Submesoscale Dynamics in the Upper Ocean: Air–Sea Interactions and Energy Transfers

Thesis by
Yue (Luna) Bai

In Partial Fulfillment of the Requirements for the
Degree of
Doctor of Philosophy

CALIFORNIA INSTITUTE OF TECHNOLOGY
Pasadena, California

2026
Defended Aug 26, 2025

Yue (Luna) Bai
ORCID: 0009-0003-6431-8413

ACKNOWLEDGMENTS

I dedicate this section to the many important people whose support, encouragement, and belief in me have sustained me through every stage of this journey and made the completion of this thesis possible.

I feel especially fortunate to have had Andy Thompson as my Ph.D. advisor. Despite what I am convinced is an already overflowing schedule held together by sheer passion, determination, and coffee, he always made time whenever I felt discouraged or uncertain about my research or life. His scientific intuition and wisdom are truly inspiring. His enthusiasm for science is infectious, and our conversations never failed to help me regain focus on my goals. I am deeply grateful for his endless support — both academically and personally — and I look forward to continuing to collaborate with and learn from him in the future.

I am also deeply grateful for the opportunity to work with Jörn Callies, who also served as chair of my thesis committee. Much of our work together began well outside my comfort zone, intentionally so as a challenge for myself, and became one of the most valuable learning experiences of my Ph.D. as well as, I suspect, a mentoring challenge for Jörn. The process required, and generously received, endless support, patience, encouragement, and figure-tweaking suggestions from him.

I sincerely thank the other members of my thesis committee for their support and time. I am particularly lucky to have had Bia Villas Bôas on my committee. Her sharp scientific insight always impressed me, and her thought-provoking questions have challenged me to think more critically. She is truly a role model. It was great joy to have Patrice Klein on my committee, whose wisdom and vast knowledge are matched only by his humbleness and warmth. I also appreciate Jane Bae's time and the thoughtful perspective she contributed to my committee, which enriched the breadth of feedback on my work.

I am truly thankful to all my previous mentors, whose guidance and encouragement made it possible for me to pursue a Ph.D. in the first place. Andrew Stewart and Yan Wang opened the door of physical oceanography for me as an undergraduate, and have been a constant source of support ever since. Marcelo Chamecki's dedication to mentorship strengthened my knowledge and gave me the confidence to start graduate school. Joe Fitzgerald's mentorship during my first two years of graduate school helped me transition smoothly into research.

I thank everyone at Caltech's Center for Teaching, Learning, and Outreach for helping me develop and improve on my teaching skills. Many thanks to the Caltech staff, especially Nora Oshima and Bronagh Glaser, for ensuring everything ran smoothly.

Friends I met during my Ph.D. have made powering through graduate school enjoyable and possible. Being part of Andy's OCTO Group (Bia, Channing, Dave, Emily, Emma, Earle, Gadi, Julian, Lily, Madeleine, Olivia, Mar, Mukund, Ruth, Sara, Sarah, Sam, Shantong,

Scott, Skylar, and Zichang) has been an amazing experience; I loved our weekly lunches, the book-swapping tradition, group retreats (and the tide pod event), and, most of all, the always welcoming and supportive environment. Sharing my time in the Callies Group (Albion, Bucky, Charly, Haakon, Jack, Joe, Henry, Scott, Shane, Shirui, Shriya, and Xihan) has been another highlight of graduate school. The tin-foil hat, the Chinese food cravings, and the "easy" hikes at group retreat are memories that I cherish. I also want to give a special mention to the best office ever, Linde 209, (Scott, Xihan, Ke, and Charly); I will miss our random chats, gossips, derivations, and lizard hunting. My cohort (Haakon, James, Ke, Maria, Ruth, and Scott) started with me in the middle of COVID-19, with our friendships that began on Zoom calls at the weirdest hours. To the puzzle crew (Xihan, Ke, Henry, Samantha, and Scott), I will leave my other 3,000-piece puzzle with you, trusting you to finish it. I enjoyed working with Heng, Shengduo, and Ziran at the Caltech Chinese Association. The pottery squad (Scott, Ruth, Julie, and Windy) helped me discover a potential career path if graduate school hadn't worked out. My first and most memorable research cruise to the Southern Ocean was made even better by Xihan, Xiang, Jason, Andrea, Treden, Kieran, Benoit, and Dawn. I would love to do another deep CTD cast with you all again. To my dear Xijuan, Yuer, Xinya, and Haoran — thank you for visiting me, chatting with me, and staying close throughout my years in graduate school. Our friendships, spanning time in the unit of decade(s), have been one of my greatest treasures.

Most importantly, I thank my parents, Yufeng Bai and Yanmei Liu, for their unwavering love, support, and belief in me. They respected my boldest choices — from the spontaneous decision to apply to U.S. colleges 10,000 km away from home to pursuing a field they had never even heard of. They have given me life, strength, and unconditional support, and have made countless sacrifices to ensure I have the best education and life possible.
And to the one and only special Adam Sydnor: thank you for always being by my side and never saying no to my ice cream requests. I couldn't have done this without you.

This work was financially supported by the National Aeronautics and Space Administration Science Mission Directorate FINESST program under Award No. 80NSSC21K1635 and by the Zeller-Resnick First Year Fellowship.

ABSTRACT

Submesoscale dynamics, with horizontal scales of $O(1–10)$ km, are ubiquitous in the surface ocean. Recent observations and simulations reveal enhanced sea surface temperature and velocity gradients at these scales, with sharpened buoyancy fronts attracting particular attention for their potential of energy transfer to link large-scale energy reservoirs to the small scales where dissipation occurs. This thesis addresses the following questions: How do the ocean and atmosphere interact at submesoscale? To what extent can balanced dynamics be applied to interpret submesoscale variability, and, given that, how well do balanced frameworks represent energy transfer at submesoscale fronts?

Air–sea interaction has been extensively studied at mesoscale, $O(100)$ km, but remains less well quantified at submesoscale. Mesoscale sea surface temperature and vorticity imprint their own spatial structure on wind stress gradients through thermal and current feedbacks (TFB and CFB). These feedbacks have typically been assessed separately, with limited attention to their collocation and potential joint impacts. Atmospheric wind stress modifications feed back on the ocean by altering surface vertical transports through Ekman dynamics. In submesoscale-resolving air–sea coupled simulations, examining TFB and CFB jointly reveals their combined influence on surface wind stress. The coupled effect produces anomalous wind stress curls an order of magnitude stronger than those at mesoscale. The resulting nonlinear Ekman velocities from wind stress curl changes reach magnitudes roughly ten times larger than at mesoscale, underscoring the potential importance of submesoscale air–sea coupling for vertical exchange in the surface ocean.

The submesoscale range covers a transition from balanced to unbalanced motion as spatial scales decrease. This transition scale is critical for understanding energy transfers and tracer transport in the upper ocean, yet remains poorly constrained. Because balanced motions evolve on time scales much longer than Earth's rotation period, the temporal scale of submesoscale motions can indicate their dynamical regime. Spatio-temporal analyses in submesoscale-resolving simulations and surface mooring observations show that flow-following Lagrangian time scale of submesoscale flow is much longer than that registered by a fixed Eulerian observer, placing the transition to unbalanced dynamics at $\sim$1 km, much shorter than suggested by Eulerian diagnostics. This implies that balanced theory remain applicable to submesoscale motions down to $O(1)$ km.

Although balanced quasi-geostrophic (QG) and semi-geostrophic (SG) theories reproduce submesoscale frontal development, the associated energy transfers under balanced conditions are less well understood. We derive and assess the full kinetic energy budget in spectral space and in physical space using coarse-graining for an isolated front in QG and SG frameworks. A geostrophic strain field by itself is sufficient to produce forward transfer of kinetic energy in QG frontogenesis. In SG, ageostrophic advection generates a dipole in

energy transfer linked to the convergent–divergent surface flow structure, but this balanced ageostrophic circulation is too weak to overcome the dominant forward transfer from the strain field. These results demonstrate that balanced dynamics can generate surface convergence and drive downscale transfers, and that ageostrophic circulation is essential to produce the asymmetry of energy fluxes at submesoscale fronts.

PUBLISHED CONTENT AND CONTRIBUTIONS

Bai, Y., A. F. Thompson, A. B. Villas Bôas, P. Klein, H. S. Torres, and D. Menemenlis, 2023: Sub-mesoscale wind–front interactions: The combined impact of thermal and current feedback. *Geophysical Research Letters*, **50 (18)**, e2023GL104807, doi:10.1029/2023GL104807.

TABLE OF CONTENTS

Chapter 1

INTRODUCTION

"In nature, nothing exists alone."

—Rachel Carson, *Silent Spring*[1]

The evolution of Earth's climate system is shaped by an ongoing dialogue between the ocean and the atmosphere. Their interactions begin across the oceanic and atmospheric boundary layers at the air–sea interface. Winds blowing across the sea surface set ocean currents in motion. Climate-critical tracers such as heat, carbon, and oxygen are exchanged back and forth with the overlying air, setting the properties of surface waters, some of which are subsequently subducted to depth and dispersed throughout the global ocean over timescales ranging from decades to millennia. Through this continual exchange, the ocean absorbs excess heat and carbon from the atmosphere, moderating both present and future climate and helping to sustain a habitable planet.

Like gradually clearing a fogged window, advances in observations and numerical simulations have gradually revealed the ocean to us—first from synoptic basin-scale circulations to increasingly fine structures (Fig. 1.1). As each newly resolved scale has come into focus, it has become clear that distinct dynamics and statistical properties operate at different scales, motivating scale-separated analyses. Our understanding of air–sea interactions has evolved in parallel, shaped first by processes dominating at synoptic-scale circulations, then refined with the recognition of $O(100)$ km mesoscale features, and now expanding into the $O(1–10)$ km submesoscale regime. However, it is critical to remember that no matter how different these scales appear, the ocean still functions as an integrated system, with exchanges and energy transfers across scales essential for linking the different scales together.

Early observations and theories portrayed the atmosphere–ocean interactions as largely one-way, from air to sea. In the mid-1800s, Matthew Fontaine Maury used ship logbooks of winds and currents to compile charts showing how winds drive ocean currents. Classical frameworks of large-scale ocean circulation likewise depicted the ocean as a passive recipient of atmospheric wind forcing. Ekman (1905) demonstrated that surface winds drag the surface ocean[2], inducing a transport of a surface water layer that, due to Earth's rotation, occurs at a 90° angle to the wind direction. This "Ekman transport," under the highly varying surface wind stress, results in convergence or divergence of surface flows. Convergence

[1] Rachel Carson, *Silent Spring* (Boston: Houghton Mifflin, 1962) (Carson, 1962)

[2] The surface wind stress is a body force acting per unit surface area of the surface ocean. It directly accelerates a very thin layer at the surface, creating strong vertical shear that are highly susceptible to instabilities and turbulence (e.g., Wagner et al., 2023).

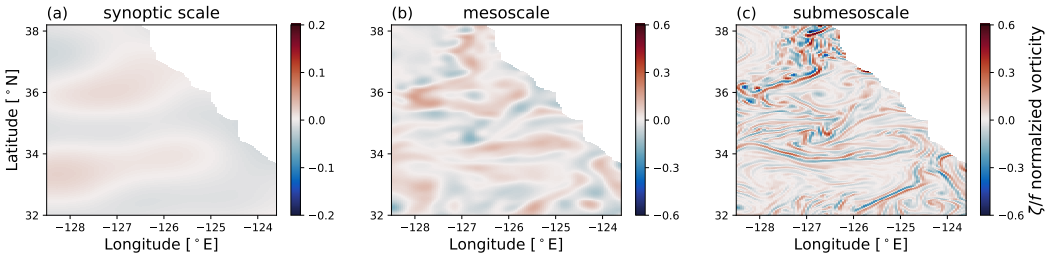

Figure 1.1: Illustration of ocean surface vorticity characteristics from a 4-km numerical simulation near the coast of California resolved at certain spatial scales: (a) synoptic scale ($>$ 200 km), (b) mesoscale ($30-200$ km), and (c) submesoscale ($<$ 30 km). Increasing resolution reveals progressively finer structures. Note that the normalized vorticity with f represents the flow Rossby number Ro.

causes surface water to pile up and downwell into the ocean interior, whereas divergence draws interior water upward into the surface layer (Stern, 1965). This vertical exchange forms the primary conduit through which surface winds communicate with the ocean interior and underpin theories of large-scale gyre circulation (Sverdrup, 1947; Stommel, 1948; Rhines and Young, 1982). At the same basin scale, a negative correlation between surface wind speed and sea surface temperature (SST) signals was identified (Liu et al., 2000; Mantua et al., 1997; Okumura et al., 2001), consistent with atmosphere forcing the ocean, as stronger winds enhance evaporation and cool the ocean surface (Small et al., 2008).

However, this atmospheric-dominant view of air–sea interactions is modified with dynamical understandings of mesoscale eddies. Mesoscale eddies are spiraling circulations in the ocean that span $O(100)$ km horizontally and persist for several months (e.g., Chelton et al., 2011b; Roemmich and Gilson, 2001; Seo et al., 2016). They were first discovered observationally back in the 1930s by Columbus Iselin on cruises across the meandering Gulf Stream (Cullen, 2005). Dynamical understandings of mesoscale eddies started in the mid-20th century from intense ship-board surveys of the Gulf Stream (Fuglister and Worthington, 1951). These mesoscale features are marked by distinct SST signatures (Hausmann and Czaja, 2012; Seo et al., 2016), and the strong currents in mesoscale eddies contain $\sim$80% of the total ocean's kinetic energy (Ferrari and Wunsch, 2009; Chelton et al., 2011b).

Diagnostics of air–sea processes confined to the mesoscale reveal relationships opposite to those predicted by earlier basin-scale theories, pointing to a regime in which the ocean actively forces the atmosphere. One key aspect is the positive correlation between SST and near-surface wind speed detected in satellite observations (Chelton et al., 2001; Liu et al., 2000), termed the "thermal feedback (TFB)." When air flows over an SST anomaly, temperature and humidity differences arise between the sea surface and the overlying air, altering the stability of the marine atmospheric boundary layer (MABL) and modulating heat exchange at the air–sea interface (Small et al., 2008; Hayes et al., 1989) [3]. Over warmer

[3] Another mechanism of wind speed change is through pressure adjustment. Heat and moisture exchanges induce pressure anomalies in the MABL, which lead to pressure-driven secondary circulations in the atmospheric

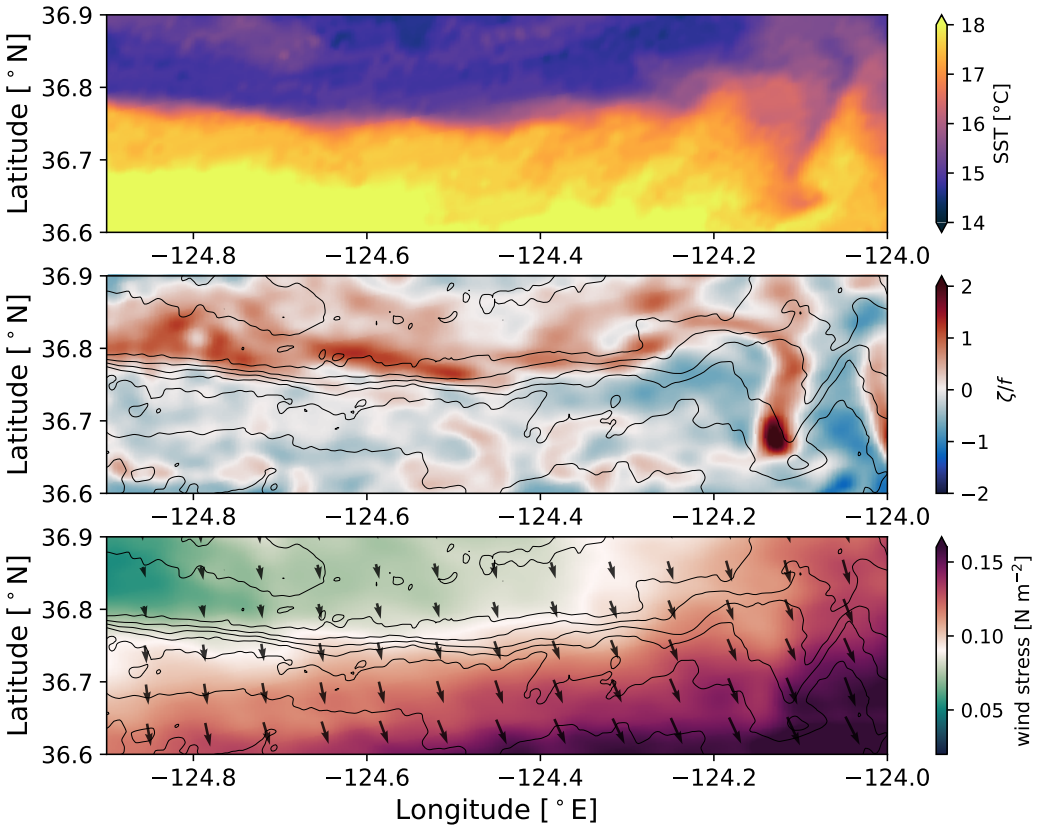

Figure 1.2: Illustration of SST and ocean surface vorticity effects on atmospheric wind stress. (a) Advanced Very High Resolution Radiometer (AVHRR) SST on 26 October 2022 (Li et al., 2001). (b) Ocean surface vorticity ζ normalized by the Coriolis parameter f on 26 October 2022, derived from the DopplerScatt platform of the Sub-Mesoscale Ocean Dynamics Experiment (S-MODE) (Farrar et al., 2025). Contours of AVHRR SST are overlaid. (c) Atmospheric surface wind stress magnitude from DopplerScatt, with AVHRR SST contours overlaid. Wind stress vectors are shown as arrows.

waters, reduced atmospheric stability enhances turbulent fluctuations of heat, moisture, and momentum, which transfer momentum from the upper boundary layer toward the surface, strengthening the near-surface wind speed (Wallace et al., 1989; Gaube et al., 2019). Over cooler waters, turbulence is more confined to the surface and winds weaken (Xie, 2004). An example is shown with surface observations from the Sub-Mesoscale Ocean Dynamics Experiment (S-MODE; Fig. 1.2c), in which surface wind stress increases as surface winds flow across an SST front from colder to warmer water. These SST-induced mesoscale wind speed changes induce wind stress gradients in the rather uniform background atmospheric wind field—expressed as wind stress curl and divergence (Fig. 1.3a,b)—which Chelton et al. (2004, 2007, 2011b); O'Neill et al. (2012); Seo et al. (2016) quantified in relation to directional SST gradients through linear coupling coefficients.

boundary layer that alters the surface wind speed (Wai and Stage, 1989; Frenger et al., 2013).

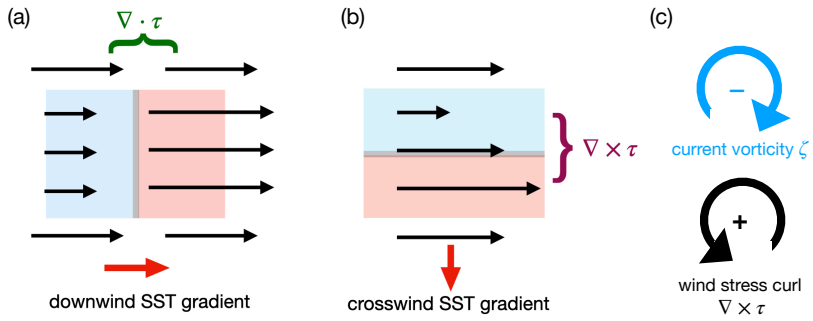

Figure 1.3: Illustration of TFB and CFB[4]. In (a, b), colored backgrounds show SST anomalies (blue: cold; red: warm). Dark arrows indicate surface wind stress, with arrow length representing its magnitude. (a) Over a downwind SST gradient (aligned with the wind), TFB generates an anomalous wind stress divergence ($\nabla \cdot \boldsymbol{\tau}$). (b) Over a crosswind SST gradient (perpendicular to the wind), TFB generates an anomalous wind stress curl ($\nabla \times \boldsymbol{\tau}$). (c) Over a negative surface ocean vorticity, CFB produces a positive wind stress curl anomaly due to the relative motion between currents and winds.

The strong mesoscale ocean currents also play a significant role in driving atmospheric changes, a process referred to as "current feedback" (CFB). The stress that surface winds exert on the ocean depends on the relative velocity between near-surface winds $\mathbf{U_a}$ and surface ocean currents $\mathbf{U_o}$, which can be expressed using the bulk formula:

$$\boldsymbol{\tau} = \rho_a C_d (\mathbf{U_a} - \mathbf{U_o}) |\mathbf{U_a} - \mathbf{U_o}|, \tag{1.1}$$

in which $\boldsymbol{\tau}$ is the wind stress, ρ_a is that density of air, C_D is the drag coefficients (e.g., Seo et al., 2016; Renault et al., 2016b). Rotating mesoscale eddies are typically of much smaller scales than variations in the atmospheric wind field, and therefore the air–sea velocity difference varies across the eddy: wind stress is enhanced on the side where ocean currents and winds oppose each other, and reduced on the side where they move in the same direction (Renault et al., 2016b, 2017). This produces a negative correlation between ocean surface current vorticity and the surface wind stress curl, defined respectively as:

$$\zeta = \frac{\partial v}{\partial x} - \frac{\partial u}{\partial y}, \quad \text{and} \quad \nabla \times \boldsymbol{\tau} = \frac{\partial \tau_y}{\partial x} - \frac{\partial \tau_x}{\partial y}. \tag{1.2}$$

The difference in relative velocities across the mesoscale eddy leads to a positive–negative dipole of differential wind work that averages to be negative (Fig. 1.3c). On average, through CFB, atmospheric wind work input is reduced, damping oceanic kinetic energy on mesoscale eddies by $\sim 30\%$ (Renault et al., 2016b; Xu and Scott, 2008).

[3]In addition to the negative correlation between surface current vorticity ζ and wind stress curl, a negative correlation also exists between ocean surface divergence and wind stress divergence due to current-induced adjustments to the surface wind stress. This divergence correlation is absent at the oceanic mesoscale (Renault et al., 2018), where the flow is largely non-divergent, but emerges at the submesoscale where surface divergence becomes significant (Bai et al., 2023; Chen et al., 2022). Given the relevance of wind stress curl to Ekman velocities in the ocean, this thesis analyzes CFB effects on wind stress divergence (Chapter 2) but focuses primarily on interpreting wind stress curl.

These interactions are termed "feedbacks" because once oceanic features imprint on atmospheric wind fields, the resulting atmospheric changes, in turn, alter upper-ocean dynamics. One manifestation of this is through changes in near-surface vertical velocities. Following Stern (1965), Ekman-driven vertical velocities consist of two components. Small-scale wind stress gradients from CFB and TFB produce "linear Ekman velocities" (McGillicuddy et al., 2007; Gaube et al., 2015), while the feedbacks' direct modification of wind stress interacts with surface ocean vorticity gradients and generates "nonlinear Ekman velocities" (McGillicuddy et al., 2007; Stern, 1965; Wenegrat and Thomas, 2017). A global satellite-based survey by Gaube et al. (2015) found that CFB-driven linear and total nonlinear Ekman velocities dominate the overall Ekman vertical velocity field, except in energetic western boundary currents where TFB linear contributions are comparably strong. The magnitudes of these feedback-driven vertical velocities are typically $O(10)$ cm day^{-1}.

The role of the ocean in driving atmospheric variability, which in turn induces vertical motions in the surface ocean, has been well established at the mesoscale, but remains less understood at the submesoscale (O(1–10) km, evolving over hours to days). Submesoscale motions include smaller rotating eddies as well as elongated fronts (Fig. 1.1c) with sharp temperature and velocity gradients[5] (Capet et al., 2008b; McWilliams, 2016; Srinivasan et al., 2023). Because they are small and short-lived, submesoscale motions are especially challenging to observe using conventional ship surveys, satellite measurements, or global climate models (Bodner et al., 2020), not to mention a collocated and concurrent measurement of atmospheric wind field. As a result, our current understanding of submesoscale air–sea interactions mostly comes from numerical simulations. Strobach et al. (2022) reported wind stress curl anomalies of up to 10^{-5} Nm^{-3} associated with $\sim$10 km SST fronts in the Gulf Stream, nearly an order of magnitude larger than values typically inferred from mesoscale studies (e.g., Chelton et al., 2004). Chen et al. (2022) further showed that the negative correlation between ocean surface vorticity and wind stress curl persists at these smaller scales.

However, strong SST gradients and ocean velocity gradients rarely exist in isolation in the upper ocean. Chelton et al. (2004) noted that their collocation may indicate simultaneous interactions of TFB and CFB with the atmosphere, potentially altering the relationships identified in previous mesoscale studies that examined each feedback separately (e.g., Chelton et al., 2007; O'Neill et al., 2012; Renault et al., 2016b). Chapter 2 of this thesis, published as Bai et al. (2023), addresses this by identifying and quantifying potential interactions between air–sea feedbacks. A two-dimensional (2-D) conditional mean analysis is proposed to assess the joint influence of TFB and CFB on wind stress gradients such as curl and divergence. Unlike conventional one-dimensional (1-D) binning with either TFB or CFB, the 2-D approach measures wind stress gradients as a function of both simultaneously. Using a coupled

[5] Submesoscale fronts are associated with strong surface buoyancy gradients influenced by both temperature and salinity; in this thesis work we focus on temperature effects.

ocean–atmosphere simulation at 2–4 km resolution (Torres et al., 2022b), Chapter 2 identifies regimes in which CFB and TFB either reinforce or oppose one another's influence on wind stress derivatives. When acting in concert, their combined effects produce wind stress derivative anomalies up to 10 times stronger than in mesoscale-resolving studies. It is also proposed that surface wind stress variations from air–sea interactions can be approximated from surface ocean velocity and SST gradients through:

$$\nabla \times \boldsymbol{\tau} \approx \alpha\zeta + \beta\nabla_c SST, \tag{1.3}$$

in which the coefficients α and β are solved based on the 2-D analyses. This 2-D reproduce the magnitude and structure in atmospheric wind field from surface ocean velocity and SST,

$$\nabla \times \boldsymbol{\tau} \approx \alpha\zeta + \beta\nabla_c SST, \tag{1.4}$$

more accurately than if using coefficients from the previous 1-D analyses. Accounting for this joint effect provides a more accurate and complete description of air–sea interactions.

If air–sea feedbacks jointly modify atmospheric winds, they potentially can change how these small-scale atmospheric variability feeds back onto the near-surface ocean. In Chapter 3, we investigate this impact on Ekman vertical velocities in the same ocean–atmosphere coupled simulation, with a focus on submesoscale air–sea interactions. By explicitly separating the flow fields into mesoscale (30–200 km) and submesoscale (< 30 km) components, we find that the largest atmospheric wind stress anomalies originate exclusively from imprints of oceanic submesoscale surface features. Linear and nonlinear Ekman velocities at each scales are compared for the first time. In addition, we propose a decomposition of nonlinear Ekman velocities into CFB and TFB contributions to more accurately quantify their impacts on the upper ocean. At mesoscale, the results largely agree with Gaube et al. (2015); Seo et al. (2016), showing that air–sea processes govern most of the variability in upper-ocean Ekman velocities at mesoscale. At sub-30 km scales, however, nonlinear Ekman velocities grow be to an order of magnitude larger than CFB- and TFB-induced linear Ekman velocities, and are driven primarily by intensified surface ocean vorticity gradients. This reveals a new regime of vertical velocities in which small-scale surface ocean processes exert a dominant influence on air–sea interaction, underscoring the critical role of submesoscale dynamics in upper ocean air–sea processes.

Besides their role in air–sea interactions, submesoscale motions possess distinctive features that set them apart from mesoscale flows and make them central to upper-ocean dynamics. A frequently emphasized feature of the submesoscale range is their high Rossby number,

$$\mathrm{Ro} = \frac{U}{fL}, \tag{1.5}$$

where U is a velocity scale, L a length scale, and f the Coriolis frequency. Ro, which measures the relative importance of inertial (advective) forcing to the Coriolis force from Earth's

rotation, transitions from Ro $\ll 1$ at mesoscale to Ro $\gtrsim 1$ at submesoscale (Fig. 1.1). This transition, emphasized in previous studies (Thomas et al., 2008; McWilliams, 2016), marks a shift in flow behaviors and dynamics. At the mesoscale, rotational effects dominate over advection, and the flow is largely in geostrophic balance, with motions spanning large horizontal scales but limited vertical extent. Submesoscale flows, however, at least partially escape rotational constraints (Thomas et al., 2008; McWilliams, 2016; Taylor and Thompson, 2023), exhibiting enhanced surface divergence and vertical velocities (Balwada et al., 2018; Barkan et al., 2019). These vertical velocity are thought to have a substantial impact on heat, nutrient, and carbon transfers at the surface ocean (Mahadevan, 2016; Rosso et al., 2016; Balwada et al., 2018; Su et al., 2018; Siegelman et al., 2020).

In contrast with expectations from classical energy-transfer theory, submesoscale motions imprint a strong energetic signature in the upper ocean. In the mesoscale regime, where flows are largely geostrophically balanced, the classical dual-cascade paradigm of geostrophic turbulence describes how large-scale available potential energy (APE) is converted into kinetic energy via mesoscale baroclinic instability (e.g., Rhines, 1977; Salmon, 1978). Nonlinear triad interactions then redistribute that energy: kinetic energy undergoes an inverse transfer to energize larger scales, while enstrophy cascades forward to smaller scales (Kraichnan, 1967; Charney, 1971; Scott and Wang, 2005; Tulloch et al., 2011; Arbic et al., 2013). This framework implies that little energy should remain at submesoscale, or at any scales smaller than the mesoscale deformation radius (Charney, 1971). Yet, both observations and high-resolution simulations reveal vigorous submesoscale activities in the surface ocean (Capet et al., 2008b; Lapeyre and Klein, 2006; Callies et al., 2015; Shcherbina et al., 2013; Naveira Garabato et al., 2022).

This persistence of energy at the submesoscale is ultimately enabled by the constraints imposed by the mere presence of ocean surface boundary (Capet et al., 2008b; Held et al., 1995; Lapeyre and Klein, 2006), which partially violate the assumptions of classical geostrophic turbulence and two-dimensional turbulence theories that apply well to mesoscale turbulence (e.g., Charney, 1971; Salmon, 1978; Kraichnan, 1967). Two main mechanisms are proposed to be responsible for the enhanced energy in the submesoscale range: mixed layer instabilities (MLI) and strain-driven frontogenesis (Callies et al., 2016; Barkan et al., 2019; Fox-Kemper et al., 2008). MLI operates similarly to mesoscale baroclinic instability but at smaller spatial scales of O(1–10) km confined largely in the surface mixed layer. It is enabled by the potential-vorticity jump at the base of the mixed layer, which permits submesoscale baroclinic instability catalyzed by lateral buoyancy gradients in the mixed layer. During the process of MLI, dense water is displaced downward and lighter water is lifted upward, essentially increasing the stratification in the surface mixed layer (Boccaletti et al., 2007). Besides the lateral buoyancy variations, the potential energy reservoir available for conversion by MLI depends strongly on the depth of the mixed layer, which deepens in winter. Both numerical simulations (Sasaki et al., 2014) and observations (Callies et al., 2015;

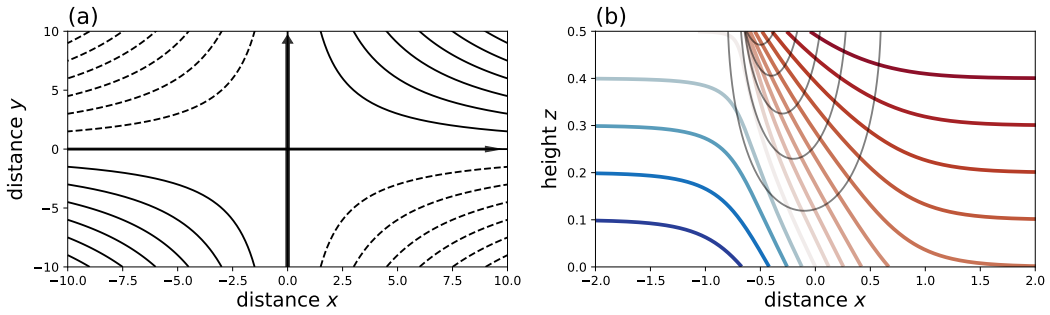

Figure 1.4: Illustration of strain-driven frontogenesis under semi-geostrophic (SG) constraints. (a) The background strain field $-\alpha x$ and αy with constrain strain rate α. (b) The buoyancy field $N^2 z + b_0$ (color) and the along-front flow v_0 (gray) in SG dynamics.

Naveira Garabato et al., 2022) show more energetic submesoscale motions in winter, with activity suppressed in summer.

Strain-driven frontogenesis provides another pathway for the surface energization of submesoscale fronts (Fig. 1.4). The essential dynamics, long recognized in the atmospheric literature, originate in quasi-geostrophic (QG) theory (Stone, 1966). A mesoscale strain field sharpens lateral buoyancy gradients at the surface and in the interior, which in turn induces an ageostrophic secondary circulation described by the omega equation (Hoskins et al., 1978), linking lateral buoyancy gradient with flows in the cross-frontal plane. This circulation produces downwelling on the dense side of the front and upwelling on the lighter side. In the ocean interior, these vertical motions act to counter further intensification of the buoyancy gradient; at the surface, however, vertical transport must vanish, allowing lateral buoyancy gradients to grow unchecked. While QG theory successfully captures the onset of frontogenesis and ageostrophic circulation, a major limitation is that the front sharpens slowly and never collapse — a result inconsistent with observations. To address this, Hoskins and Bretherton (1972) developed a semi-geostrophic (SG) theory of frontogenesis, which allows ageostrophic flows to advect momentum. This key distinction turns out to be critical: ageostrophic flow pushes the center of the front to a surface convergent zone, enhancing asymmetry and leading to finite-time frontal collapse. Both QG and SG frontogenesis are considered "balanced," as they describe flow regimes governed by potential vorticity conservation and an associated inversion principle, where the full flow field can be reconstructed from the distribution of potential vorticity (Hoskins et al., 1985). They generally assume a small Ro. Despite their simplified dynamics, these theories provide powerful representations of key aspects of oceanic frontal flows.

The unique dynamics and intermediate spatial scale of submesoscale flows place them at the forefront of efforts to understand how energy transfers from the larger mesoscale to the submesoscale, and ultimately to the smaller scales where viscous dissipation occurs. Oceanic energy sinks occur at both large and small spatial scales. Large-scale sinks arise from body

forces like top and bottom drag (Ferrari and Wunsch, 2009), while small-scale sinks rely on eddy and viscous dissipation (Gregg, 1989; Wunsch and Ferrari, 2004). Interaction with the ocean bottom can generate boundary-layer turbulence and produce bottom-enhanced dissipation (e.g., Ferrari and Wunsch, 2009). Lee waves are generated behind the wake of bottom topography, whose breaking exerts a net drag on the mean flow (e.g., Nikurashin et al., 2013). Although part of the mesoscale energy could be dissipated by large-scale surface drag, interactions with topography and waves, and air–sea interactions via CFB, the inverse energy cascade characteristic of mesoscale turbulence does not provide an efficient pathway for the remainder to be dissipated through molecular diffusivity (Bodner et al., 2020). To maintain steady state, energy must cascade from mesoscale reservoirs forward progressively to smaller spatial scales where dissipation becomes dominant. At the submesoscale, numerical simulations and observations agree that most energy released by MLI also cascades inversely to larger scales, filling the gap between the mixed-layer deformation radius and the mesoscale through triad interactions (Sasaki et al., 2014; Boccaletti et al., 2007; Rocha et al., 2016; Lawrence and Callies, 2022). However, part of the MLI-released energy does undergo a forward transfer to reach microscale dissipation (Capet et al., 2008b), and the persistence of this dissipation even at resolution sufficient to resolve $O(1\ \mathrm{km})$ motions indicates that it is a pathway for energy removal (Capet et al., 2008c).

In submesoscale fronts, recent studies using coarse-graining approaches (Leonard, 1975; Eyink, 1995; Aluie et al., 2018) applied to realistic primitive-equation simulations have revealed significant forward energy transfer, suggesting that submesoscale fronts act as a viable conduit for downscale energy fluxes. Specifically, Srinivasan et al. (2023) identified a tight link between surface convergence and frontal energy transfer. A characteristic dipole pattern emerges on either side of submesoscale fronts: the convergent side induces forward transfer to smaller scales, while the divergent side shows inverse transfer to larger scales. When integrated over a pool of submesoscale fronts, the forward transfer associated with convergence outweighs the inverse transfer associated with divergence, resulting in a net forward transfer. The driver of strong surface convergence and hence the forward frontal transfer is attributed to unbalanced processes, such as turbulent thermal wind (TTW) (Barkan et al., 2019; Srinivasan et al., 2023). TTW describes a balanced between rotation, pressure gradient, and vertical momentum mixing, in which vertical mixing disrupts geostrophic balance and accelerates the front's cross-frontal ageostrophic circulation [6]. This mechanism could intensify the convergent side of a front, enhancing the forward transfer there (Dauhajre et al., 2025).

Given the dynamical transition that occurs somewhere within the submesoscale range, an important question regarding energy transfer at fronts arises: to what extent can balanced theories like QG and SG capture the forward–inverse dipole of energy transfer observed in

[6] Vertical momentum mixing is generally parameterized with eddy viscosity (e.g., Fox-Kemper et al., 2008; Bodner et al., 2020), and prevailingly regarded as frontogenic (Garrett and Loder, 1981).

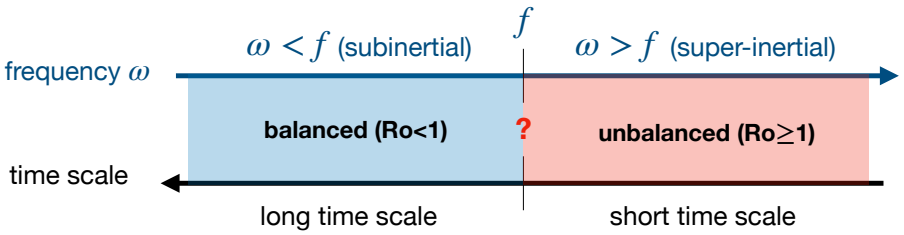

Figure 1.5: Schematic of the submesoscale transition from balanced to unbalanced dynamics, marked by changes in flow time scale and frequency ω. The transition time scale and its corresponding length scale occur somewhere within the broad submesoscale range but remain poorly quantified.

realistic simulations? Although QG and SG frameworks are well established for reproducing key flow features in strain-driven frontogenesis (Stone, 1966; Hoskins and Bretherton, 1972; Hoskins, 1975), the associated energy transfer under balanced conditions has received relatively little attention and remains poorly constrained. Realistic numerical studies tend to exclusively associate forward transfer to unbalanced dynamics such as momentum mixing and mixed-layer turbulence Barkan et al. (2019); Srinivasan et al. (2023). However, in principle, when a strain field sharpens a lateral surface buoyancy gradient, the surface convergence transfers kinetic energy to smaller scales. This suggests that, at least in theory, balanced dynamics should be able to reproduce a forward energy transfer at fronts without invoking unbalanced dynamics.

The potential of using balanced dynamics to describe submesoscale motions is sometimes overlooked. The ongoing debate over "balance" and the uncertainty of when and where it ceases to hold reflects a fundamental gap in the theoretical understanding of submesoscale dynamics (McWilliams, 2016). Within the broad range of submesoscale motions (O(1–10)km), the dynamics transition from being largely describable by balanced theories such as QG and SG to being predominantly unbalanced, as the Rossby number (Ro) increases from $\ll 1$ to $O(1)$ (Thomas et al., 2008). Ro can be alternatively expressed as a ratio of the time scale of Earth's rotation f^{-1} and an advective time scale of $\tau = L/U$: $\mathrm{Ro} = (\tau f)^{-1}$. The shift to unbalanced motion therefore occurs when τ becomes comparable to f^{-1}, the inertial timescale (Fig. 1.5). Motions with frequencies greater than f (super-inertial) thus have $\mathrm{Ro} \sim 1$ and shorter timescales, indicative of unbalanced dynamics. In a submesoscale-permitting numerical simulation, Torres et al. (2018) decomposed oceanic kinetic energy into spatial and temporal scales using Eulerian Fourier filters and found that submesoscale turbulence reaches super-inertial frequencies at scales as large as ~50 km. This suggests that QG and SG theories might have reached their limit at scales of $O(10)$ km or smaller, failing to capture the dynamics at smaller scales. This is followed by studies that have appealed to unbalanced dynamics (e.g., Barkan et al., 2019; Srinivasan et al., 2023) to describe submesoscale frontogensis and energy transfer. Yet, other studies using a Lagrangian flow-following perspective have successfully applied balanced theory to interpret dynamics down to $O(1)$ km (e.g., Thomas et al., 2008; Callies et al., 2016).

Reconciling the dichotomy between balanced and unbalanced dynamics in describing submesoscale motions hinges on a key question: at what temporal or spatial scale within the broad submesoscale range does the transition to unbalance occur? In Chapter 4, we argue that Doppler shifting could bias Eulerian estimates of submesoscale timescales, artificially making balanced motions appear unbalanced. Following Callies et al. (2020), intrinsically balanced and sub-inertial submesoscale features may be embedded within, and advected by, a faster mesoscale flow. From a fixed Eulerian perspective, this advection can make the submesoscale flow appear to change rapidly, even if the feature itself evolves at balanced time scale, resulting in a spuriously high observed frequency being assigned to the flow. A simple kinematic example of a submesoscale eddy advected by a uniform mean flow illustrates this point: to an Eulerian observer, the apparent flow frequency reflects the background mean flow, whereas from a flow-following Lagrangian perspective, the mean flow is a zero-frequency component and only the slowly-varying intrinsic eddy frequency is captured. We test this effect in realistic numerical simulations by comparing Eulerian and Lagrangian frequency–wavenumber analyses, the latter computed from particle advections. Mooring observations in the North Atlantic (Yu et al., 2019; Callies et al., 2020) show a similar pattern: over the same flow field, Eulerian spectra is elevated in sub-inertial frequency range compared with Lagrangian spectra, but reduced in the lowest frequencies, suggesting that slow motions are misclassified as faster in the Eulerian frame. The Lagrangian numerical analysis further suggest that Ro reaches unity at spatial scales as small as sub-10 km, implying that QG and SG balanced remain valid to at least $O(1)$ km, with unbalanced dynamics becoming more important at smaller scales.

Continuing from Chapter 4, Chapter 5 uses simplified QG and SG models to investigate the direction and distribution of energy transfer in strain-driven frontogenesis. To isolate the underlying dynamics, we consider an idealized front without background turbulence. The key distinction between the QG and SG frameworks is whether the ageostrophic circulation participates in momentum transfer: SG includes ageostrophic advection, enhancing frontal asymmetry. We assess kinetic energy evolution first in spectral space for an integrated view, then in physical space using a coarse-graining approach to examine the existence of the dipole structure and compare directly with numerical studies (e.g., Srinivasan et al., 2023). In QG frontogenesis, the narrowing jet along the sharpening front is powered by buoyancy production, but downscale transfer due to the background strain field plays an important role in the forward energy transfer. In SG, the ageostrophic secondary circulation induces a forward transfer on the dense side of the front and an inverse transfer on the light side. This forward–inverse dipole introduces asymmetries in the energy transfer, similar to those observed in realistic simulations, although its magnitude is insufficient to offset the background forward transfer driven by the strain field. Our results show that balanced dynamics can generate surface convergence and drive downscale transfer, with ageostrophic circulation essential for reproducing the observed asymmetry of energy fluxes in the adiabatic and

frictionless frontogenesis considered here. This also points to the importance of mixed-layer turbulence in inducing the ageostrophic circulation and the associated scale transfers.

Finally, in Chapter 6, we summarize the main findings and outline future directions. The numerical results about joint air–sea interactions and impacts on the surface ocean in Chapters 2 and 3 highlight the potential for air–sea processes to influence tracer fluxes and transports of latent and sensible heat, carbon, and other climate-relevant properties. The newly available observations from the Surface Water and Ocean Topography (SWOT) satellite mission offer potentially powerful tools to quantify submesoscale air–sea impacts and constrain global budgets of these climate-critical tracers. Extending these analyses to include additional surface processes, such as wave–eddy interactions (e.g., Villas Bôas et al., 2020; Conn et al., 2024), could reveal exciting dynamics. Building on Chapter 5, applying the scale-resolved analysis of the full kinetic energy budget to realistic simulations, where fronts are embedded in a turbulent eddy field, would provide a natural next step towards a deeper understanding of forward energy transfer at submesoscale fronts.

Chapter 2

SUB-MESOSCALE WIND–FRONT INTERACTIONS: THE COMBINED IMPACT OF THERMAL AND CURRENT FEEDBACK

This chapter is reproduced from the published article:

Bai, Y., Thompson, A. F., Villas Bôas, A. B., Klein, P., Torres, H. S., and Menemenlis, D. (2023). Sub-mesoscale wind–front interactions: The combined impact of thermal and current feedback. *Geophysical Research Letters*, **50 (18)**, e2023GL104807, doi:10.1029/2023GL104807.

As a self-contained work, some notation may differ from conventions used elsewhere in this thesis.

2.1 Abstract

Surface ocean temperature and velocity anomalies at meso- and sub-meso-scales induce wind stress anomalies. These wind-front interactions, referred to as thermal (TFB) and current (CFB) feedbacks, respectively, have been studied in isolation at mesoscale, yet they have rarely been considered in tandem. Here, we assess the combined influence of TFB and CFB and their relative impact on surface wind stress derivatives. Analyses are based on output from two regions of the Southern Ocean in a coupled simulation with local ocean resolution of 2 km. Considering both TFB and CFB shows regimes of interference, which remain mostly linear down to the simulation resolution. The jointly-generated wind stress curl anomalies approach 10^{-5} Nm^{-3}, ∼20 times stronger than at mesoscale. The synergy of both feedbacks improves the ability to reconstruct wind stress curl magnitude and structure from both surface vorticity and SST gradients by 12-37% on average, compared with using either feedback alone.

2.2 Introduction

The exchange of heat and momentum between the ocean and the atmosphere is a critical component of global climate evolution. Processes that govern air–sea coupling and the transfer of climate-relevant tracers occur across a broad range of scales (Small et al., 2019; Strobach et al., 2022; Renault et al., 2018; Chang et al., 2020; Seo et al., 2023), with transitions in air–sea behavior occurring at a few key spatial scales. At the basin scale, the atmosphere supplies the momentum that powers the ocean currents (Rai et al., 2021) and determines the oceanic distribution of latent and sensible heat fluxes Small et al. (2008, 2019). At oceanic mesoscale, or spatial scales of $O(100)$ km and Rossby number $\mathrm{Ro} = \zeta/f \ll 1$ (where ζ is the vertical component of relative vorticity), these relationships reverse and ocean surface variability triggers atmospheric responses (Chelton and Xie, 2010; Re-

nault et al., 2016b; Small et al., 2019; Frenger et al., 2013; Seo et al., 2023). This change in behavior occurs due to two dynamical processes that become relevant at the scale of ocean mesoscale eddies: the thermal and current feedbacks (TFB and CFB), which are related to surface ocean temperature and velocity gradients, respectively. wind–front interactions have been studied almost exclusively using satellite products (e.g., Chelton et al., 2004) and mesoscale-resolving numerical simulations (e.g., Renault et al., 2016b; Takatama and Schneider, 2017). In the ocean, however, another dynamical transition occurs at $O(10)$ km, scales smaller than the mesoscale, where the Rossby number approaches $O(1)$. Hereafter, we refer to $O(10)$ km and Ro $\gtrsim 1$ motions as "sub-mesoscale." While the impact of these sub-mesoscale features on air–sea interactions remains largely unconstrained, they are characterized by strong anomalies in vorticity and density gradients (Siegelman et al., 2020; Taylor and Thompson, 2023; Balwada et al., 2018) that may contribute to the TFB and CFB.

The thermal component of wind–front interactions assesses the "bottom-up" (Renault et al., 2018) thermodynamic influence of sea surface temperature (SST) gradients on the atmospheric wind fields (Chelton et al., 2004).Forerunner studies, such as Chelton et al. (2001, 2004); O'Neill et al. (2012), empirically established positive linear relationships between wind stress divergence and wind stress curl with downwind and crosswind SST gradients (defined in Sec. 2.4.1), respectively. Mechanisms that support the TFB coupling were reviewed in detail by Small et al. (2008). Gradients in SST modify the overlying atmospheric boundary layer stability and the surface drag coefficient. This in turn generates mesoscale variability in wind speed and stress through either pressure adjustment or downward momentum transfer (Frenger et al., 2013; Desbiolles et al., 2023). Chelton et al. (2007, 2011b); O'Neill et al. (2012) quantified these correlations through linear coupling coefficients and found seasonal fluctuations in the coupling intensity (Chelton and Xie, 2010). The TFB influences the distribution of latent and sensible heat fluxes (Foussard et al., 2019), and induces wind stress curl anomalies that can enhance Ekman pumping, especially in the Southern Ocean (Gaube et al., 2015).

Current feedback (CFB), the mechanical driver of wind–front interactions, arises from the difference between surface vector winds and surface ocean currents. Since mesoscale eddies are typically of smaller spatial scale than atmospheric variations, the air–sea velocity difference is non-uniform across the eddy. This feature causes eddies with positive vorticity to generate a negative wind stress curl anomaly (Renault et al., 2016b), and eddies with negative vorticity to generate a positive wind stress curl anomaly (Rai et al., 2021). Bye (1985) and Rooth and Xie (1992) showed analytically that the negative correlation between vorticity and wind stress curl is linearly dependent on the magnitude of the local surface wind speed. Renault et al. (2017) used mesoscale satellite observations to confirm that the current-stress coupling coefficient depends on local surface wind speed. CFB is a sink of the oceanic mesoscale geostrophic kinetic energy to the atmosphere (Renault et al., 2016b; Xu

and Scott, 2008). This "eddy killing" effect acts through the wind stress curl-induced Ekman pumping (Gaube et al., 2015) that counteracts the eddy vorticity and therefore weakens the eddies (Renault et al., 2018). At mesoscales, where flows are to leading order geostrophic and divergence-free, the connection between surface current divergence and wind stress divergence is often neglected (Renault et al., 2018).

Recent high-resolution numerical simulations have enabled a first exploration of sub-mesoscale wind–front feedbacks, which are shown to be significantly enhanced compared with those at mesoscales. Strobach et al. (2022) focused on SST fronts of ∼10 km in the Gulf Stream using a sub-mesoscale-resolving coupled simulation. These SST gradients are up to 20 times stronger than those observed in pioneering mesoscale studies (e.g., Chelton et al., 2004), and they generate large wind stress curl anomalies up to 10^{-5} N m^{-3}. In an idealized simulation, Chen et al. (2022) confirmed the enhancement of CFB due to sub-mesoscale surface vorticity anomalies that exceed the local Coriolis parameter f. At the sub-mesoscale, flow begins to escape the constraint of Earth's rotation, and surface divergence starts to assume a comparable magnitude as the surface vorticity (Thomas et al., 2008; McWilliams, 2016; Callies et al., 2020). At those small spatial scales, a negative linear correlation between surface divergence and wind stress divergence was recently identified (Chen et al., 2022), in addition to the well-established correlation between ocean vorticity and wind stress curl. The impact of sub-mesoscale wind–front interactions on globally-integrated heat and momentum budgets are yet to be quantified.

Most previous studies, including recent studies that resolve sub-mesoscales, quantify wind stress derivatives as a function of either TFB or CFB, but rarely consider the two processes in tandem. Chelton et al. (2004) pointed out that strong density fronts are often collocated with strong currents and speculated that wind stress curl modifications from TFB could potentially be contaminated with CFB (Small et al., 2008). Renault et al. (2019) and Takatama and Schneider (2017) developed controlled mesoscale simulations to separate the two feedback mechanisms by only having one active at a given time, and identified their individual contribution to wind stress curl. However, in a coupled simulation or using observations, it is not possible to separate the impact on the wind stress derivatives from individual feedback mechanisms, and predictions from these "1D" studies, hereby referred to as 1D current or 1D thermal analysis, may be inaccurate due to the combination or cancellation of correlated TFB and CFB. In this study, we use output from a high-resolution coupled climate model to show that there is a large region of parameter space where an accurate prediction of wind stress derivatives requires accounting for both feedbacks. We adopt a "2D" perspective that incorporates both TFB and CFB and assesses their joint influence and relative importance simultaneously.

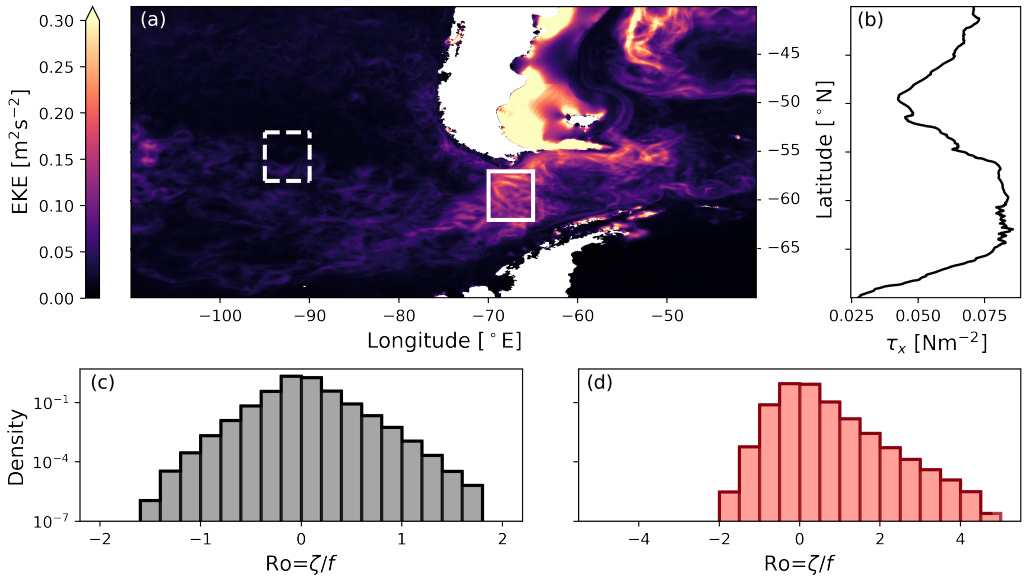

Figure 2.1: Southern Ocean study domains. (a) Mean surface eddy kinetic energy (EKE [m^2 s^{-2}]) for austral winter months in 2012, taken from the COAS simulation (see section 2.3), for the eastern Pacific sector of the Southern Ocean. The white boxes show two subdomains that are the focus of this study. The western (dashed) and eastern (solid) boxes correspond to quiescent (58-53°S, 95-90°E) and energetic (62-57°S, 70-65°E) regions, respectively. (b) Zonally-integrated zonal wind stress [N m^{-2}] for the region shown in panel (a). (c) Histogram of Rossby number in the quiescent region; (d) histogram of Rossby number in the energetic region.

2.3 Methods and Study Region

In this study, we use outputs from the state-of-the-art global Coupled Ocean-Atmosphere Simulation (COAS), commonly referred to as C1440-LLC2160. The oceanic component of COAS has a horizontal grid spacing of 1/24°, approximately 2 km around Antarctica. The atmospheric models has a nominal horizontal grid spacing of 6.9 km. The simulation was initialized on January 20th, 2012 and results shown below are based on output from June 1st to August 31st, 2012 (JJA). This configuration is identical to that used in Torres et al. (2022b), from which the readers can find more general information on the model and experiment setup. The unprecedented spatial and temporal resolutions of this global coupled simulation make it a unique and necessary tool to study meso-to-sub-mesoscale wind–front interactions, a regime that remains under-explored.

The present study focuses on two subdomains that are within or close to the Drake Passage region of the Southern Ocean (Fig. 2.1), where the impact of variable ocean surface properties is disproportionally large Nicholson et al. (2022). We select this region because it is aligned with the westerly wind stress maximum (Fig. 2.1b), and the Southern Ocean is a key site of air–sea exchange and ventilation Marshall and Speer (2012); Dove et al. (2021); Gruber et al. (2019), both of which may be impacted by vertical velocities linked to small-scale wind–front interactions Gaube et al. (2015); Renault et al. (2023). Furthermore, the two 5°×5° subdomains compare a quiescent, low eddy kinetic energy (EKE) regime, and

a turbulent frontal region with higher background energy levels, the latter of which have been shown to localize and enhance ventilation Dove et al. (2022, 2023). The surface Ro distribution (Fig. 2.1c,d) for quiescent and energetic regions both favor cyclonic eddies and respectively have skewness values of 0.4 and 0.9, suggesting more sub-mesoscale fronts Buckingham et al. (2016); Barkan et al. (2019) and frontal slumping Hoskins and Bretherton (1972) in the energetic region; Ro also has a larger magnitude in the energetic region.

In the following sections, we describe the 2D approach and the synergy of thermal and current feedbacks with output from the energetic region. These results do not depend on the dynamical processes that generate the SST gradients and vorticity anomalies; therefore we primarily focus on the statistical impact on wind-stress gradients in this simulation. Results from the quiescent subdomain provided in the Supplementary Information (SI) offer preliminary insight into regional variations. A more thorough regional and temporal analysis of wind–front interactions is beyond the scope of is left for future work.

2.4 Results

In this section, we consider the relative importance of both TFB and CFB by constructing a series of two-dimensional, binned-averaged, conditional mean plots that evaluate the joint dependence of wind stress curl and divergence on surface ocean vorticity/divergence and temperature gradients. We also quantify the relative contribution of each feedback on wind stress properties via linear coefficients, and investigate the temporal variability of these coefficients as well as the mechanisms that give rise to the variability.

2.4.1 Combined impact of thermal and current feedbacks

The dependence of wind stress curl and divergence on surface ocean properties illustrates scenarios and regimes where, if considered using the 2D approach, CFB and TFB combine constructively and destructively. These regimes are evaluated by bin-averaging the hourly wind stress curl or divergence as a function of two properties, one chosen from each category: ocean vorticity and divergence, or crosswind and downwind SST gradient. Crosswind SST gradients are defined by $\boldsymbol{\nabla} SST \times \boldsymbol{\tau}$ in which the winds are aligned with the front. For downwind SST gradients, $\boldsymbol{\nabla} SST \cdot \boldsymbol{\tau}$, the winds are perpendicular to the frontal direction. Ocean vorticity and divergence are normalized by the absolute value of f, while SST gradients are scaled by a typical sub-mesoscale frontal length scale, $\sim$ 10 km. Note that the normalizations are different from previous mesoscale studies in order to highlight sub-mesoscale features. A series of conditional mean plots (Fig. 2.2) are constructed with non-uniform bin sizes as data points are sparse for extreme values; non-dimensionalized vorticity ($\zeta/|f|$) and divergence ($\delta/|f|$) have bin sizes ranging from 0.1 near 0 to 0.5 at ± 4; crosswind and downwind SST gradient bin sizes range from 0.1°C/10 km near 0 to 0.4°C/10 km at ± 8 (see further details in SI). These results are qualitatively similar when using uniform bin sizes. We calculate the mean and other statistical moments, using hourly output, to which we

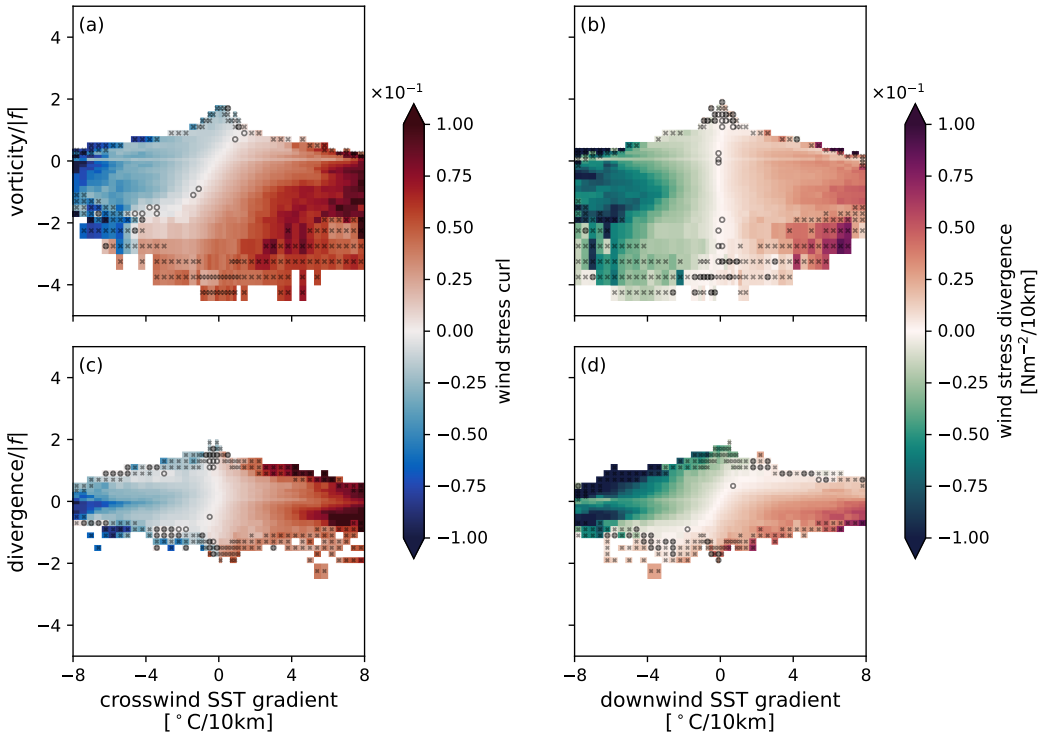

Figure 2.2: Conditional mean plots, conditioned on surface ocean vorticity or divergence and cross-wind or downwind SST gradients, colored by mean values of either wind stress curl or wind stress divergence. Cross marks indicate bins with less than 50 points after removing data outside of mean ± 1 standard deviation. Circles indicate bins with standard error that is larger than the mean value. (a) The joint influence of vorticity and crosswind SST gradient on wind stress curl. (b) TFB from downwind SST gradient on wind stress divergence. (c) TFB from crosswind SST gradient on wind stress curl. (d) The joint influence of ocean divergence and downwind SST gradient on wind stress divergence. The slope of the zero-line (white in all panels) indicates the level of interaction and competition between surface vorticity/divergence and crosswind/downwind SST gradients in generating small-scale features in the wind stress fields. Evidence of sub-mesoscale dynamics is indicated by regions where the magnitude of $\mathrm{Ro} = \zeta/f$ is greater than 1 and is positively skewed (Fig. 2.1).

apply a one-day running mean to each field to remove high-frequency variability, likely related to atmospheric fluctuations. All values of wind stress curl/divergence over the full austral winter period (JJA, 2012) are collected for a given combination of vorticity/divergence and crosswind/downwind SST gradient, from which the standard deviation is calculated. Data that exceed ± 1 standard deviation, in each bin, are removed before computing the mean wind stress product to further minimize outliers introduced by synoptic events. The mean percentage of data removed in each panel ranges from 24.8% to 30.9%. The calculations of slopes and coefficients in Sec. 2.4.2 are not sensitive to this standard deviation cutoff.

There are eight possible combinations from two sets of surface variables as axes (ocean vorticity/divergence and cross/down-wind SST gradients): four for wind stress curl and four for wind stress divergence. Four are highlighted in Fig. 2.2 that are representative of different CFB and TFB regimes. When only one property is relevant to the wind stress derivative, the

conditional mean plot provides similar information as the independent 1D approach; when both properties are correlated with the wind stress field, the 2D perspective show patterns of interaction.

Between the two chosen axes of the conditional mean plot, if only one of the properties is contributing actively to wind-ocean feedbacks, then the wind stress derivative varies along a single axis, for example, Fig. 2.2b and c. This essentially reduces to an independent 1D analysis. In Fig. 2.2b, the mean wind stress divergence is close to zero when the downwind SST gradient is weak, for all values of surface vorticity. Positive downwind SST gradients lead to a positive wind stress divergence. This indicates that SST gradients and the TFB dominate small-scale structures in wind stress divergence, while surface vorticity plays a negligible role in setting small-scale variability. By averaging across surface vorticity values, the traditional 1D binned analysis of the TFB slope compares well with previous studies (e.g., Chelton and Xie, 2010). TFB also occurs where crosswind SST gradient is positively correlated with wind stress curl, while ocean divergence, as the other axis, has a limited impact (Fig. 2.2c).

The conditional mean analysis also illustrates regimes where components from both CFB and TFB contribute to wind stress gradients. In Fig. 2.2a, both vorticity and crosswind SST gradients shape small-scale variations in wind stress curl. For a given surface vorticity, wind stress curl increases linearly with crosswind SST gradient. However, meso- and smaller-scale features in wind stress curl are at the same time imprinted from surface ocean vorticity, which causes wind stress curl to decrease with increasing vorticity, at fixed crosswind SST gradients. Together, this causes the zero-line (white) in wind stress curl to be tilted between the independent TFB- and CFB-dominant regimes. CFB constructively reinforces TFB feedback in the second (negative SST gradient and positive vorticity) and fourth (positive SST gradient and negative vorticity) quadrants, while destructively attenuating or even reversing the sign of the wind stress curl anomaly in the first (positive SST gradient and vorticity) and third (negative SST gradient and vorticity) quadrants. The combined influence is also present in Fig. 2.2d, in which wind stress divergence is a function of both ocean surface divergence and downwind SST gradients. The constructive interaction between both feedbacks suggests that anomalously large wind stress curl or divergence occurs at large magnitudes of SST gradients and surface vorticity or divergence values, when they have the opposite signs. In Fig. 2.2a, the jointly-generated wind stress curl approaches anomalously positive values that are over 0.1 N m^{-2}/10 km, about 20 times stronger than in previous mesoscale studies (e.g., Chelton et al., 2004). This enhancement at small scales is also consistent with Strobach et al. (2022)'s 1D study on sub-mesoscale thermal feedback. These results also confirm, in a realistic numerical setting, that strong sub-mesoscale surface ocean divergence imprints on wind stress divergence, first shown in an idealized simulation by Chen et al. (2022). Although high-resolution 1D studies show enhanced feedback impact, they neglect variations from the other feedback and tend to underestimate wind stress curl or divergence, which is

illustrated in Sec. 2.4.2.

2.4.2 Vorticity and crosswind SST gradient: contribution and variability

Based on the interaction between both feedbacks, in this section we test the hypothesis that most variance in wind stress fields can be explained by a combination of ocean surface vorticity/divergence and cross/downwind SST gradients when the wind stress field is not dominated by synoptic events. The following analysis is focused on the dependence of wind stress curl on surface vorticity and crosswind SST gradients, but the same approach applies to wind stress divergence (see SI). We propose a dependent, bivariate, as opposed to univariate, and linear model to reconstruct wind stress curl:

$$\boldsymbol{\nabla} \times \boldsymbol{\tau} = \alpha \, \boldsymbol{\zeta}/|f| + \beta \, \boldsymbol{\nabla}_c \mathrm{SST}. \tag{2.1}$$

$\boldsymbol{\nabla}_c$SST stands for crosswind SST gradients. The coefficients α and β are solved for simultaneously by inverting the matrix whose columns correspond to vorticity scaled by $|f|$ and crosswind SST gradients scaled by 10 km within the subdomain and over the desired time scales. The coefficients vary with the chosen normalization, but the relative contributions of the two terms on the right-hand side of (2.1) are not dependent on normalizations. These coefficients are directly related to the 2D wind stress curl distributions, such that the ratio of α and β corresponds to the zero-line slope (not shown) in Fig. 2.2a. To assess the importance of the combined TFB and CFB, we compare the 2D dependent reconstruction to wind reconstructions due to CFB and TFB alone, as well as the linear sum of these two cases, for example, with α and β coefficients determined independently.

Among the various reconstruction approaches, the ones that incorporate both feedbacks (2D and 1D current + thermal) provide a more accurate representation of the variance of wind stress curl (Fig. 2.3). We solve for the 2D and 1D coefficients at hourly intervals in the energetic subdomain (Fig. 2.1) and reconstruct the wind stress curl linearly based on (2.1). Notably, the reconstructed wind stress curl has similar magnitudes using the bivariate 2D and 1D current + thermal approaches (Fig. 2.3b,e and g,j). By comparison, univariate reconstruction performances based on only one feedback, 1D current (Fig. 2.3c,h) or 1D thermal (Fig. 2.3d,i), fluctuate in time, suggesting that CFB or TFB dominance can vary even in a localized region. To statistically quantify their agreement with the simulated wind stress curl, the hourly Pearson correlation coefficient squared r^2 is shown in Fig. 2.3k for each method. Agreement between the two time series of r^2 reconstructed by both feedback suggests similar spatial structures, while 1D current or 1D thermal feedback preferably recovers vorticity or filamentary structures, respectively. The r^2 values indicate that skill in reconstructing wind stress curl improves when both feedbacks are involved. Specifically, the 1D current and 1D thermal reconstructions have 40% and 10% larger domain-averarged root-mean-square error (RMSE) for the three-month period (Fig. 2.3l) as compared to the 2D reconstruction. The 1D independent sum slightly under-performs the 2D approach, with 3% more RMSE.

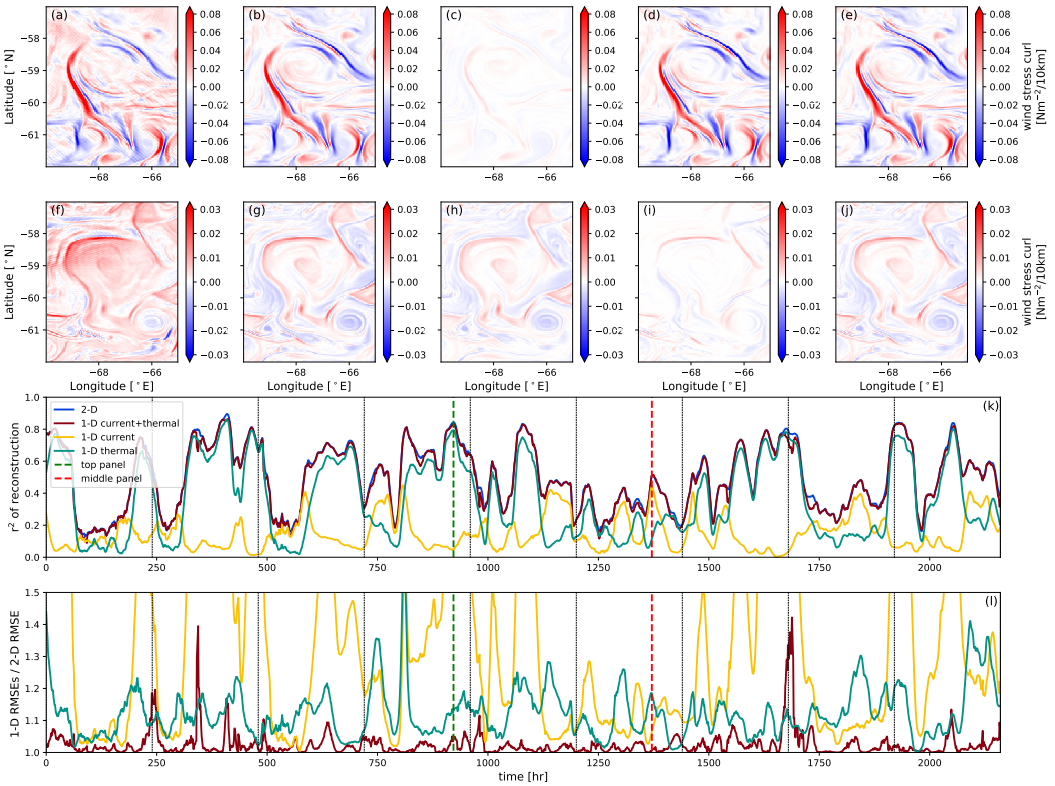

Figure 2.3: Illustration of reconstruction performances with simulated wind stress curl snapshots and hourly reconstruction variability. The top two panels (a-j), from left to right, show: (a,f) wind stress curl from the numerical simulation, (b,g) wind stress curl estimated by 2D dependent coefficients for both current and thermal feedback, (c,h) reconstruction based on 1D current feedback, (d,i) reconstruction based on 1D thermal feedback, (e,j) reconstruction fromthe linear sum of the 1D current and thermal feedbacks. Pearson linear correlation coefficients squared (r^2) of each reconstruction and simulated wind stress curl are calculated per hour in (k). The root-mean square error of all 1D reconstruction methods as well as the 2D error are averaged through the subdomain in (l). The 1D current RMSE ratio curve is cropped, but reaches a maximum value of 2.98. The dashed lines indicate an instance of thermal and current feedback dominance that correspond to panels (a-e) and (f-j), respectively. Black dashed lines are 10 days separations.

However, caution should be taken in interpreting the reconstruction performance, as (2.1) is limited when large-scale wind stress curl anomalies pass through the subdomain, potentially linked to synoptic events, as discussed in Sec. 2.5.

The 2D coefficients improve the wind stress curl reconstruction, but their values are time dependent (Fig. 2.4). α and β are calculated as in (2.1) with one-, five-, and fifteen-day time windows within the energetic domain. For each case, the coefficients are calculated by updating the center of the window by one day; the values are plotted at the window midpoint in Fig. 2.4b,c. Wintertime daily-calculated α has a mean of -0.017$\pm$0.006 N m^{-2}/10 km and β has 0.013$\pm$0.007 N m^{-2}/°C. The standard deviation for both coefficients reduces to $\sim$ 0.003 at 15-day time scale. The ratio, $\beta/|\alpha|$, across all three windowing time scales is about 0.8 10km/°C, which is consistent with the zero-line slope in Fig. 2.2a.

We explored a wide range of physical properties at the air–sea interface that could contribute to variations in α and β, and find that the most relevant are wind speed and air–sea temperature difference, respectively (Fig. 2.4a,d). Within one-, five-, and fifteen-day time windows, wind speed at 10 m and each coefficient are scattered and the correlation between them is quantified with Pearson linear coefficients r_{W_α} and r_{W_β} (Fig. 2.4e,f). Absolute values of r_{W_α} and r_{W_β} both increase with windowing length. Having $r_{W_\alpha} > 0.8$ indicates that α has a tight linear correlation with wind speed; this is weaker between β and wind speed with r_{W_β} ranging from 0.6-0.8. Indeed, when 1D binned means and standard deviations of α and β are calculated as a function of wind speed (with bin sizes 1 m s^{-1}), β has a spread that is twice as large compared with α, on average (Fig. 2.4e, f). We explore β's relationship with air–sea temperature difference, noting that the quadratic drag coefficient of wind stress calculation, C_d, depends on this temperature difference. The correlation, r_{T_β} (Fig. 2.4g), ranges from $0.4 - 0.7$, with the largest r_{T_β} occurring for one-day time windows. The implications of the correlation dependence on time scale are discussed in Sec. 2.5.

2.5 Discussion

This study emphasizes the importance of a 2D perspective on wind–front interactions at sub-mesoscales that accounts for the joint impact of TFB and CFB. This is illustrated by the distribution of wind stress curl as a function of surface vorticity and crosswind SST gradient (Fig. 2.2). Incorporation of both feedbacks improves the skill of hourly wind stress field estimations compared with the traditional (univariate 1D) approaches (Fig. 2.3). These relationships are summarized in terms of coefficients α and β that describe the dependence on vorticity and crosswind SST gradients, respectively. The coefficient fluctuations are strongly correlated with variations in domain-averaged wind speed and air–sea temperature difference, respectively. In this section, we discuss implications of these small-scale wind–front interactions (Fig. 2.2) as well as some limitations of the linear reconstruction.

Both TFB and CFB are required to accurately reconstruct wind stress field variability (Fig. 2.3). Wind stress curl reconstructions are similar using either a 2D dependent sum or 1D current + thermal sum. Yet, using TFB or CFB alone leads to a larger domain-averaged RMSE, up to 60% and 190%, respectively. This occurs because the dominant feedback can vary with time (Fig. 2.3k, l).

However, when both feedbacks are taken into account, the 2D dependent sum does not significantly outperform the 1D independent current + thermal sum. Thus, the interaction between TFB and CFB, at least in this simulation, remains largely linear from larger scales, $O(100)$ km, to the resolved scales in this study, $O(10)$ km, including regions where Ro $\gtrsim 1$. The accuracy of the 1D independent sum may deteriorate as the model resolution increases, allowing for stronger and non-linear fronts. The temporal scale at which the upper ocean vorticity and SST fields evolve may also alter the relative importance of CFB and TFB.

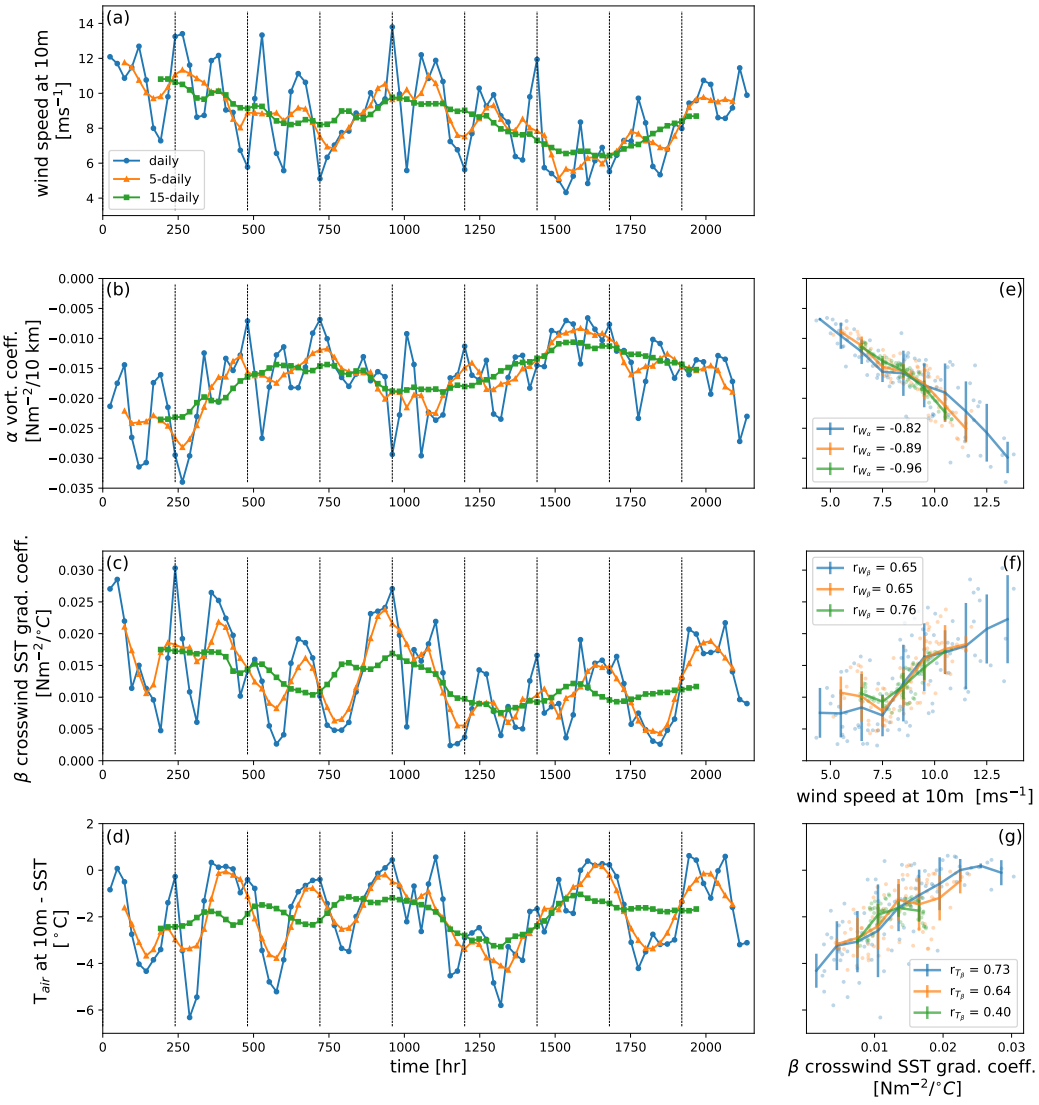

Figure 2.4: Variability of coefficients α and β and their correlation with wind speed and air–sea temperature difference. Temporal evolution of (a) wind speed, (b) α, (c) β, and (d) air–sea temperature difference (air temperature at 10 m $-$ SST). The temporal variability is spatially averaged over the domain and over the same time period in which α and β are obtained. (e) Correlation between wind speed and α with Pearson correlation coefficient r_{W_α}. (f) Correlation between wind speed and β with Pearson correlation coefficient r_{W_β}. (g) Correlation between air–sea temperature difference and β with Pearson correlation coefficient r_{T_β}.

While consideration of both vorticity and SST gradients improves wind stress curl reconstruction over 1D individual estimates, there remain periods when the inferred wind stress curl field differs significantly from the simulated output, at least as measured by r^2 (Fig. 2.3). Further analysis of the reconstructed snapshots during these periods as well as the RMSE suggests a more nuanced relationship. During high r^2 events ($r^2 > 0.6$), the simulated wind stress curl is dominated by vorticity and strain structures that reflect those at the ocean surface. In most of the anomalously low r^2 events ($r^2 < 0.2$), the simulation is characterized by a large-scale, anomalous wind stress curl event that obscures the underlying fine-scale structures, which is potentially related to synoptic storms. The proposed 2D coefficients support reconstruction of the slowly-varying wind stress curl structures, therefore leading to occasional low r^2 values when synoptic transient events dominate the wind field. Indeed, removing the domain averaged wind stress derivatives at those instances recovers some finescale structures and raises r^2 by 25-50%.

Spatially, the CFB and TFB coefficients are not uniform throughout the domain, but are instead tied to coherent structures, such as filamentary strain or eddy vorticity centers (Balwada et al., 2021) as diagnosed by the Okubo-Weiss parameter (SI). This information may be useful for future observational campaigns, similar to the Sub-Mesoscale Ocean Dynamics Experiment (S-MODE) (Farrar et al., 2020), in terms of experiment design and real-time adaptive sampling. The different characteristic time scales of variability for α and β as well as the differing correlations between the two coefficients and various physical properties suggest that CFB and TFB vary in response to different physical processes. Vorticity coefficients α are linearly correlated with wind stress magnitude ($r_{W_\alpha} > 0.8$) for all three time windows (Fig. 2.4e), indicating an almost instantaneous domain-wide adjustment to wind stress curl through changes in relative velocities. The TFB coefficient β correlates with both air–sea temperature difference and wind speed, yet the spread is almost twice as large in the wind speed correlation. Since the highest r_{T_β} occurs at daily time scales (Fig. 2.4g), we infer that air–sea temperature differences and the daily atmospheric heating/cooling cycle explain most of the variance for high frequency variations of β. This is consistent with (Desbiolles et al., 2023), which identified a correlation at a daily time scale between 1D thermal feedback and air–sea temperature gradients in reanalysis data. In contrast, r_{W_β} remains moderate for all time scales. The larger spread may be explained by a longer time for wind speed adjustment through downward momentum mixing in the atmospheric boundary layer as compared to air–sea temperature thermal adjustments. A more detailed mechanistic analysis of β and its relationship to wind speed and air–sea temperature gradient is needed. The relative contributions from each feedback are expected to vary both temporally and spatially throughout the global ocean; mapping this behavior is left for future studies.

This study has focused on simulated, wintertime properties from Drake Passage, Southern Ocean. This region hosts especially vigorous mesoscale and sub-mesoscale flow fields (Luecke et al., 2017), enabling strong wind–front interactions and the potential for enhanced

ventilation. Compared to the rest of the global ocean, properties unique to the Southern Ocean include stronger surface winds (Flexas et al., 2019) (Fig. 2.1b), sharper surface density gradients, deeper mixed layers (Dong et al., 2008), and weaker stratification, which, combined with the connectedness to the world ocean basins (Talley, 2013), make the Southern Ocean a critical location where the impact of wind–front interactions and modifications to air–sea fluxes may have a global impact (Nicholson et al., 2022). The stronger sub-mesoscale modification to wind stress curl in this studycould potentially enhance vertical velocities in the upper ocean through Ekman dynamics (Gaube et al., 2015; Seo et al., 2016). The impact of wind–front interactions on the transport of tracers, ventilation, and upper ocean stratification in the Southern Ocean are key directions for future study (Morrison et al., 2022; Swart et al., 2023).

2.6 Conclusions

Estimation of both the structure and magnitude of wind stress curl or divergence improves when the combined impact of surface ocean velocity and SST gradients, or the synergy of current and thermal feedbacks, are considered. Conditional mean plots of wind stress curl and wind stress divergence illustrate that in the Southern Ocean, the two feedbacks constructively and destructively interact and jointly control anomalies in the wind fields at sub-mesoscale. Temporal variability of each feedback is tied to physical properties such as wind speed or air–sea temperature difference, or both, implying the underlying mechanical and thermodynamical mechanisms of wind–front interactions. The results presented in this study are based on an energetic domain that is relevant to other strong western boundary currents. Yet, the mechanism of wind–front interactions is generic and applies to other ocean regions with varied intensity. A more comprehensive quantification of the two feedbacks is indispensable to constrain the calculation of air–sea fluxes and ocean surface properties. This study highlights the need for future observational endeavors with collocated measurements of surface currents, SST, and surface wind stress.

Acknowledgments

YB acknowledges support from the National Aeronautics and Space Administration Science Mission Directorate FINESST program under Award No. 80NSSC21K1635. AFT and ABVB were supported by NASA grant 80NSSC19K1004; ABVB received additional support from the NSF award OCE-2241822.

Open Research

The coupled ocean-atmosphere simulation used in this study is accessible through: (a) any NASA Ames Supercomputer at ∼ dmenemen/c1440_llc2160; (b) xmitgcm: `https://xmitgcm.readthedocs.io`; (c) NASA Ames data portal: `https://data.nas.nasa.gov/ecco/`. Example calculation and plotting codes are here: `https://doi.org/10.5281/zenodo.8231130`.

2.7 Supplementary materials

2.7.1 Introduction

This supplementary information provides additional panels and error analysis of 2D conditional mean plots in the energetic subdomain in Drake Passage. Specifically, this document presents a wind stress divergence reconstruction as a function of surface divergence and downwind SST gradient. Also, a discussion of the spatial distribution of the feedback coefficients, which is not included in the main text, is provided here. Finally, we compare our analysis in the energetic region of the Southern Ocean to a more quiescent subdomain (Fig. 2.1).

2.7.2 Additional 2D conditional mean plots and associated error analysis

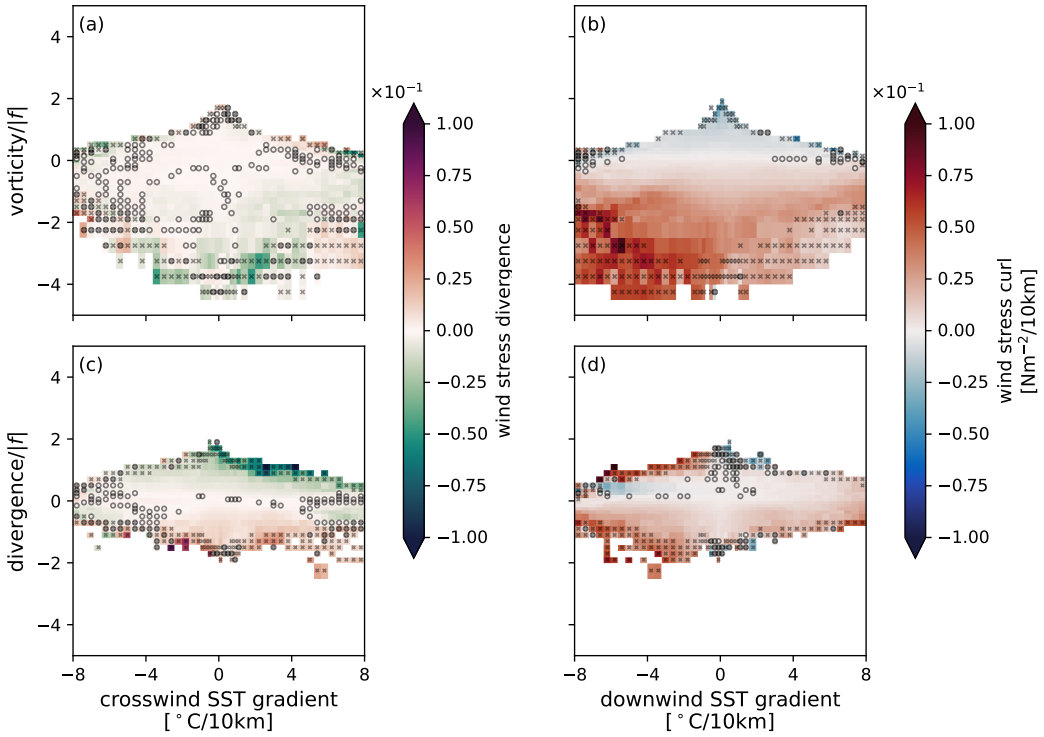

Figure 2.5: Conditional mean plots, for the combinations not presented in Fig. 2.2. Conditions for cross marks and circles are the same as in Fig. 2.2. (a) Wind stress divergence is not correlated with ocean surface vorticity or crosswind SST gradient. (b) CFB from surface vorticity on wind stress curl. (c) CFB from surface divergence on wind stress divergence. (d) Wind stress curl is not correlated with surface divergence or downwind SST gradient.

Considering wind stress curl and divergence as a function of both surface ocean vorticity/divergence and crosswind/downwind SST gradients, there are eight combinations of 2D conditional mean plots to visualize the impact of TFB and CFB on spatial wind stress patterns (four for each of wind stress curl and divergence). Four of the combinations are shown in the panels of Fig. 2.2, which highlight both the interaction between TFB and CFB

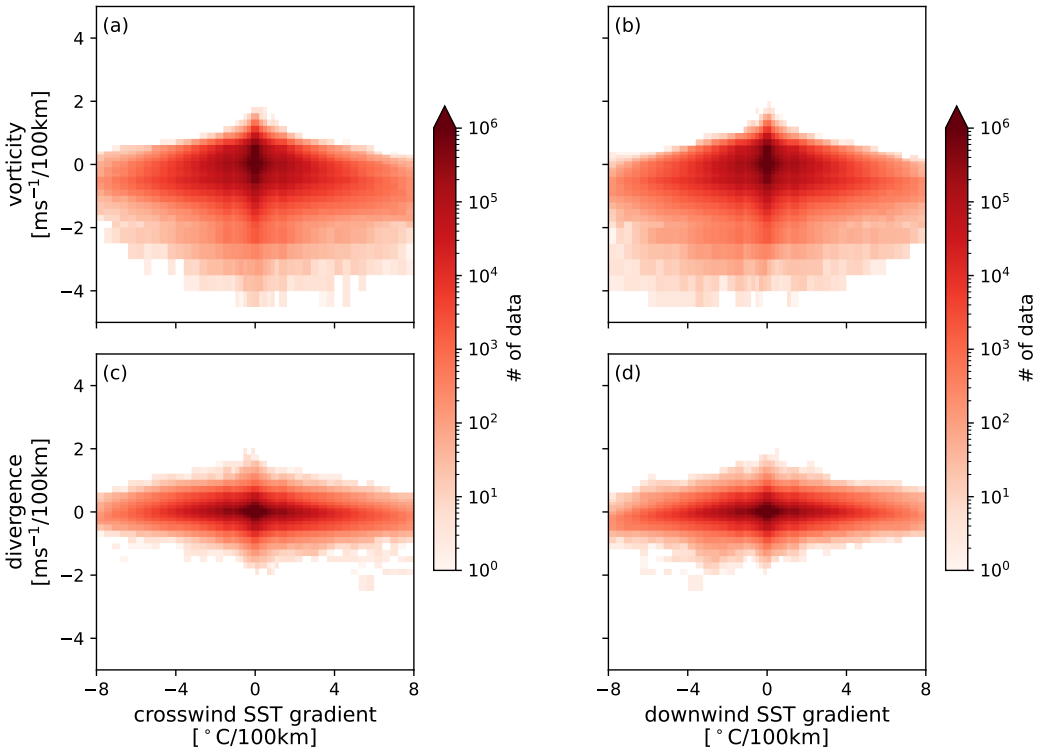

Figure 2.6: Total number of data within in ±1 standard deviation of the total mean. All panels are conditioned by the same physical properties as panels in Fig. 2.2.

(Fig. 2.2a,d) and 1D scenarios where TFB is significant (Fig. 2.2b,c). The other four combinations are computed and averaged in the same way as in the main text (Fig. 2.2), and showcase scenarios where only components of the CFB are relevant to the selected wind stress product (Fig. 2.5b,c), or when both chosen components of TFB and CFB are irrelevant (Fig. 2.5a,d). To illustrate, in Fig. 2.5b, the mean wind stress curl is close to zero when the ocean surface vorticity is weak, regardless of the magnitude of the downwind SST gradient. Positive wind stress curl values occur in the negative vorticity regime. This shows that ocean surface currents and the CFB set small-scale variability in wind stress curl, while downwind SST gradient plays a negligible role here. This CFB control is also visible in Fig. 2.5c, in which ocean surface divergence is negatively correlated with wind stress divergence. In Fig. 2.5a,d, in which both ocean vorticity/divergence and cross/downwind SST gradients considered are uncorrelated with the wind stress fields, the distributions are random and no clear zero-lines are visible. Similar to the properties discussed in the main text, there is an asymmetric distribution of vorticity with regions having a Rossby number larger than 1 preferentially associated with cyclonic vorticity.

Assessment of errors associated with the 2D conditional mean calculation is needed to provide confidence in our documented patterns of TFB and CFB, especially for large values of

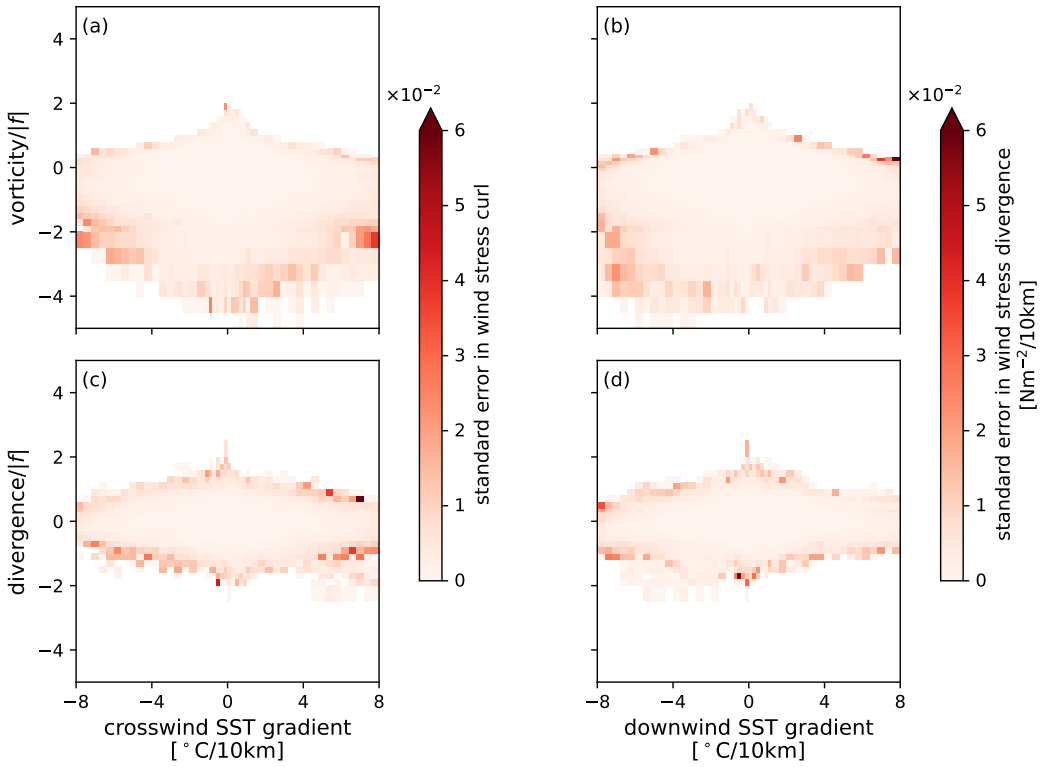

Figure 2.7: Standard error $\frac{\sigma}{\sqrt{n}}$ (σ is the standard deviation and n is the total number of points) in each bin. All panels are conditioned by the same physical properties as panels in Fig. 2.2, and therefore represent their standard error.

vorticity/divergence and strong SST gradients. The total number of data points within ± 1 standard deviation of the bin-averaged value (for each bin, Fig. 2.2) is shown in Fig. 2.6. As expected, most data points occur at small vorticity/divergence and SST gradient values. However, there are substantial data points at the extremes to provide meaningful statistics. Standard errors (Fig. 2.7) $\frac{\sigma}{\sqrt{n}}$, in which σ is the standard deviation and n is the total number of points in each bin, are computed to highlight the credibility of the mean values in each bin. Bins with higher standard error values are generally located at the edge of the distributions and might indicate a regions of parameter space with insufficient data or a greater impact of outliers.

As mentioned in the main text, we use non-uniform bin sizes in both surface ocean vorticity/divergence and SST gradients when computing the 2D conditional mean plots. Bin sizes generally increase away from zero so that the number of points in each bin at extreme values of vorticity and SST gradients are not too low. The vorticity bin sizes are:

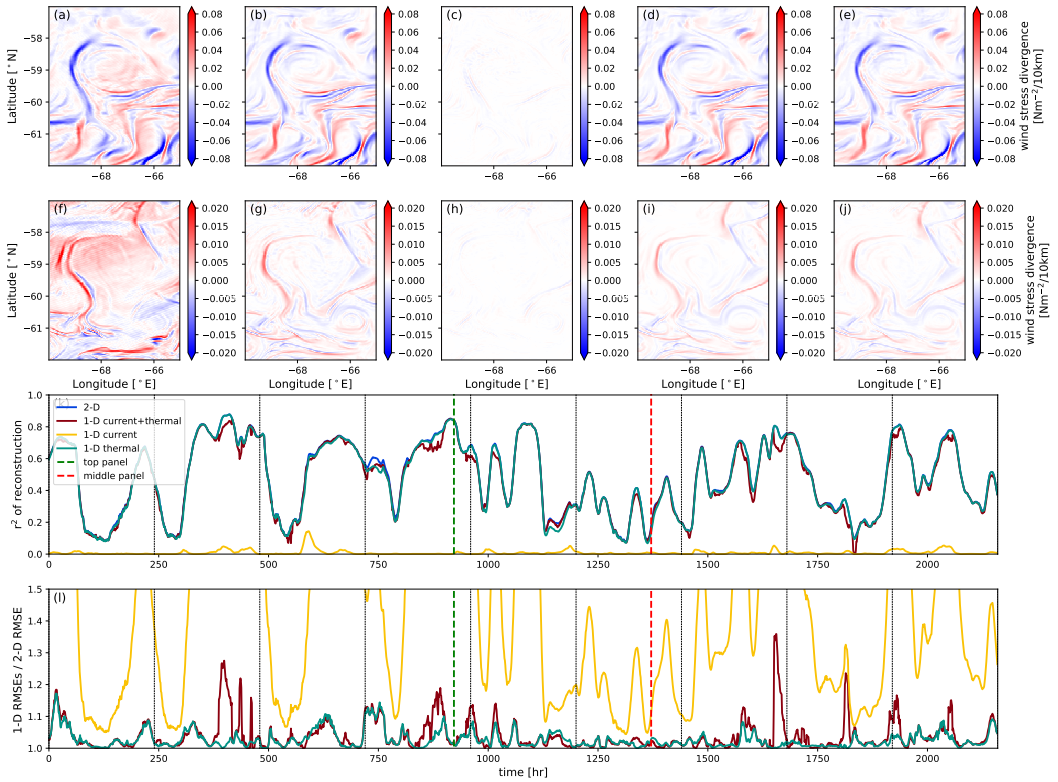

Figure 2.8: Wind stress divergence reconstruction. The top two panels are taken at the same snapshot as the wind stress curl reconstruction (Fig. 2.3 Within the top two panels, from left to right are simulated wind stress curl (a,f), 2D reconstruction (b,g), 1D current reconstruction (c,h), 1D thermal (d,i), and 1D current + thermal (e,j).

$$\Delta bin = \begin{cases} 0.1 & |\zeta/f|, |\delta/f| \leq 0.4 \\ 0.2 & 0.4 < |\zeta/f|, |\delta/f| \leq 2 \\ 0.5 & 2 < |\zeta/f|, |\delta/f| \leq 5. \end{cases}$$

The crosswind or downwind SST gradient bin sizes (with unit $^\circ C/10\text{km}$) are:

$$\Delta bin = \begin{cases} 0.2 & \text{SST gradients} \times 10^4 \leq 2 \\ 0.4 & 2 < \text{SST gradients} \times 10^4 \leq 8. \end{cases}$$

Using uniform bin sizes of 0.2 and 0.2 ($^\circ C/10\text{km}$) for both vorticity/divergence and SST gradients does not significantly change the results of the 2D conditional mean plots.

Following the same method of producing a linear 2D reconstruction of wind stress curl in Sec. 2.4, here we present the reconstruction method for wind stress divergence:

$$\boldsymbol{\nabla} \cdot \boldsymbol{\tau} = \alpha\, \delta/|f| + \beta\, \boldsymbol{\nabla}_d \text{SST}, \tag{2.2}$$

where α is still the coefficient of CFB, but for ocean surface divergence $\boldsymbol{\delta}/|f|$, and β for downwind SST gradient $\boldsymbol{\nabla}_d$SST. 2D and 1D calculations remain the same as in Sec. 2.4.

In the energetic subdomain, most variance in wind stress divergence (Fig. 2.8) is explained by variability in the downwind SST gradient, even though surface ocean divergence has a similar order of magnitude as vorticity at the nominal resolution of this simulation, ∼10 km. Unlike for wind stress curl, for most times, 1D thermal reconstruction captures the structure of wind stress divergence as well as the dependent 2D or independent 1D current + thermal reconstruction. This suggests that wind stress divergence is dominated by mesoscale oceanic variability; at these scales, the ocean surface divergence is negligible. Overall, the 1D thermal reconstruction has 0-17% larger RMSE than the 2D reconstruction; averaged over time, the error associated with the 1D thermal reconstruction is 3% larger. It is anticipated that, with increased spatial resolution and improved representation of submesoscale features, the impact of ocean surface divergence on the wind stress field will enhance. At these smaller scales, consideration of ocean surface divergence when reconstructing submesoscale wind stress divergence will be necessary.

2.7.3 Spatial distribution of α and β with surface dynamical features and implications for future observational missions

As mentioned briefly in the main text, the coefficients of TFB and CFB contributions to the wind stress curl (β and α, respectively) are spatially variable, and the patterns of variability relate to coherent structures in the upper ocean. Both α and β, as well as the magnitude of the Pearson correlation coefficient r^2 determined from the 2D reconstructed and simulated wind stress curl (Fig. 2.3), are sensitive to dynamical regimes identified from an Okubo-Weiss (OW) filter. Positive values of OW indicate a strain-dominated region and negative values of OW indicate a vorticity-dominated region. Following a similar approach based on the strain-vorticity joint probability distribution functions in Balwada et al. (2021), the coefficient calculations (Sec. 2.4) are repeated using a subset of wind and ocean data in the energetic subdomain, screening with the OW parameter. One- and fifteen-day time-averaging windows are used as in the main text. When conditioning on $OW/f^2 < 0$ (Fig. 2.9), β has minimal fluctuations at daily time scales, and α increases by 11% on average. However, when conditioning on areas with $OW/f^2 > 0.2$ (Fig. 2.10), daily calculated α and r^2 are enhanced by 36% and 30%, respectively.

These changes in the correlation coefficients based on OW conditions suggest that the intensity of wind–front interactions is visibly strengthened in filamentary strain regions as compared to the center of eddies. Yet, the estimates of coefficients in eddy centers are more representative of subdomain-averaged values (Fig. 2.9). In future observational campaigns, such as S-MODE (Farrar et al., 2020), estimation of domain-averaged wind–front interactions would require broad spatial measurements of surface velocity and temperature, covering multiple mesoscale and submesoscale eddies. More localized quantification of enhanced

Figure 2.9: wind–front feedback coefficients (Fig. 2.4) and 2D reconstruction accuracy (Fig. 2.4) calculations, conditioned on Okubo-Weiss parameter in vorticity dominated regime. (a) Comparison of subdomain-based and $OW/f^2 < 0$ conditioned α calculations in one- and fifteen-day time windows. (b) β calculated as in (a). (c) Pearson linear correlation coefficients squared (r^2) of the 2D reconstruction calculated with the same conditions and in the same time windows.

sub-mesoscale wind–front interaction requires persistent and collocated sampling in narrow filamentary structures. At the same time, in-situ Lagrangian measurements, such as surface drifters, have the propensity to converge at frontal regions, and therefore are subject to potentially misrepresenting and biasing estimations on average wind–front interaction intensity in the domain.

2.7.4 Analyses in the quiescent region

In the quiescent region of the Southern Ocean considered in this study (Fig. 2.1, left box), the same analyses of the 2D conditional mean (Fig. 2.2), wind stress curl reconstruction (Fig. 2.3), and temporal coefficient variability (Fig. 2.4) are conducted and shown here for comparison. Overall, despite differences in the surface Ro distributions (Fig. 2.1c,d), background energy levels (Fig. 2.1a), and the range of SST gradients between the two subdomains, the essence of the 2D conditional mean plot and our argument of the joint impact of wind–front interactions remain robust.

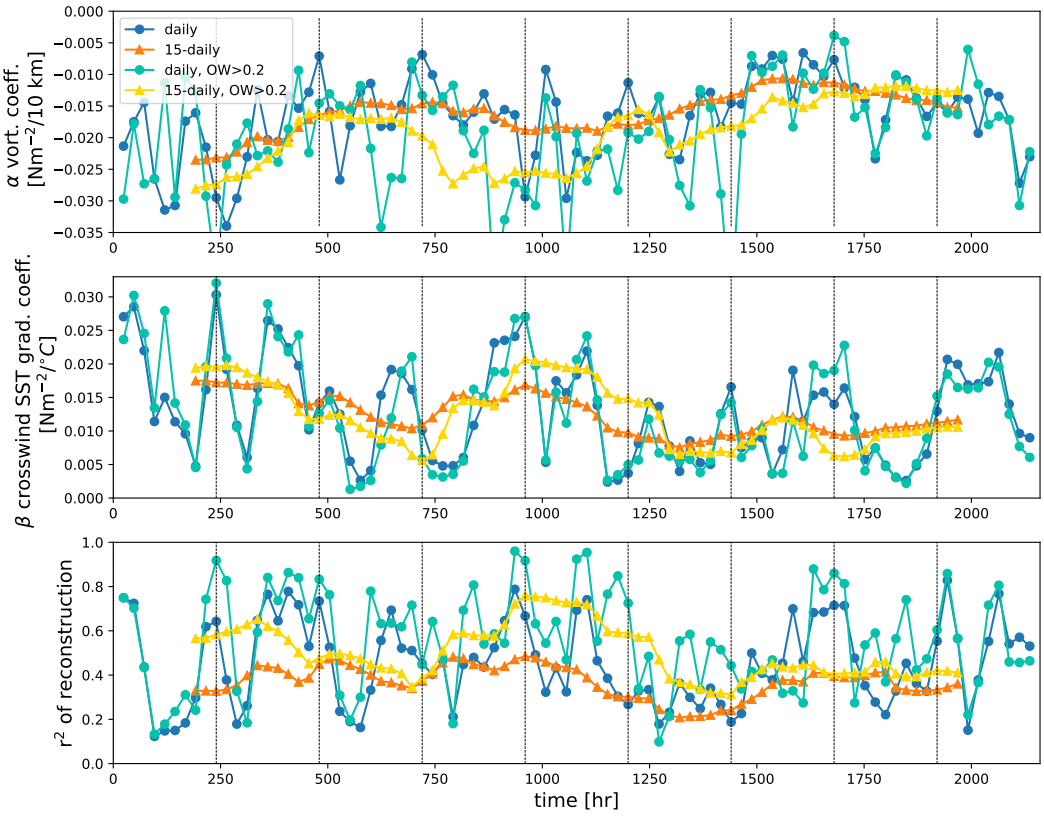

Figure 2.10: Same as in Fig. 2.9, but conditioned on Okubo-Weiss parameter in strain dominated regime, with $OW/f^2 > 0.2$.

Specifically, tilted zero-lines, an indication of the constructive and destructive interactions between CFB and TFB, are seen in Fig. 2.11a,d, even though the ranges of surface ocean vorticity/divergence and crosswind/downwind SST gradients in the quiescent regime are reduced by roughly a factor of 2. Therefore, wind stress curl reconstructions (Fig. 2.12) also require consideration of both the thermal and mechanical components. We again see alternating hourly reconstruction performances from 1D current and 1D thermal methods (Fig. 2.12k,l), both of which retain ∼6% more RMSE on average than the 2D dependent sum. The independent 1D current + thermal reconstruction, on the other hand, only generates ∼1% more error, implying that in the quiescent region, CFB and TFB might be more independent than in the energetic subdomain. The correlation between the coefficients and physical parameters such as 10 m wind speed and air–sea temperature difference also remain and even strengthen, compared with the energetic region (Fig. 2.13). This suggests that α and β coefficients are more linearly correlated with physical parameters when Ro is smaller and the motions are dominated by larger scales.

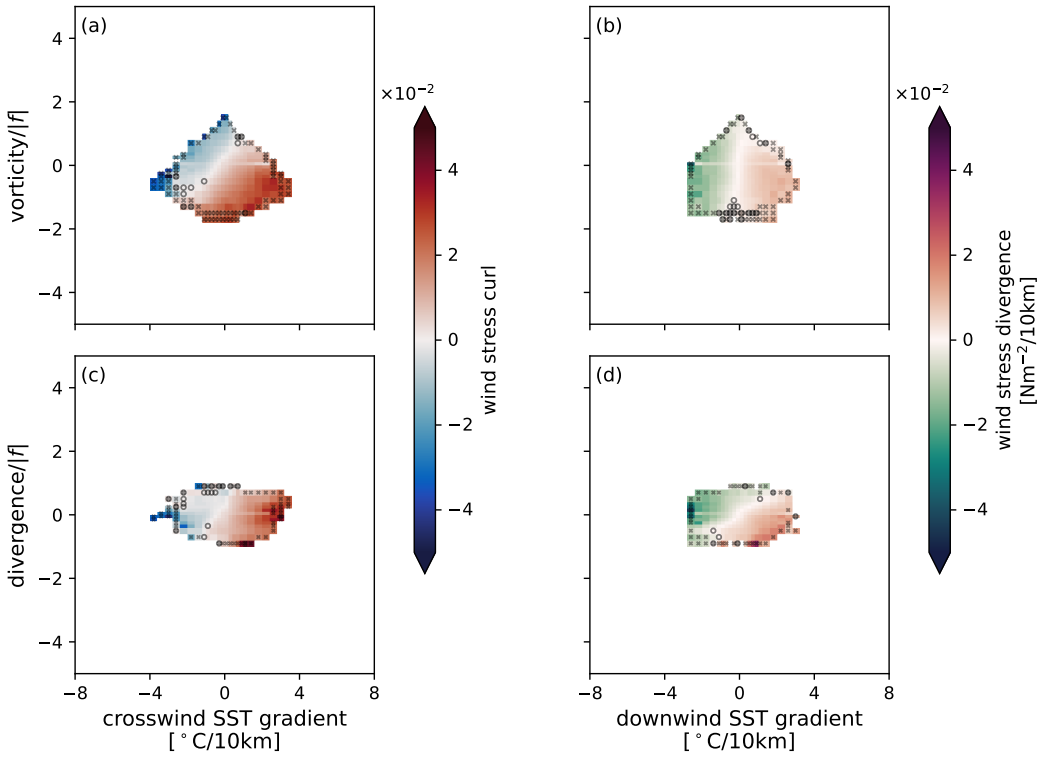

Figure 2.11: (quiescent subdomain) Conditional mean plots conditioned on surface ocean vorticity or divergence and crosswind or downwind SST gradients, colored by mean values of either wind stress curl or wind stress divergence. (a) The joint influence of vorticity and crosswind SST gradient on wind stress curl. (b) TFB from downwind SST gradient on wind stress divergence. (c) TFB from crosswind SST gradient on wind stress curl. (d) The joint influence of ocean divergence and downwind SST gradient on wind stress divergence. The slope of the zero-line (white in both colormaps) indicates the level of interaction and competition between surface vorticity/divergence and crosswind/downwind SST gradients in generating small-scale features in the wind stress fields.

Overall, the joint impact of current and thermal feedback applies in the quiescent region albeit with regional differences, as wind–front interactions are ubiquitous. More detailed spatial and temporal quantification of wind–front interactions are left for future work.

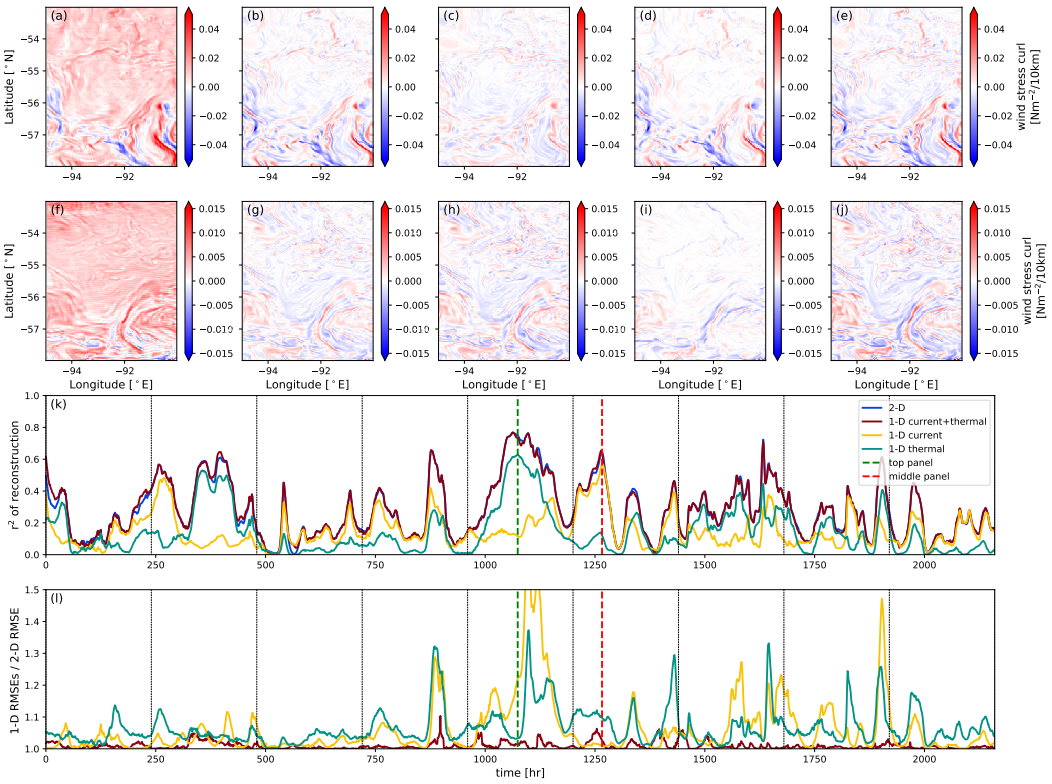

Figure 2.12: Same as in Fig. 2.3, but calculated in the quiescent subdomain (Fig. 2.1). Within the top two panels, from left to right are simulated wind stress curl (a,f), 2D reconstruction (b,g), 1D current reconstruction (c,h), 1D thermal (d,i), and 1D current + thermal (e,j).

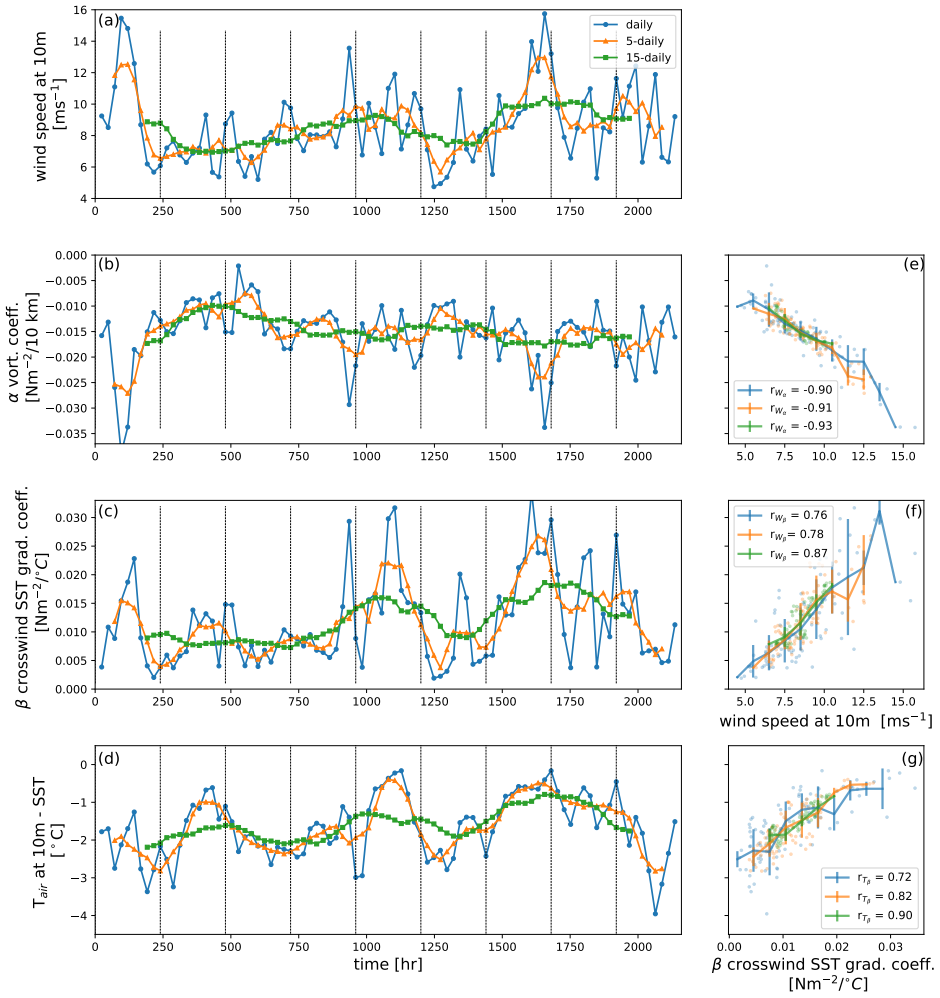

Figure 2.13: Variability and correlation of coefficients, α and β, and related physical properties, wind speed and air–sea temperature difference. (b) α; (c) β. (a) Wind speed and (d) air–sea temperature difference (air temperature at 10 m − SST) temporal variability are spatially averaged over the domain and over the same time period in which α and β are obtained. (e) correlation between wind speed and α with Pearson correlation coefficient r_{W_α}. (f) correlation between wind speed and β with Pearson correlation coefficient r_{W_β}. (g) correlation between air–sea temperature difference and β with Pearson correlation coefficient r_{T_β}.

Chapter 3

MESO- AND SUB-MESOSCALE WIND–FRONT INTERACTIONS AND THEIR IMPACTS ON OCEAN VERTICAL VELOCITIES

As a self-contained work, some notation may differ from conventions used elsewhere in this thesis.

3.1 Abstract

Coherent surface ocean temperature and velocity structures, with scales spanning 10 km to 100 km, induce surface wind stress anomalies that generate near-surface vertical velocities as a result of Ekman dynamics. The influence of these wind–front interactions on surface wind stress gradients, known as thermal (TFB) and current (CFB) feedbacks, have been studied extensively at $O(100)$ km scales. However, their relative contributions to ocean vertical velocities and their characteristic scales of variability remain underexplored. This study evaluates the impacts of TFB and CFB at $O(100)$ km and $O(10)$ km scales on Ekman vertical velocities using output from a global 4–6 km ocean–atmosphere coupled simulation, focusing on the California Current System. Total Ekman velocities are decomposed into a linear component related to wind stress curl and a nonlinear component involving ocean vorticity derivatives. At 30–200 km scales, linear and nonlinear Ekman velocities are of comparable magnitude, with TFB and CFB contributing similarly to the linear component. At <30 km scales, CFB induces $O(10)$ times stronger vertical transport than TFB linear components, yet nonlinear Ekman velocities dominate, exceeding linear terms by an order of magnitude and matching total near-surface vertical velocities. A decomposition of the nonlinear component reveals that the enhancement is driven by ocean vorticity gradients at <30 km scales. These results highlight the importance of resolving small-scale wind–front interactions and oceanic surface features that modulate upper ocean vertical velocities and, potentially, tracer and heat transport.

3.2 Introduction

Ekman pumping plays a critical role in upper-ocean exchange and biological productivity through the vertical transport of heat (Li et al., 2021), nutrients (He et al., 2017; Priyanka et al., 2025; Gaube et al., 2013), and carbon (Resplandy et al., 2019) — elements essential to climate regulation and marine ecosystems. At the oceanic mesoscale, $O(100)$ km, both observations and numerical simulations show that air–sea interactions significantly modulate Ekman velocities. Wind–front interactions refer to mechanical (current feedback, CFB) and thermodynamical (thermal feedback, TFB) feedback processes between the ocean surface and the atmospheric boundary layer, which can lead to substantial modifications of the surface wind stress field and, in turn, Ekman pumping. Surface wind stress curl anomalies

arising from CFB and TFB generate local vertical motions within the Ekman layer, commonly referred to as "linear Ekman velocities" (McGillicuddy et al., 2007; Gaube et al., 2015). In addition, CFB and TFB modify the wind stress field, which, when interacting with surface vorticity gradients, gives rise to "nonlinear Ekman velocities" (McGillicuddy et al., 2007; Stern, 1965; Wenegrat and Thomas, 2017) (see further discussion in Sec. 3.3.6). Using satellite observations, Gaube et al. (2015) decomposed linear Ekman velocities into CFB and TFB contributions via correlation-based partitioning of wind stress curl. Globally, CFB-driven linear velocities and nonlinear Ekman velocities dominate the full Ekman vertical velocities, except in energetic western boundary currents where TFB contributions become comparably strong. The relative importance of these feedbacks and their magnitudes, $O(10)$ [cm day^{-1}], were confirmed by Seo et al. (2016) using a 7-km coupled numerical simulation in the California Current System (CCS). These mesoscale Ekman pumping dynamics have also been linked to asymmetric chlorophyll patterns (He et al., 2016; Chelton et al., 2011a) and enhanced winter phytoplankton blooms (He et al., 2017).

Current feedback (CFB) and thermal feedback (TFB), collectively referred to as wind–front interactions, connect surface ocean properties to atmospheric surface wind stress and facilitate momentum and energy exchange across the air–sea interface. Both feedbacks have been extensively studied individually at the oceanic mesoscale of $O(100)$ km. For the TFB process, sea surface temperature (SST) gradients alter lower atmospheric stability, inducing eddy-scale variations in vertical momentum fluxes and surface wind stress (e.g., Small et al., 2008; Strobach et al., 2022; Chelton and Xie, 2010). Early satellite-based studies resolving $O(100)$ km variability (Chelton et al., 2004, 2007; O'Neill et al., 2010, 2012) identified approximately linear relationships between wind stress curl and crosswind SST gradients, as well as between wind stress divergence and downwind SST gradients. More recently, Renault et al. (2024) demonstrated that TFB extracts energy from the ocean's potential energy reservoir and acts as a sink for baroclinic energy conversion. For CFB, the relative velocity difference between surface winds and currents, caused by coherent mesoscale features, establishes a negative correlation between ocean surface vorticity ζ and wind stress curl (e.g., Renault et al., 2016b; Rai et al., 2021). CFB analyses at mesoscale have focused on ocean vorticity, excluding correlations with ocean surface divergence (Renault et al., 2018), as ocean currents are largely geostrophic at these scales and approximately non-divergent (Barkan et al., 2019; Callies et al., 2020; Pedlosky, 1987). Observational and numerical studies (Seo et al., 2016; Renault et al., 2016b, 2019; Eden and Dietze, 2009; Rai et al., 2025) have shown that mesoscale eddies drain oceanic kinetic energy via the generation of negative wind work integrated over eddies.

Recent high-resolution air–sea coupled simulations have begun to resolve $O(10)$ km submesoscale oceanic processes that reveal how CFB and TFB change with scale as well as the interaction of these two processes. Bai et al. (2023) have shown that wind stress curl associated with air–sea interactions is enhanced by an order of magnitude at sub-mesoscale

compared to mesoscale. This is because CFB and TFB remain linear beyond mesoscale at $O(100)$ km scales (Bai et al., 2023), so the intensification of wind stress curl scales linearly with the sharpened velocity and temperature gradients at the oceanic sub-mesoscale of $O(10)$ km (Bai et al., 2023; Conejero et al., 2024; Renault et al., 2024; Strobach et al., 2022). In addition, at sub-mesoscale where ocean surface divergence has the same order of magnitude as vorticity (Callies et al., 2020; Barkan et al., 2019), a negative correlation is found between ocean divergence and wind stress divergence (Bai et al., 2023; Conejero et al., 2024). At both meso- and sub-mesoscales, numerical studies (Bai et al., 2023; Conejero et al., 2024) demonstrate that CFB and TFB interact constructively and destructively, jointly modulating the surface wind stress gradients. Neglecting their combined influence leads to inaccurate quantification of the correlation coefficients associated with CFB and TFB.

While understanding of wind–front interactions has extended to include $O(10)$ km submesoscale dynamics, their contributions to Ekman vertical velocities remains under-explored. Enhanced wind stress curl associated with air–sea interactions (Bai et al., 2023; Conejero et al., 2024) may intensify both CFB- and TFB-induced linear Ekman pumping. Nonlinear Ekman velocities are also expected to strengthen due to sharper surface velocity gradients arising from submesoscale frontogenesis and mesoscale strain (Barkan et al., 2019; McWilliams, 2016). Thus, sub-mesoscale wind–front interactions may generate Ekman vertical velocities, from both linear and nonlinear contributions, that may exceed the magnitudes previously recognized due to interactions with mesoscale features. Quantifying these velocities at sub-mesoscale, and comparing them with their mesoscale counterparts (Seo et al., 2016; Gaube et al., 2015), is essential for determining their contribution to the vertical motions near the ocean surface.

Beyond quantifying these velocities, a key challenge lies in partitioning nonlinear Ekman velocities into contributions from CFB, TFB, and ocean surface structures. Nonlinear Ekman velocities arise from the interaction between wind stress and surface vorticity gradients. However, the wind stress itself is modified by air–sea feedbacks during the generation of wind stress curl. At sub-mesoscale ($O(10)$ km), both air–sea coupling (Bai et al., 2023; Conejero et al., 2024) and surface vorticity gradients (Callies et al., 2020; Barkan et al., 2019) intensify, raising the question of whether wind–front interactions or ocean surface variability plays the dominant role in setting vertical velocities at previously unexplored scales. Gaining insight into the relative roles of air–sea feedbacks and ocean surface vorticity structure is important for linking observed surface fields to vertical motions, with broad relevance for interpreting high-resolution satellite data and inferring vertical transport processes in the upper ocean.

In this study, existing gaps in understanding sub-mesoscale Ekman velocities and the decomposition of nonlinear Ekman pumping are addressed. Results based on spatially separated

fields (Sec. 3.3.2) highlight the importance of resolving $O(10)$ km submesoscale dynamics at the air–sea interface (Sec. 3.4.1,3.4.2). Nonlinear Ekman velocities at these scales are found to be at least an order of magnitude stronger than their $O(100)$ km counterparts (Sec. 3.4.3), primarily driven by gradients in ocean surface vorticity (Sec. 3.4.4). Notably, these nonlinear Ekman velocities, inferred solely from surface fields, reproduce the general magnitude and structure of total vertical velocities at the base of the Ekman layer (Sec. 3.4.5), indicating a distinct dynamical regime in which surface Ekman pumping is predominantly governed by small-scale ocean surface variability.

3.3 Methods

3.3.1 Ocean-atmosphere coupled simulation and the domain of interest

In this study, we use hourly averaged output from a global, state-of-the-art, atmosphere–ocean coupled simulation, referred to as C1440-LLC2160 (Torres et al., 2022b). The simulation couples the Goddard Earth Observing System (GEOS) and the Massachusetts Institute of Technology (MIT) general circulation model (MITgcm, Marshall et al. (1997)). The atmospheric component is run with the C1440 cubed-sphere grid that has a nominal horizontal grid spacing of 6.9 km and 72 hybrid sigma-pressure vertical levels. The oceanic component of the simulation is on the Latitude-Longitude-Cap 2160 grid (Forget et al., 2015), and has a horizontal grid spacing of 1/24°, approximately ∼4 km around the coast of California. The coupling between the two components is enabled by information exchange every 45 model seconds. The simulation was initialized with ocean initial conditions on January 20th in 2012 and concluded in March, 2013. Results shown below use model outputs from March 1 to May 31, 2012. Additional information about the model configuration and experiment setup can be found in Torres et al. (2022b).

The domain of interest is the California Current System (CCS), an eastern boundary upwelling system that sustains one of the most productive coastal marine ecosystems globally (Chavez and Messié, 2009). Equatorward winds induce coastal Ekman upwelling along the California coast (Combes et al., 2013; Villas Bôas et al., 2017), bringing cold, nutrient-rich waters to the surface and generating strong vertical velocities essential for nutrient replenishment and biological productivity (Checkley Jr and Barth, 2009). Ekman-induced velocities exhibit a clear seasonal cycle, typically peaking in spring and summer (Renault et al., 2016a), during which the results of this study are derived. Dynamically, the CCS is characterized by the presence of offshore mesoscale eddies, shed from the coast, and ample sub-mesoscale fronts and filaments near the coast (Seo et al., 2016). Large-scale SST anomalies and gradients form as cold, upwelled waters displace warmer surface waters. These dynamics precondition the region for wind–front interactions, which contribute to vertical velocities at mesoscale and further modify surface ocean dynamics (Seo et al., 2016; Gaube et al., 2015). Furthermore, this region coincides with the sampling site of NASA's Sub-Mesoscale Ocean Dynamics Experiment (S-MODE) (Farrar et al., 2025), offering opportunities to integrate

high-resolution observations with numerical simulations in future work.

3.3.2 Spatial and temporal filters

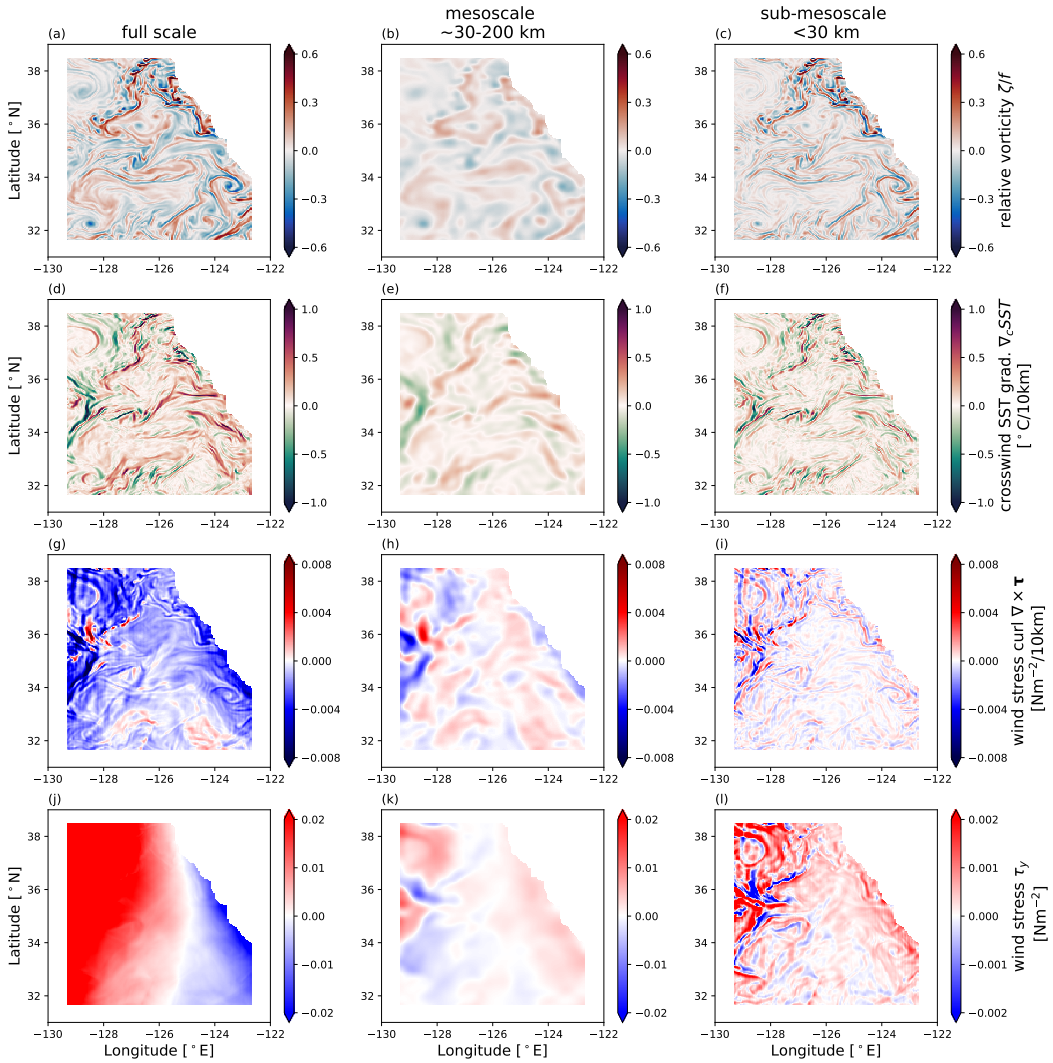

Figure 3.1: Illustration of spatial filtering and scale separation of model output. Snapshots are taken at 8:00 am on April 8th, 2012 after applying a one-day running mean to remove high-frequency noise. Simulated, nondimensionalized ocean surface relative vorticity ζ/f (first row, a-c), crosswind SST gradients $\nabla_c SST$ (second row, d-f), surface wind stress curl $\nabla \times \boldsymbol{\tau}$ (third row, g-i), and surface meridional wind stress τ_y (bottom row, j-l) are shown with no filtering (left column), with a mesoscale filter ($\sim$ 30-200 km; middle column), and with a sub-mesoscale filter ($<$ 30 km; right column). Note that the color bar range for surface wind stress is an order of magnitude smaller at sub-mesoscale. The filtering approach that isolates these scales is described in Sec. 3.3.2.

To examine and compare the intensity of wind–front interactions and associated Ekman vertical velocities at mesoscale and sub-mesoscale spatial resolutions, spatial filters are applied to all relevant atmospheric and oceanic fields (Fig. 3.1), including ocean surface vorticity ζ, directional SST gradients, and wind stress curl, $\nabla \times \boldsymbol{\tau}$. Directional SST gradients include crosswind SST gradient $\nabla_c SST \equiv \boldsymbol{\nabla} SST \times \hat{\boldsymbol{\tau}}$, in which the winds are aligned with the front,

and downwind SST gradient $\nabla_d SST \equiv \boldsymbol{\nabla} SST \cdot \hat{\boldsymbol{\tau}}$, where the winds are perpendicular to the frontal direction. The unit vector in the direction of wind stress is given by $\hat{\boldsymbol{\tau}} \equiv \frac{\boldsymbol{\tau}}{|\boldsymbol{\tau}|}$. Two approaches exist for applying spatial filters to fields involving products of terms, as required in the calculation of nonlinear Ekman velocities (Sec. 3.3.6). The key distinction lies in the order of operations: one can either (1) compute the product terms first and then apply the spatial filter, or (2) apply the filter to the individual fields before computing their products. Consistent with prior air–sea interaction studies (Renault et al., 2019; Conejero et al., 2024) and with spatial filtering methods (Aluie et al., 2018), the first approach is adopted here, in which all spatial filtering and convolution are performed after the necessary derivatives and product fields are computed. This choice preserves correlations between derivative fields, which are essential for diagnosing wind–front interactions, and retains the cross terms in the product fields. Although the second approach may be more effective at minimizing spatial scale aliasing, since all raw fields are filtered prior to differentiation, it eliminates the cross terms within the product fields and therefore yields incomplete results.

Spatial filtering reveals that sub-30 km oceanic features leave a distinct imprint on atmospheric wind fields. To begin, a one-day running mean is applied to all fields to remove high-frequency transient motions. The "sub-mesoscale" range is isolated using a high-pass Gaussian filter with a cutoff near 30 km. Mesoscale fields, spanning approximately 30–200 km, are extracted using a band-pass Gaussian filter. Visual inspection of the wind stress curl (Fig. 3.1g–i) and surface wind stress fields (Fig. 3.1j–l) reveals that variability at scales <30 km share strong spatial resemblance to ocean surface relative vorticity and crosswind SST gradients (Fig. 3.1c,f). Although the surface wind stress is dominated by the large-scale background fields (Fig. 3.1j), <30 km features emerge from coupling with ocean surface vorticity and SST gradients. However, as shown later (Sec. 3.4.4), this wind–front coupling has limited impact on the generation of sub-30 km nonlinear Ekman velocities; instead, gradients in ocean surface vorticity are the dominant driver of nonlinear Ekman velocities that sub-30 km scales.

3.3.3 Total Ekman velocity estimation

The ocean interior is influenced by spatial variations in the surface wind stress through Ekman pumping; this multi-scale process spans basin scales that govern the subtropical and subpolar gyres, to individual meso- and sub-mesoscale eddies. The total Ekman-induced vertical velocity is estimated following Stern (1965) and Gaube et al. (2015) as:

$$w_{\text{total}} = \frac{1}{\rho_0}\mathbf{k} \cdot \left[\nabla \times \left(\frac{\boldsymbol{\tau}}{f+\zeta}\right)\right], \tag{3.1}$$

in which $\mathbf{k} = (0, 0, 1)$ is the unit vector in the vertical direction. This total Ekman velocity can be decomposed into two components assuming that the meridional variation of f is negligible,

$$w_{\text{total}} \approx \frac{1}{\rho_0}\mathbf{k} \cdot \left[\underbrace{\frac{\nabla \times \boldsymbol{\tau}}{(f+\zeta)}}_{w_{\text{L,total}}} + \underbrace{\frac{1}{(f+\zeta)^2}(\tau^x \frac{\partial \zeta}{\partial y} - \tau^y \frac{\partial \zeta}{\partial x})}_{w_{\text{NL,total}}} \right]. \tag{3.2}$$

Here, $\rho_0 = 1025$ kg m^{-3} is assumed constant, f represents the Coriolis parameter, the surface wind stress $\boldsymbol{\tau}$ has zonal and meridional components τ^x and τ^y, and $\zeta = \frac{\partial v}{\partial x} - \frac{\partial u}{\partial y}$, the vertical component of ocean surface relative vorticity. The first term in Eq. 3.2 is conventionally referred to as the "linear Ekman vertical velocity," which is associated with the wind stress curl, but also includes a vorticity correction in the denominator. The second term arises from interactions between the surface wind stress and horizontal gradients of surface relative vorticity (Gaube et al., 2015; Seo et al., 2016; Oerder et al., 2024), which can generate an Ekman upwelling/downwelling dipole within an eddy. This term is the vorticity gradient-induced Ekman pumping (Stern, 1965), and is commonly referred as the "nonlinear Ekman vertical velocity."

An important assumption underlying Eq. 3.2 is that both the flow Rossby number $\frac{U}{fL}$ and the Ekman Rossby number $\frac{U_E}{fL}$ are much smaller than 1. Here, U_E is the undisturbed Ekman velocities assuming a balance between only the Coriolis term and surface frictional stress (Wenegrat and Thomas, 2017), and L represents a characteristic horizontal length scale. An ageostrophic Rossby number is also defined here as $\frac{U_a}{fL}$, in which $U_a = U_0 - U_g$ is the total surface ageostrophic velocities by subtracting the surface geostrophic flow U_g from the surface flow U_0. The ageostrophic Rossby number serves as an upper bound on the Ekman Rossby number, as ageostrophic flow includes non-Ekman components. Assuming a constant Ekman layer depth of 48 m, based on Chereskin (1995), the Ekman and ageostrophic Rossby number are estimated to be O(0.01-0.1) (see Appendix A), which confirms the applicability of Eq. 3.2.

3.3.4 Wind stress curl decomposition into CFB and TFB contributions

To isolate the contributions of CFB and TFB to Ekman velocities, the surface wind stress curl is first partitioned into SST- and current-induced components based on correlations between surface ocean features and surface wind stress curl. Specifically, wind–front-induced surface wind stress curl is reconstructed using the following linear relation:

$$\nabla \times \boldsymbol{\tau} \approx \alpha \frac{\zeta}{f} + \beta \nabla_c SST, \tag{3.3}$$

where α [N m^{-2}/10 km] represents the CFB-related correlation between nondimensionalized surface vorticity ζ/f and wind stress curl, and typically takes on negative values due to

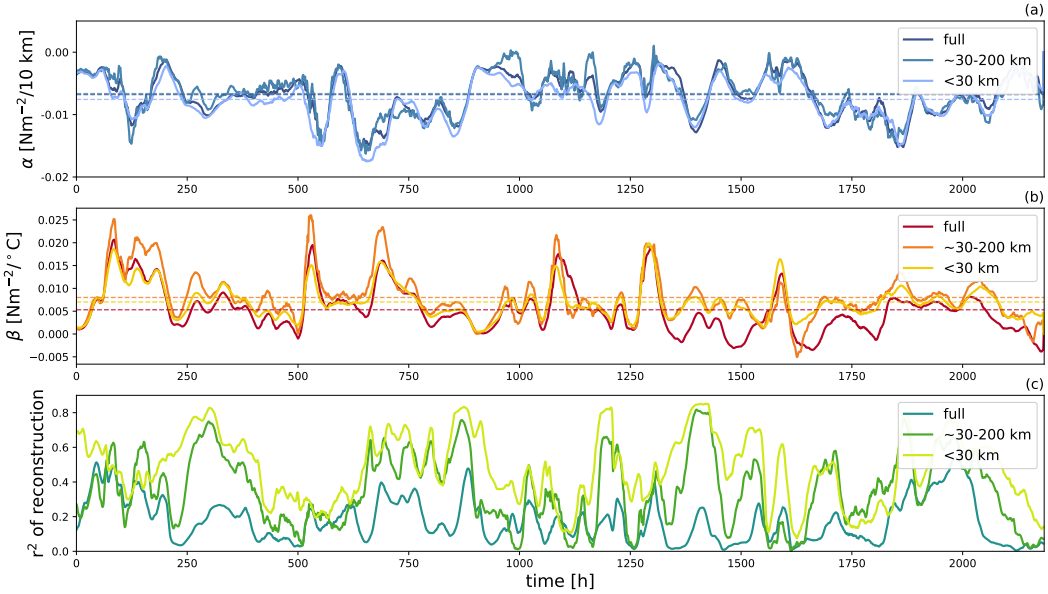

Figure 3.2: March-April-May time series of current α and thermal β feedback coefficients and reconstruction success calculated for unfiltered fields as well as mesoscale filtered (30-200 km), and sub-mesoscale filtered (<30 km). (a) The coupling coefficient α linking ocean surface vorticity ζ and surface wind stress curl, at three scales. Horizontal dashed lines are the temporal averages at three scales. (b) The coupling coefficient β linking ocean surface crosswind SST gradient $\nabla_c SST$ and wind stress curl, at three scales. Horizontal dashed lines are the temporal averages at three scales. (c) Pearson linear correlation coefficients squared (r^2) of the reconstruction of wind stress curl, at three scales. Note that α and β are calculated jointly to account for interactions between CFB and TFB.

their inverse relationship. β [N m^{-2}/°C] represents the TFB-related correlation between the crosswind SST gradient ∇_cSST and wind stress curl, and is generally positive. The units of α and β are chosen to highlight effects of $O(10)$ km eddies or frontal structures. This decomposition follows methodologies used in previous observational and modeling studies (Seo et al., 2016; Gaube et al., 2015), which rely on empirical linear relationships between derivatives of SST, ocean current fields, and wind stress curl. However, in this study, α and β are solved jointly by inverting a matrix of collocated vorticity and crosswind SST gradient values against the wind stress curl field. This approach accounts for constructive and destructive interactions between CFB and TFB (Bai et al., 2023), and better captures their combined influence on wind stress curl (Fig. 3.3).

Estimates of α and β can either highlight temporal or spatial variability. Temporal variability underscores how the relative contributions of surface ocean vorticity and crosswind SST gradients change in time. These changing contributions from CFB and TFB are also correlated with surface wind speed and the air–sea temperature difference (Bai et al., 2023). To examine temporal variability, α and β are computed hourly at each grid point and then averaged over the Fig. 3.1 domain (Bai et al., 2023, Fig. 3.2); time series are considered for unfiltered model output as well as fields filtered at 30-200 km and $<$ 30 km scales. To examine spatial variability, α and β are computed as a three-month time mean at each grid

point, which provides a seasonally averaged spatial map of α and β (Conejero et al., 2024, Fig. 4). Overall, the temporal variations of α and β, filtered at different spatial scales, behave similarly (Fig. 3.2a,b). However, the percentage of wind stress curl variance that can be explained by air–sea interactions alone does depend on spatial scale, with more variance explained at smaller spatial scales (Fig. 3.2c). Further discussion of the temporal variability appears in Sec. 3.4.1. While α is spatially uniform, β values with large magnitudes are localized along fronts and filaments; this is discussed further in Appendix B.

3.3.5 Linear Ekman pumping decomposition

Linear Ekman vertical velocities are partitioned into contributions from TFB and CFB based on their respective modifications to wind stress curl. This separation follows the decomposition of wind stress curl into CFB- and TFB-induced components described in Sec. 3.4.2. Specifically, vertical velocities attributed to linear CFB and TFB are defined as:

$$w_{\mathrm{L,CFB}} \equiv \frac{\alpha\zeta}{\rho_o(f+\zeta)}, \qquad w_{\mathrm{L,TFB}} \equiv \frac{\beta\nabla_c SST}{\rho_o(f+\zeta)}. \tag{3.4}$$

This approach follows Seo et al. (2016); Gaube et al. (2015), however, instead of relying on fixed correlation coefficients derived from isolated feedbacks, the present method employs time-varying coefficients α and β (Fig. 3.2a,b) that capture the joint influence of CFB and TFB (Sec. 3.4.2). These coefficients are updated hourly across the domain to account for the high temporal variability associated with $O(10)$ km processes. The use of temporal means or constant values (Fig. 3.2a,b, dashed lines) both under- and overestimate outcomes of wind stress curl reconstructions and therefore Ekman vertical velocities per hour. The magnitude of temporally varying coefficients at < 30 km scales on average deviate from the mean values by 34% for α and 38% for β. Wind stress curl components that arise from processes unrelated to wind–front interactions also generate vertical motions, but these are not considered in this study.

3.3.6 Nonlinear Ekman pumping decomposition

While previous studies (Gaube et al., 2015; Seo et al., 2016) include the non-linear component in their estimates of Ekman vertical velocities, this quantity has not, to our knowledge, been decomposed into contributions from air–sea coupling and surface ocean vorticity. Traditionally, $w_{\mathrm{NL,total}}$ (in Eq. 3.2) has been associated with gradients in surface ocean vorticity, which sharpen progressively at $O(100)$ km and $O(10)$ km scales (Callies et al., 2020; Barkan et al., 2019; Capet et al., 2008b). However, at these scales, air–sea coupling also increasingly influences surface wind stress variability (Bai et al., 2023; Conejero et al., 2024). The relative impact of air–sea interactions and of the surface ocean vorticity gradients remains unconstrained. A decomposition of $w_{\mathrm{NL,total}}$ would offer insight into the relative impact of wind–front interactions and ocean vorticity gradients on vertical transport, particularly at $O(10)$ km scales, where both mechanisms become more pronounced. However, the decomposition of nonlinear Ekman velocities is less straightforward than its linear counterpart

(Sec. 3.4.3) because both TFB and CFB influence wind stress gradients, not the surface wind stress, which appears in the conventional form of $w_{\mathrm{NL,total}}$ (Eq. 3.2).

We propose the following $w_{\mathrm{NL,total}}$ decomposition that highlights correlations between wind stress curl, surface ocean SST and currents, while separating out the impact of ocean surface vorticity gradients. Re-writing $w_{\mathrm{NL,total}}$ in Eq. 3.2 using integration by parts, we have:

$$w_{\mathrm{NL,total}} = \frac{1}{\rho_0(f+\zeta)^2}\left[\frac{\partial}{\partial y}(\tau^x\zeta) - \frac{\partial}{\partial x}(\tau^y\zeta) + \zeta(\nabla\times\boldsymbol{\tau})\right]. \tag{3.5}$$

This form permits a decomposition of the last term into SST-induced and current-induced components using Eq. 3.3. We denote the first two terms as wind-stress-induced nonlinear Ekman velocity, or $w_{\mathrm{NL},\tau}$; these terms are calculated with surface wind stress fields that are spatially filtered, but not decomposed into wind–front interaction contributions. This implies that the CFB- and TFB-induced vertical velocity decomposition is incomplete, and the limitations of Eq. 3.3 are discussed later in Sec. 3.5.3.

Summarizing the decomposition, $w_{\mathrm{NL,total}}$ can be written as:

$$\begin{aligned}
w_{\mathrm{NL,total}} &\approx w_{\mathrm{NL},\tau} + w_{\mathrm{NL,CFB}} + w_{\mathrm{NL,TFB}},\\
w_{\mathrm{NL},\tau} &\equiv \frac{1}{\rho_0(f+\zeta)^2}\left[\frac{\partial}{\partial y}(\tau^x\zeta) - \frac{\partial}{\partial x}(\tau^y\zeta)\right],\\
w_{\mathrm{NL,CFB}} &\equiv \frac{1}{\rho_0(f+\zeta)^2}\zeta(\alpha\zeta),\\
w_{\mathrm{NL,TFB}} &\equiv \frac{1}{\rho_0(f+\zeta)^2}\zeta(\beta\nabla_c SST).
\end{aligned} \tag{3.6}$$

Hereafter, all references to $w_{\mathrm{NL,total}}$ are based on Eq. 3.6.

3.4 Meso- v.s. Sub-mesoscale Wind–Front Interactions and Ekman Vertical Velocities

3.4.1 Temporal variability of α and β coefficients

Features at scales <30 km explain the largest fraction of the corresponding wind stress curl variance based on the temporal evolution of the spatially averaged joint coupling coefficients, $\alpha(t)$ and $\beta(t)$ (Fig. 3.2c). The coefficients and linear wind stress curl reconstruction are calculated for different scales. For example, the mesoscale wind stress curl is approximated as $\nabla\times\boldsymbol{\tau}_{\mathrm{meso}} \sim \alpha_{\mathrm{meso}}\zeta_{\mathrm{meso}} + \beta_{\mathrm{meso}}\nabla_c SST_{\mathrm{meso}}$. The scale-separated coefficients exhibit consistent trends in their variation and differ by less than 20% and 39% for α and β, respectively (Fig. 3.2a,b). In contrast, the reconstruction accuracy, measured by the squared Pearson correlation coefficient (r^2) between the reconstructed and simulated wind stress curl fields at each spatial scale, improves significantly when using scale-separated inputs (Fig. 3.2c). Improvements over the unfiltered reconstructions occur in 84% of times for 30–200 km scales and in 98% of cases for <30 km scales during March, April, and May. Specifically, recon-

structions of 30–200 km and <30 km wind stress curl fields exhibit an average r^2 enhancement of 202.5% and 433.3%, respectively, relative to reconstructions using unfiltered fields (Fig. 3.2c). These results suggest that the ability to reconstruct variations in surface wind stress curl is limited when all scales are considered together, which is likely due to the influence of processes beyond air–sea interactions. At scales ≤200 km, variability in surface atmospheric wind stress curl is largely governed by and responsive to wind–front interactions with ocean surface currents and SST.

3.4.2 Enhanced wind stress anomalies at sub-mesoscale

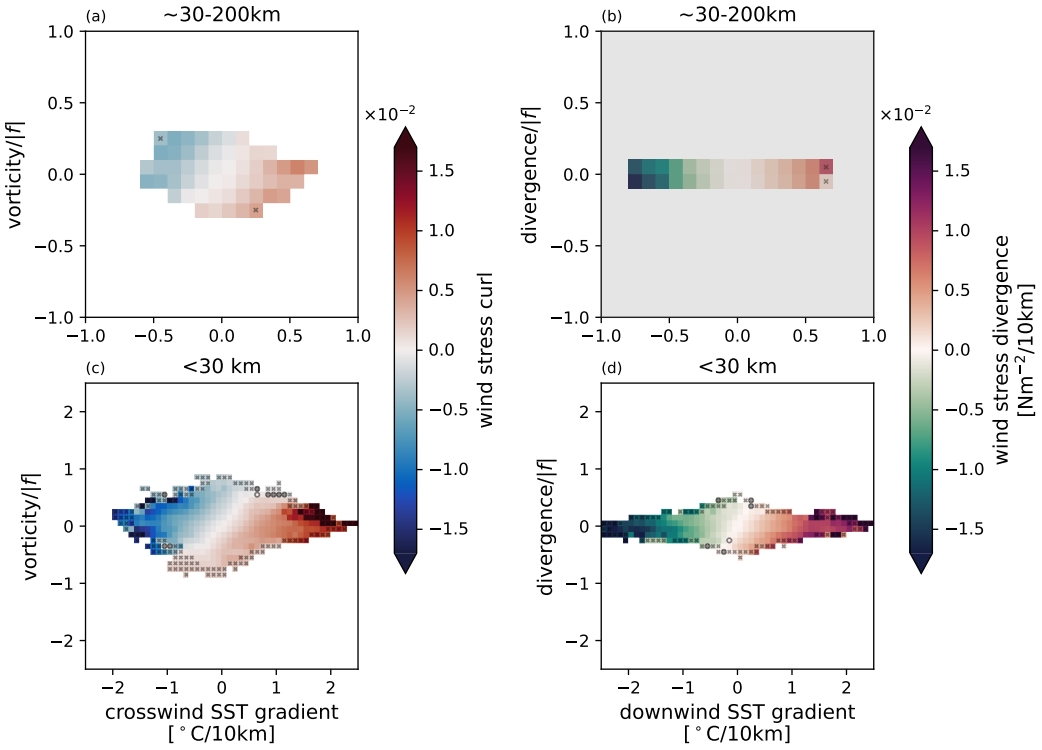

Figure 3.3: Meso- and sub-mesoscale conditional mean plots in the CCS domain for March, April, and May. Conditional averages of wind stress curl or wind stress divergence (color) are based on surface ocean vorticity and crosswind SST gradients or surface ocean divergence and downwind SST gradients. Cross marks indicate bins with less than 50 points after removing data outside of mean ±1 standard deviation. Circles indicate bins with standard error that is larger than the mean value. (a) The joint influence of mesoscale (~30-200 km) vorticity and crosswind SST gradient on wind stress curl. (b) The joint influence of mesoscale (~30-200 km) ocean surface divergence and downwind SST gradient on wind stress divergence. (c) As in panel (a), but for sub-mesoscale (<30 km). (d) As in panel (b), but for sub-mesoscale (<30 km). Note that in (b), at oceanic mesoscale, surface flows are largely divergence-free, so mesoscale wind stress divergence is predominantly determined by downwind SST gradient. This panel is therefore grayed out as there is no joint CFB and TFB interactions.

Anomalous values of eddy-scale wind stress gradients are generated almost exclusively at sub-30 km scales based on conditional mean plots (Fig. 3.3) conditioned on ocean velocity and SST gradients. Calculations of conditional mean plots follow the methodology detailed

in Bai et al. (2023) and Conejero et al. (2024). Over monthly to seasonal timescales, CFB and TFB jointly modify surface wind stress curl at both 30–200 km and <30 km scales, as indicated by the slanted zero-contour in (Fig. 3.3a,c,d) At sub-30 km scales, surface velocity and SST gradients are intensified, resulting in an expanded parameter space–expanding to a region at least four times larger than at mesoscale (Fig. 3.3a,c). These sub-mesoscale surface features generate more extreme wind stress curl anomalies; wind stress curl magnitudes are up to four times greater than at mesoscale. These interactions leave a clear imprint of sub-mesoscale ocean structures on the surface wind stress and its spatial gradients (Fig. 3.1). A similar pattern is observed in wind stress divergence at sub-30 km scales (Fig. 3.3d), where a tilted zero-contour indicates joint control from surface wind stress divergence and downwind SST gradients. At 30–200 km scales, where ocean flows are approximately geostrophic and non-divergent, wind stress divergence associated with wind–front interactions are primarily attributed to TFB, consistent with the vertically oriented zero-contour (Fig. 3.3b). The relative contribution from CFB in this study appears weaker than in Conejero et al. (2024) and in the energetic regime of Drake Passage, Southern Ocean in Bai et al. (2023). This discrepancy may arise from the higher spatial resolution (∼1 km) used in Conejero et al. (2024), which better resolves intense surface vorticity features, and from the stronger eddy activity in the Antarctic Circumpolar Current (Bai et al., 2023). The magnitude of wind stress curl anomalies and the relative strength of TFB and CFB in this CCS study resemble those in the quiescent region of the Southern Ocean examined in Bai et al. (2023), and provides additional evidence that resolving sub-mesoscale features more significantly alters the surface wind field variability as compared to mesoscale-resolving studies (Renault et al., 2016b; Seo et al., 2016).

In Sec. 3.4.4, it will be shown that, despite the enhanced $O(10)$ km wind stress curl associated with CFB and TFB, the influence of these air–sea processes on w_{total}, and especially on $w_{\mathrm{NL,total}}$, is small compared to the contribution from surface vorticity gradients.

3.4.3 Linear Ekman velocities induced by wind–front interactions

Ekman vertical velocities due to mesoscale wind–front interactions have roughly equal contributions from SST-induced $w_{\mathrm{L,TFB}}$ and current-induced $w_{\mathrm{L,CFB}}$ linear Ekman components (Fig. 3.4). These vertical velocities are calculated following the definitions in Eq. 3.4. The similarity in magnitude between TFB and CFB contributions is observed throughout the CCS domain, regardless of the distance from the coast (Fig. 3.4g). Both $w_{\mathrm{L,TFB}}$ and $w_{\mathrm{L,CFB}}$ increase in magnitude closer to the coast, contributing to the coastal upwelling zone. At mesoscale, the total nonlinear Ekman vertical velocity, $w_{\mathrm{NL,total}}$ calculated following Eq. 3.6, is of comparable magnitude to the linear components (Fig. 3.4b,g), and exhibits similar large-scale spatial patterns. This result is consistent with previous observational and modeling studies (Gaube et al., 2015; Seo et al., 2016), and supports the prevailing view that nonlinear Ekman pumping has a secondary or at most comparable influence relative to linear

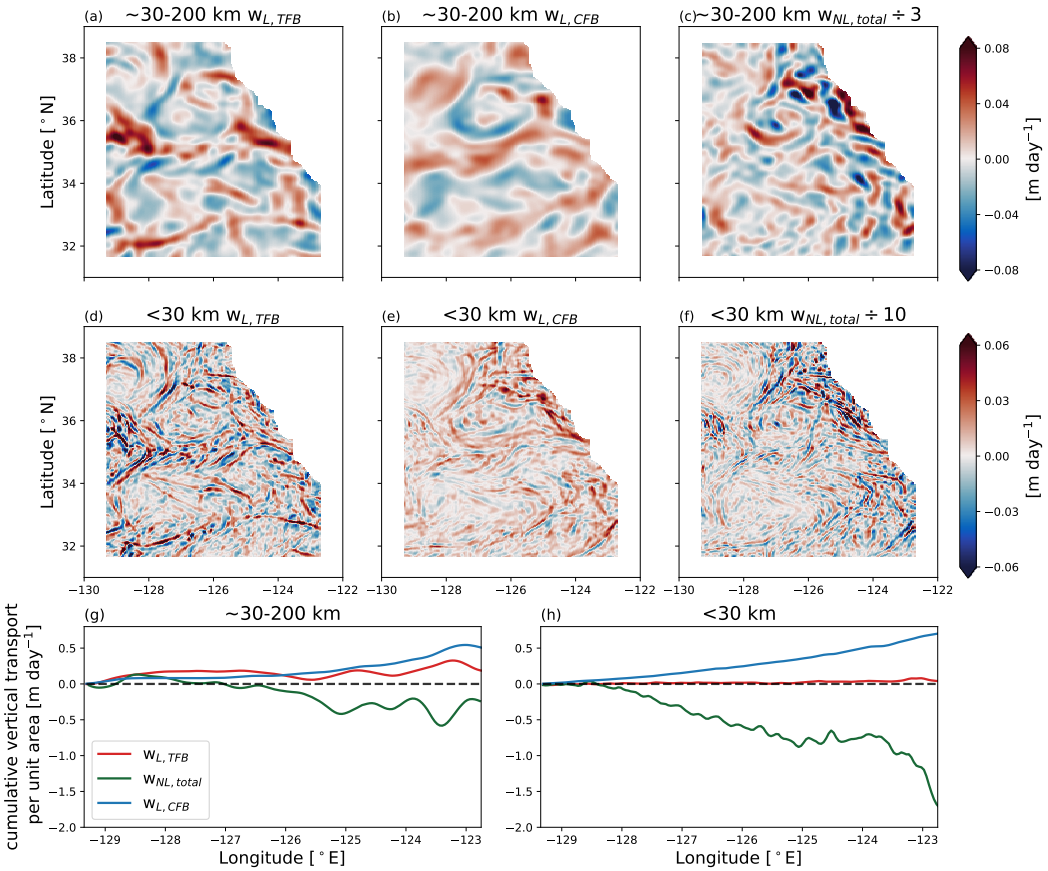

Figure 3.4: Comparison of linear Ekman velocity components with the total nonlinear Ekman velocities in the California Current System averaged during March, April, and May. Linear Ekman velocities are decomposed into $w_{\mathrm{L,TFB}}$, the SST-induced component, and $w_{\mathrm{L,CFB}}$, the current-induced component (Eq. 3.4). Total nonlinear Ekman velocities is $\mathrm{w}_{NL,total}$ from Eq. 3.6. (a)-(c) Seasonal mean vertical velocity at mesoscale for each component. (d)-(f) Seasonal mean vertical velocity at sub-mesoscale scale for each component. Cumulative vertical transport per unit area as a function of longitude at (g) mesoscale and (h) sub-mesoscale, with $w_{\mathrm{NL,total}}$ in green, $w_{\mathrm{L,CFB}}$ in blue, and $w_{\mathrm{L,TFB}}$ in red. Note that the magnitude of $\mathrm{w}_{NL,total}$ at both meso- (factor of 3) and at sub-mesoscale (factor of 10) have been reduced to use the same colorbar range as the linear components, but in the cumulative transport calculation $\mathrm{w}_{NL,total}$ is not re-scaled.

Ekman dynamics. The relative magnitudes of mesoscale $w_{\mathrm{NL,total}}$ compared with the linear components in this study are somewhat larger than those reported by Gaube et al. (2015) and Seo et al. (2016), likely due to the higher spatial resolution of the coupled simulation used here.

At sub-30 km scales, a regime that has been largely unexplored, nonlinear Ekman vertical velocities ($w_{\mathrm{NL,total}}$) emerge as the leading-order contribution and dominate over their linear counterparts, in contrast to the mesoscale regime. Although all three submesoscale components ($w_{\mathrm{L,TFB}}$, $w_{\mathrm{L,CFB}}$, and $w_{\mathrm{NL,total}}$) highlight similar frontal structures around mesoscale eddies and along the coast, $w_{\mathrm{NL,total}}$ is approximately an order of magnitude stronger than both linear components. By cumulatively summing the vertical transport per unit area along

the zonal direction in the study region, $w_{\mathrm{NL,total}}$ contributes to a net downwelling (Fig. 3.4k). Despite having a relatively small contribution at <30-km scales, the linear vertical velocities still exhibit coherent spatial variations. $w_{\mathrm{L,CFB}}$ steadily contributes to a positive (upward) cumulative vertical transport towards the coast. In contrast, $w_{\mathrm{L,TFB}}$ fluctuates around zero and does not make a strong net net contribution to vertical transport (Fig. 3.4k). The shift in dominance from linear to nonlinear Ekman velocities at sub-mesoscale signals a transition to a new dynamical regime in upper-ocean vertical motions.

3.4.4 Decomposition of nonlinear Ekman velocities

Following the decomposition given in Eq. 3.6, $w_{\mathrm{NL},\tau}$ is found to dominate the contribution to $w_{\mathrm{NL,total}}$ and its variability. The terms in Eq. 3.6 are calculated at meso- and sub-mesoscales and seasonally averaged from March to May (Fig. 3.5d–i); the seasonal mean is also shown without filtering for comparison (Fig. 3.5a-c). Synoptic scale ($>$ 200 km) variability can be visually assessed by subtracting the meso- and sub-mesoscale vertical velocities (Fig. 3.5d–i) from those at the unfiltered scales (Fig. 3.5a–c). For $w_{\mathrm{NL},\tau}$, synoptic scale variations are overwhelmed by the meso- and sub-mesoscale variations. Indeed, mesoscale (Fig. 3.5d) and sub-mesoscale (Fig. 3.5g) contributions explain 35.7% and 86.7% of the variance, respectively, for the unfiltered $w_{\mathrm{NL},\tau}$. Correlations between $\boldsymbol{\tau}$ anomalies and large ocean surface vorticity gradients are central to setting the magnitude and pattern of $w_{\mathrm{NL},\tau}$. In fact, sub-30 km filtered $w_{\mathrm{NL},\tau}$ (Fig. 3.5g) is the leading-order contributor to the total nonlinear Ekman pumping (Fig. 3.4f) and dominate over all other $w_{\mathrm{NL},\tau}$, $w_{\mathrm{NL,CFB}}$, and $w_{\mathrm{NL,TFB}}$ terms across all scales. CFB and TFB associated nonlinear Ekman velocities are at least an order of magnitude smaller than $w_{\mathrm{NL},\tau}$ terms. The sub-mesoscale signals for $w_{\mathrm{NL,CFB}}$ (Fig. 3.5h) account for 78.2% of the variance in the full $w_{\mathrm{NL,CFB}}$ (Fig. 3.5b), while the mesoscale contribution for the CFB term is small. In contrast, $w_{\mathrm{NL,TFB}}$ is negligible at all scales and fails to imprint SST-related structure on nonlinear Ekman velocities. In Sec. 3.5.3, it is shown that the dominance of sub-mesoscale $w_{\mathrm{NL},\tau}$ underscores the critical role of fine-scale ocean vorticity in shaping nonlinear Ekman vertical velocities. When focusing specifically on wind–front-induced components, $w_{\mathrm{NL,CFB}}$ and $w_{\mathrm{NL,TFB}}$, the decomposition indicates that at sub-mesoscale CFB dominates, while the TFB-induced contribution is effectively negligible. Potential caveats regarding this decomposition are discussed in Sec. 3.5.3.

The spatial distribution of the decomposed nonlinear components helps explain the observed coastal downwelling pattern in $w_{\mathrm{NL,total}}$ (Fig. 3.4). Cumulative vertical transport per unit area (Fig. 3.5j,k) at both 30–200 km and <30 km scales show that $w_{\mathrm{NL,TFB}}$ fluctuates around zero with no trend as a function of longitude, indicating that TFB makes a negligible net contribution to the vertical transport. In contrast, the downwelling attributed to $w_{\mathrm{NL,CFB}}$ increases in magnitude toward the coast, resulting in a net downward vertical transport that is at least an order of magnitude stronger than that from $w_{\mathrm{NL,TFB}}$ during MMA. $w_{\mathrm{NL},\tau}$ has the largest absolute magnitudes at both meso- and submesoscales, and the strength of this verti-

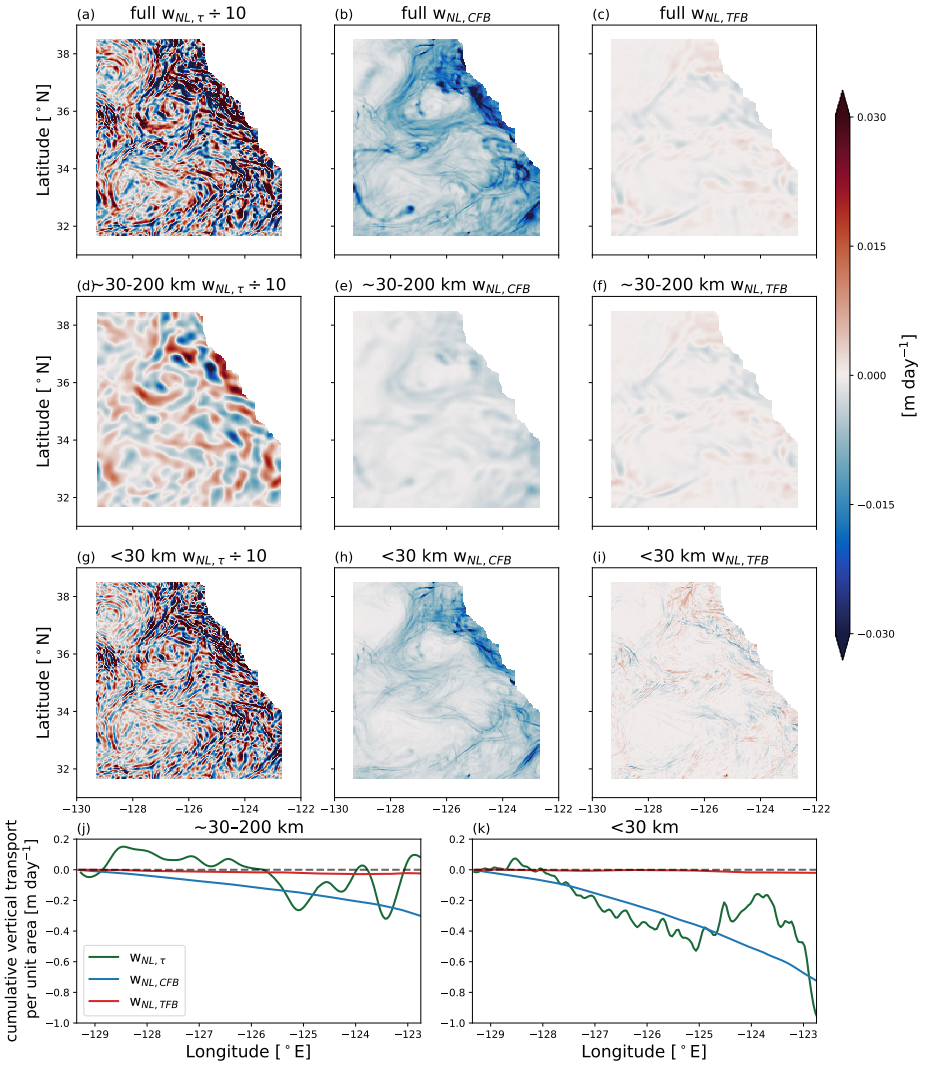

Figure 3.5: March, April, and May averaged nonlinear Ekman vertical velocity decomposition in the California Current System. The $w_{\mathrm{NL,total}}$ is decomposed into three components: the wind stress driven $w_{\mathrm{NL},\tau}$, the current feedback induced $w_{\mathrm{NL,CFB}}$, and the thermal feedback induced $w_{\mathrm{NL,TFB}}$ (Eq. 3.6). The seasonal mean of these components are shown, respectively, at unfiltered full scale in (a)-(c), mesoscale (~30-200 km) in (d)-(f) , and sub-mesoscale (< 30 km) in (g)-(i). Note that in (a), the unfiltered full scale $w_{\mathrm{NL},\tau}$ is an order of magnitude larger than all other fields. Cumulative vertical transport per unit area as a function of longitude of (j) meso- and (k) sub-mesoscale $w_{\mathrm{NL},\tau}$ components, with $w_{\mathrm{NL},\tau}$ in green, $w_{\mathrm{NL,CFB}}$ in blue, and $w_{\mathrm{NL,TFB}}$ in red. Note that the magnitude of $w_{\mathrm{NL},\tau}$ have been reduced by a factor of 10 to use the same colorbar range as the other nonlinear components, but in the cumulative transport calculation $w_{\mathrm{NL},\tau}$ is not re-scaled.

cal velocity intensifies near the coast (Fig. 3.5d,g). However, strong compensating variations between upwelling and downwelling in $w_{\mathrm{NL},\tau}$ lead to relatively weaker contribution in vertical transport. In MMA over the CCS region, $w_{\mathrm{NL},\tau}$ provides a small net vertical transport at the mesoscale and contributes a negative cumulative vertical transport of similar magnitude to $w_{\mathrm{NL,CFB}}$ at the sub-mesoscale.

3.4.5 Comparison with full vertical velocities

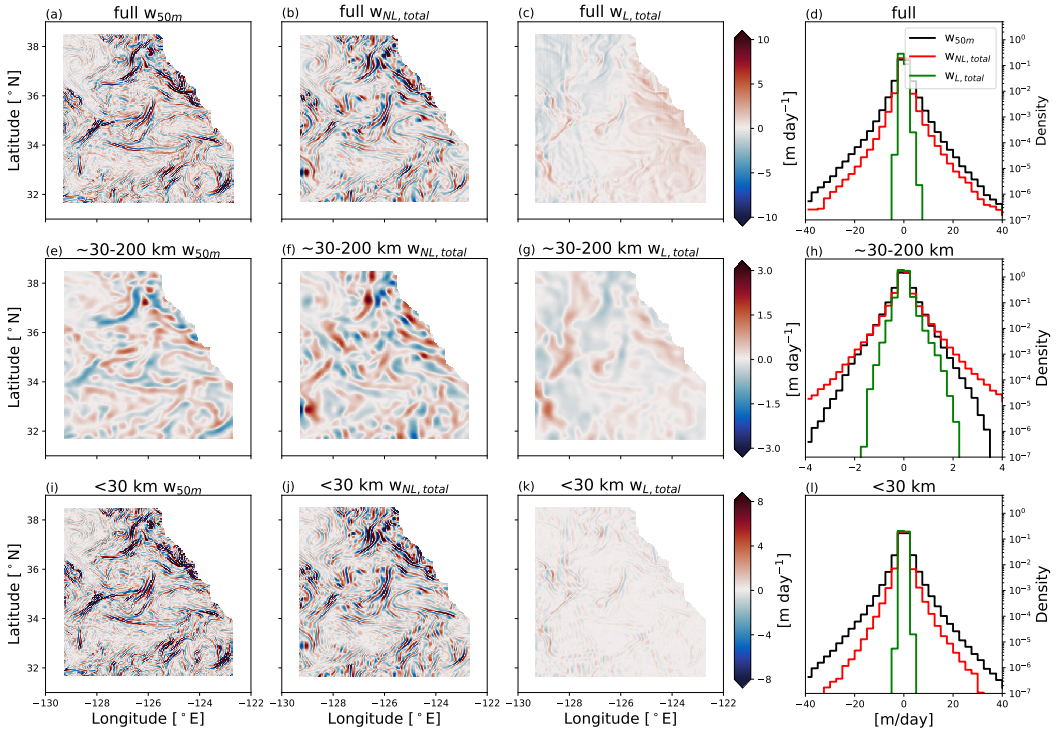

Figure 3.6: Comparisons of total Ekman vertical velocities $w_{\mathrm{NL,Total}}$ and $w_{\mathrm{L,Total}}$ with the vertical velocity at 50 m depth w_{50m}. Snapshots are taken at 4:00 on Mar 29th, 2012, when w_{50m} is not dominated by waves. (a)-(c) w_{50m}, $w_{\mathrm{NL,Total}}$, and $w_{\mathrm{L,Total}}$ without a spatial filter. The same quantities are shown with a spatial filter at (e-g) $\sim$ 30-200 km and at (i-k) <30 km scales. Histograms of (d) unfiltered scale, (h) $\sim$ 30-200 km, and (l) <30 km of the three velocities for all March, April, and May.

Vertical motions may arise from processes beyond Ekman dynamics; here we compare the nonlinear and linear Ekman components with the total simulated vertical velocities. Even though Ekman velocities represent an average of vertical motions induced by Ekman dynamics within the surface Ekman layer, for simplicity we compare $w_{\mathrm{NL,Total}}$ and $w_{\mathrm{L,Total}}$ with simulated vertical velocities at ~50 m, which is approximately at the bottom of the surface Ekman layer in CCS (Chereskin, 1995). To remove internal wave signals in the simulated vertical velocity field, the filter proposed in Torres et al. (2022a), which removes a linear trend between the surface and 80 m depth below the surface mixed layer, is applied. Subsequently, a one-day running mean is further applied to the vertical velocity fields to remove high-frequency noise; spatial filters of $\sim$ 30-200 km and <30 km scales are also used as de-

scribed in Sec. 3.3.2. The simulated vertical velocities, processed in this manner, are referred to as w_{50m}.

The magnitude and spatial structure of w_{50m} is better captured by $w_{NL,Total}$ than by $w_{L,Total}$, with the Total Variation (TV) distance to w_{50m} at unfiltered scales reduced by a factor of 7.3. The TV distance measures a statistical distance between two probability distributions. At mesoscale (~30-200 km), both snapshots and a seasonal histogram (Fig. 3.6e–h) suggest consistent findings with previous mesoscale studies that $w_{NL,Total}$ is of similar importance as $w_{L,Total}$. Both of the Ekman velocities reproduce the large-scale structures seen in w_{50m}. However, at sub-mesoscale, $w_{L,total}$ under-represents the spatial variability in w_{50m} (Fig. 3.6i–k) in snapshots, and underestimates the magnitude of w_{50m} in the seasonal histogram (Fig. 3.6l). Instead, $w_{NL,Total}$ especially with the contributions from $w_{NL,\tau}$ (Fig. 3.5), are able to generate eddy and filamentary structures across the domain in w_{50m} with comparable magnitudes (Fig. 3.6i–k). However, the structures in $w_{NL,Total}$ are offset from those in w_{50m}. This displacement suggests that additional dynamics, such as divergence and secondary circulations, influence the vertical velocities in the upper ocean. Nevertheless, these fine-scale structures mostly stem from surface ocean vorticity and their horizontal gradients. The dominance of sub-mesoscale $w_{NL,Total}$ highlights the importance of ocean surface vorticity and its coupling with surface wind fields; it also suggests a need to resolve small-scale features to improve estimates of total vertical motions in the water column.

3.5 Discussion

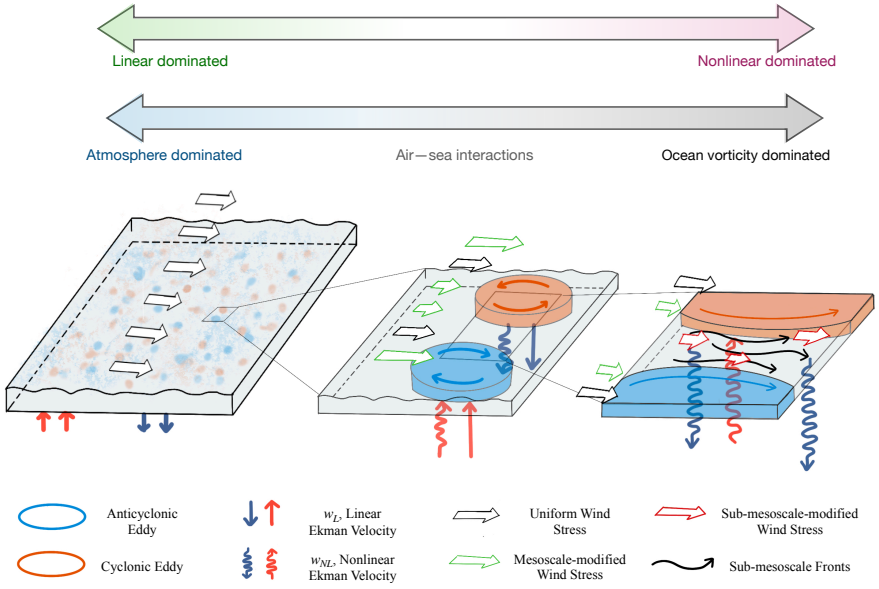

Figure 3.7: Schematic summarizing the scale-dependent shift in Ekman vertical velocity and the dominant drivers. As the horizontal scale decreases from synoptic scales $O(1000)$ km to oceanic mesoscale $O(100)$ km and sub-mesoscale $O(10)$ km, the primary control on Ekman vertical velocities transitions from large-scale atmospheric wind stress to oceanic surface vorticity. Concurrently, nonlinear Ekman velocities become increasingly important at $O(10)$ km scales.

3.5.1 A regime shift in Ekman vertical velocities with spatial scale

This study demonstrates that Ekman vertical velocities gradually transition from atmospheric to oceanic dominance as the spatial scale decreases from $O(1000)$ km to $O(100)$ km, and eventually to $O(10)$ km. Classical Ekman velocity theory (Ekman, 1905) emphasizes the role of atmospheric forcing, where synoptic-scale wind stress curl drives large-scale upwelling and downwelling, shaping vertical velocity patterns across subtropical and subpolar gyres and around the Antarctic Circumpolar Current. This traditional view has been revised by mesoscale studies (e.g., Seo et al., 2016; Gaube et al., 2015), which highlight the increasing importance of air–sea interactions, specifically, the coupling between surface ocean features and atmospheric wind stress, in generating eddy-scale Ekman vertical velocities. At sub-mesoscale ($O(10)$ km), the balance shifts toward oceanic control. Nonlinear Ekman vertical velocities driven by gradients in ocean surface vorticity become the dominant contribution, surpassing those associated with air–sea feedbacks. This indicates that sub-mesoscale Ekman vertical velocity is primarily governed by surface ocean dynamics, marking a transition from joint ocean–atmosphere control at the $O(100)$ km to ocean-dominated Ekman velocities at $O(10)$ km.

3.5.2 Cancellation between linear and nonlinear air–sea Ekman pumping components

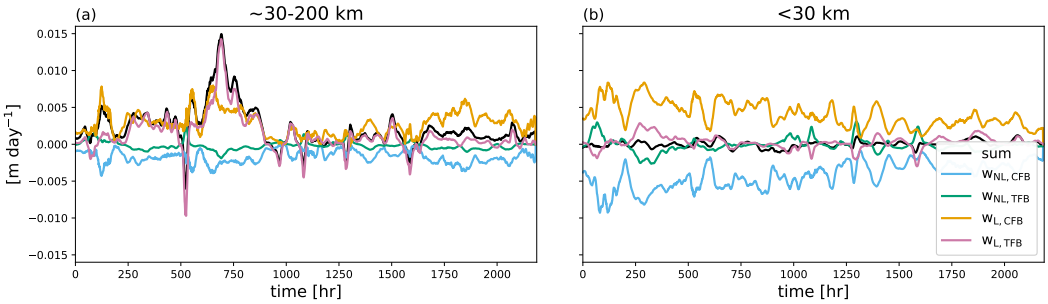

Figure 3.8: March, April, and May time series of domain-averaged Ekman pumping components in the California Current System. (a) Domain-averaged $w_{\mathrm{NL,CFB}}$ (blue), $w_{\mathrm{NL,TFB}}$ (green), $w_{\mathrm{L,CFB}}$ (yellow), $w_{\mathrm{L,TFB}}$ (pink), and their sum (black) at ~30-200 km. (b) As in (a), but for < 30 km scale.

Most of this study has focused on small-scale vertical velocity structures, but total net transport depends on temporally and spatially averaged properties that account for potential cancellation between upwelling and downwelling motions. Here, we focus on vertical volume transport (or mean values of w) from air–sea interaction related components, w_{CFB} and w_{TFB}; vertical tracer fluxes are not considered here and may have more complicated structure due to correlations between w and tracer concentrations.

Time series of spatially averaged Ekman velocities associated with wind–front interactions at 30–200 km and <30 km scales during March-May across the CCS domain highlight two key features: a consistent upwelling contribution from $w_{\mathrm{L,TFB}}$, and a near-complete cancel-

lation of submesoscale components. At 30–200 km scales (Fig. 3.8a), $w_{\mathrm{L,TFB}}$ remains persistently positive (upwelling) and dominates the temporal variability of the total wind–front-induced signal, defined as the sum of $w_{\mathrm{L,CFB}}$, $w_{\mathrm{L,TFB}}$, $w_{\mathrm{NL,CFB}}$, and $w_{\mathrm{NL,TFB}}$. In contrast, at sub-30 km scales, the strongest individual contributions arise from CFB-induced linear and nonlinear components, while SST-driven terms remain comparatively weak. However, the linear and nonlinear components of both CFB and TFB nearly cancel at sub-mesoscale, resulting in average total wind–front-induced vertical velocities that fluctuate around zero. These results indicate that in the CCS region, the net effect of wind–front interactions on vertical transport is primarily governed by mesoscale TFB, with sub-mesoscale contributions playing a minimal role in the spatially integrated sense due to compensation of linear and nonlinear components.

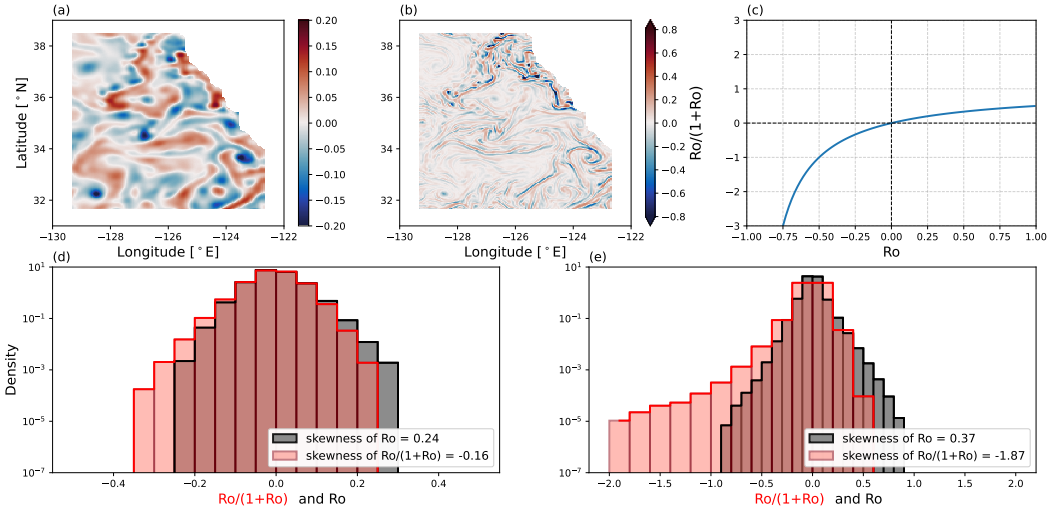

Figure 3.9: The scale factor $\gamma \equiv \frac{Ro}{(1+Ro)}$ that determines the degree of cancellation between linear and nonlinear Ekman velocities (Sec. 3.5b). (a) Snapshot of γ at mesoscale (~30-200 km) taken at 8:00 am on April 8th, 2012. This time is the same as the snapshots in Fig. 3.1. (b) As in (a), but for sub-mesoscale of $<$ 30 km. The analytical variation of γ based on Ro is in (c). (d) Histogram of mesoscale ocean surface Ro $= \zeta/f$ (black bars) as well as γ (red bars). (e) As in (d), but for sub-mesoscale.

The cancellation between TFB and CFB components (Fig. 3.8) further establishes the leading role of sub-mesoscale $w_{\mathrm{NL},\tau}$ in dominating the Ekman vertical velocities, and motivates further investigation into the underlying mechanism of the cancellation and whether it can be generalized to other ocean regions. By taking the ratio of nonlinear to linear components under the assumption that they are both induced by air–sea interactions, a scaling emerges:

$$\gamma \equiv \frac{w_{\mathrm{NL,CFB}}}{w_{\mathrm{L,CFB}}} = \frac{w_{\mathrm{NL,TFB}}}{w_{\mathrm{L,TFB}}} = \frac{\mathrm{Ro}}{(1+\mathrm{Ro})}, \tag{3.7}$$

where Ro $= \zeta f^{-1}$. The degree of compensation or enhancement between w_{L} and w_{NL}, spatially averaged, is largely controlled by the sign and magnitude of γ. If γ is positive, w_{L} and w_{NL} are of the same sign and reinforce the induced vertical velocities. If γ is nega-

tive, w_{L} and w_{NL} are of opposite signs and provide some degree of compensation, which is determined by the relative magnitude of γ.

Spatial maps of γ at meso- and sub-mesoscale (Fig. 3.9) closely resemble maps of ocean surface vorticity (Fig. 3.1), yet γ has a greater tendency to be negatively skewed, especially at sub-mesoscale. At mesoscale, Ro values vary between $\pm O(0.1)$, with a slight positive skewness of 0.24, consistent with typical geostrophic conditions. This distribution yields γ values between -0.5 and 0.5, with mild negative skewness. As a result, for both CFB- and TFB-induced Ekman velocities, the nonlinear components are at most half the magnitude of the corresponding linear terms. Domain-averaged time series of mesoscale γ (not shown) remain mostly negative throughout March to May in the CCS, further confirming that nonlinear velocities generally oppose and reduce the linear contribution, with a residual of the same sign as the linear velocities (Fig. 3.8). In contrast, at sub-mesoscale, Ro values reach $\pm O(1)$, and although the skewness of Ro (0.37) is similar to that at mesoscale, the larger magnitudes lead to a γ distribution with pronounced negative skewness (–1.87). This indicates that at sub-mesoscale, nonlinear Ekman velocities frequently oppose the linear ones with a comparable magnitude, resulting in near-complete compensation (Fig. 3.8).

This behavior can be generalized to other regions of the ocean through Ro-based criteria for relationships between wind–front associated Ekman pumping velocities. In cyclonic regions ($Ro > 0$), linear and nonlinear components reinforce one another, as they share the same sign; however, nonlinear velocities remain weaker since γ asymptotically approaches 1, limiting w_{NL} to at most the magnitude of w_{L}. In weak anticyclones ($-0.5 < Ro < 0$), nonlinear velocities oppose the linear component but remain smaller in magnitude, resulting in partial cancellation with a net residual matching the sign of the linear term. For $-1 < Ro < -0.5$, nonlinear velocities exceed the linear component and dominate the net vertical velocity. When $Ro < -1$, nonlinear and linear components again align in sign, but nonlinear velocities dominate in magnitude. However, under real ocean conditions, with semi-geostrophic fronts and symmetric instability, there is a natural propensity to favor strong cyclones instead of anti-cyclones. As a result, cases where $Ro < -1$ and nonlinear Ekman velocities dominate are expected to be rare. Note that the cancellation argument between linear and nonlinear Ekman velocities only apply to those related to CFB and TFB; $w_{\mathrm{NL},\tau}$ does not participate in the cancellation process.

3.5.3 Caveats and constraints

There are some caveats associated with the decomposition described in Sec. 3.3.5. First, the proposed decomposition of $w_{\mathrm{NL,total}}$ may underestimate $w_{\mathrm{NL,CFB}}$ and $w_{\mathrm{NL,TFB}}$, while overestimating $w_{\mathrm{NL},\tau}$. Underestimation of CFB and TFB may occur because their estimation relies solely on the correlation between surface ocean properties and wind stress curl, while $w_{\mathrm{NL},\tau}$ depends on the surface wind stress $\boldsymbol{\tau}$. At sub-30 km scales, $\boldsymbol{\tau}$ contains variations induced by CFB and TFB (Fig.3.1j–l), but the decomposition in Eq.3.6 does not explicitly partition

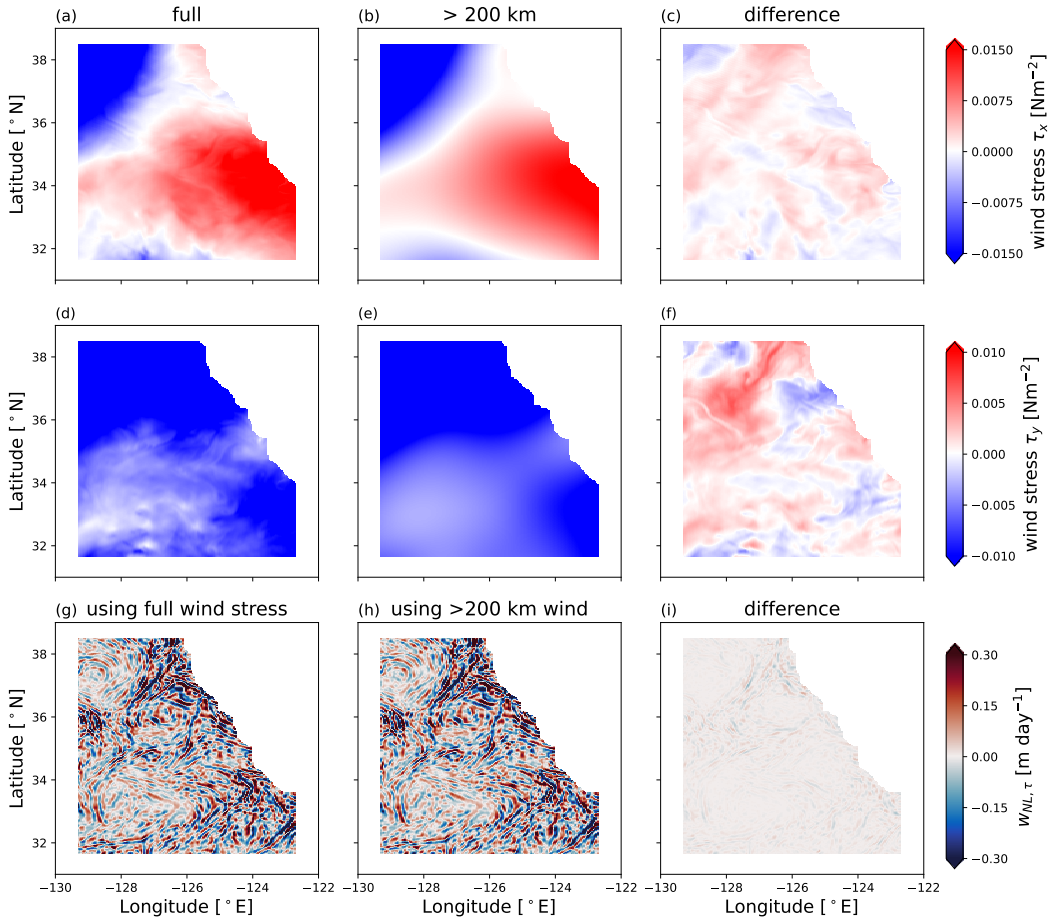

Figure 3.10: Recalculation of $w_{\mathrm{NL},\tau\ \mathrm{large}}$ and comparison with $w_{\mathrm{NL},\tau}$ at sub-30 km. (a,d) Exemplary snapshots of surface wind stress with impacts from meso- and sub-mesoscale wind–front coupling. (b,e) Same as (a,d) but without wind–front coupling impacts. (c,f) The difference between (a,d) and (b,e). Snapshots are from 12:00 on March 1st, 2012. (g) March, April, May seasonally averaged $w_{\mathrm{NL},\tau}$ at sub-30 km, including coupling between vorticity and air–sea generated small-scale wind stress (identical to Fig. 3.5g). (h) Seasonally averaged $w_{\mathrm{NL},\tau\ \mathrm{large}}$ at sub-30 km, isolating impacts from only small-scale ocean surface vorticity gradients. (i) The difference between $w_{\mathrm{NL},\tau}$ and $w_{\mathrm{NL},\tau\ \mathrm{large}}$.

these into feedback contributions. As a result, these "indirect" influences are omitted from $w_{\mathrm{NL,CFB}}$ and $w_{\mathrm{NL,TFB}}$, and are instead absorbed into $w_{\mathrm{NL},\tau}$, likely leading to an overestimation of the role of ocean surface vorticity gradients and coupling with surface wind stress. Furthermore, it remains unclear from the above decomposition (Fig. 3.5) whether the dominance of sub-30 km $w_{\mathrm{NL},\tau}$ is primarily due to the coupling of surface vorticity with surface wind stress or solely the strong vorticity gradients at sub-mesoscale. To assess the extent of this overestimation and identify the primary contributor, sub-30 km $w_{\mathrm{NL},\tau}$ is recalculated and compared with results in Fig. 3.5, in which the product of the unfiltered wind stress and ocean surface vorticity is first computed and then spatially filtered. The recalculation follows the same procedure, but with the key difference that the wind stress fields are first filtered to retain only scales larger than 200 km prior to forming the product. This approach thereby

effectively removes local impacts from mesoscale and sub-mesoscale wind–front interaction on τ (Fig. 3.10a–f), therefore isolating the influence from surface small-scale vorticity gradients. The resulting seasonally-mean $w_{\mathrm{NL},\tau\ \mathrm{large}}$ (Fig. 3.10h) differs point-to-point from the $w_{\mathrm{NL},\tau}$ (Fig. 3.10g or Fig. 3.5g), which include vorticity coupling with small-scale surface wind stress at sub-30 km scales, by less than 35%, indicating that the influence of air–sea interactions on $w_{\mathrm{NL},\tau}$ is limited. Therefore, despite this potential limitation, the decomposition robustly highlights the dominant role of sub-30 km ocean surface vorticity gradients over wind–front interactions in shaping nonlinear Ekman vertical velocities.

Additionally, both the linear and nonlinear Ekman velocity decompositions consider only the contributions from wind–front interactions. This is because both rely on the reconstruction of wind stress curl (Eq. 3.3) from surface SST gradients and surface vorticity. Other dynamical processes that influence wind stress curl variability, such as high-frequency transients or dynamics not related to SST and vorticity, are not considered. These omitted processes likely explain the portion of wind stress curl variance not captured by TFB and CFB (Fig. 3.2). This exclusion may contribute to discrepancies observed between $w_{\mathrm{NL,total}}$ and $w_{\mathrm{L,total}}$ compared to $w_{50\mathrm{m}}$ from the simulation (Fig. 3.6). Nevertheless, even in the absence of additional dynamics, $w_{\mathrm{NL,total}}$ and $w_{\mathrm{L,total}}$, derived under the reconstruction assumption (Eq. 3.3) and incorporating wind stress–vorticity coupling, still succeed in capturing the leading-order magnitude and spatial structure of $w_{50\mathrm{m}}$.

Lastly, our definition of meso- and sub-mesoscale is phenomenological rather than dynamical. A common dynamical criterion for scale separation involves Ro, with mesoscale motions characterized by $\mathrm{Ro} << 1$, and sub-mesoscale motions by $\mathrm{Ro} \gtrsim 1$. Here, our approach is based on a spatial cut-off at 30 km and 200 km for sub-mesoscales and mesoscales, respectively. Under this spatial filtering, some features may not satisfy the dynamical definition of submesoscale, e.g., they may have small Rossby number, yet are still captured due to their small spatial extent. The spatial cut-offs used in the study is consistent with previous meso- and sub-mesoscale studies.

3.6 Conclusion

Our analysis of vertical Ekman velocities associated with air–sea interactions across different spatial scales reveals a progression of distinct dynamical regimes (Fig. 3.7). Using output from a high-resolution coupled numerical simulation in the California Current System, we apply spatial filtering to isolate mesoscale (30–200 km) and sub mesoscale (<30 km) variability (Fig. 3.1), allowing us to quantify and compare the structure and magnitude of linear and nonlinear Ekman velocities arising from wind–front coupling. We find that, in contrast to synoptic scales (O(1000) km), where Ekman velocities are dominated by the linear component, and oceanic mesoscale (O(100) km), where linear and nonlinear components are roughly comparable (Fig. 3.4), Ekman velocities at sub-30 km scales are almost entirely nonlinear-dominated (Fig. 3.5), and the nonlinear Ekman components match closely with

the simulated total near-surface vertical velocity (Fig. 3.6).

To further understand the spatial variability and drivers of these transitions in Ekman vertical velocity regimes, we introduce a decomposition of the nonlinear Ekman velocity into components attributable to ocean surface vorticity, Current Feedback (CFB), and Thermal Feedback (TFB) (see Eq. 3.6); this parallels the decomposition of linear Ekman velocities into CFB and TFB contributions previously examined at mesoscales (Gaube et al., 2015; Seo et al., 2016). This partitioning allows us to attribute the sources of Ekman vertical velocity across scales. We find that alongside the regime shift in linear-to-nonlinear dominance, there is a corresponding shift in the primary driver of Ekman velocities. At the mesoscale (O(100) km), CFB and TFB play a substantial role, and their corresponding linear Ekman velocities have comparable magnitude (Fig. 3.4). However, at sub-mesoscales (O(10) km), despite enhanced CFB and TFB joint control on surface wind stress curl (Fig. 3.2, 3.3), the dominant driver of large nonlinear Ekman velocities is the horizontal gradients of ocean surface vorticity, which is intensified at these scales (Fig. 3.5, 3.10).

It should be noted, however, that the above analyses only account for components related to wind–front interactions and surface vorticity gradients. Contributions from other dynamical processes such as atmospheric synoptic scale systems and topographic impacts not associated with SST or vorticity are not considered. While the decomposition of nonlinear Ekman velocities may not be entirely complete (Sec. 3.5.3), the dominant role of ocean surface vorticity remains robust. These results underscore the importance of explicitly resolving submesoscale air–sea interactions, particularly surface ocean coherent structures, to accurately capture upper ocean vertical velocity and transport. This is critical due to the increasing significance and dominance of nonlinear Ekman velocities at fine spatial scales.

Data Availability Statement

The coupled ocean-atmosphere simulation used in this study is accessible through: (a) any NASA Ames Supercomputer at ~ dmenemen/c1440_llc2160; (b) xmitgcm: `https://xmitgcm.readthedocs.io`; (c) NASA Ames data portal: `https://data.nas.nasa.gov/ecco/`.

Acknowledgments

The authors gratefully acknowledge insightful discussions with Lionel Renault, Mara Freilich, Jacob Wenegrat, Igor Uchoa, and Fabien Desbiolles, which helped strengthen the manuscript. YB acknowledges support from the National Aeronautics and Space Administration Science Mission Directorate FINESST program under Award
No. 80NSSC21K1635. ABVB was supported by the NSF award OCE-2241822, and NASA awards 80NSSC23K0979 through the Ocean Vector Winds Science Team and the Earth System Explorer program ODYSEA 80GSFC24CA067.

3.7 Appendix A: Ekman and ageostrophic Rossby number

Following Stern (1965), we define a lower bound for the Ekman Rossby number as the linear Ekman Rossby number, Ro_L, estimated using the linear Ekman transport velocity $v_{E,L}$:

$$\int_{-H}^{0} v_{E,L} dz = -\frac{1}{\rho_0 f} \hat{k} \times \tau. \tag{3.8}$$

To account for nonlinear effects, we also estimate a nonlinear Ekman Rossby number, Ro_{NL}, corresponding to an Ekman transport velocity $v_{E,NL}$ that includes the influence of surface vorticity:

$$\int_{-H}^{0} v_{E,NL} dz = -\frac{1}{\rho_0 (f+\zeta)} \hat{k} \times \tau, \tag{3.9}$$

where ζ is the surface relative vorticity. This formulation modifies the classical expression in Eq. 3.8 by replacing f with $f+\zeta$ in the denominator. Both Ro_L and Ro_{NL} are calculated using a constant Ekman depth of $H = 48$ m, consistent with Chereskin (1995).

To provide an upper bound, we introduce the ageostrophic Rossby number Ro_{AG}, derived from surface ageostrophic velocities which are defined as the difference between simulated surface velocities and geostrophic velocities inferred from SSH gradients. These velocities take into account of other ageostrophic dynamics in additional to the Ekman balance.

The applicability of Eq.3.1 depends on the Ekman Rossby number being much smaller than one. Based on the estimates above, both Ro_L and Ro_{NL} are approximately $O(0.01)$, and the upper bound Ro_{AG} remains within $O(0.1)$ (Fig.3.11), indicating that the use of Eq.3.1 is justified under the resolution of this coupled numerical simulation.

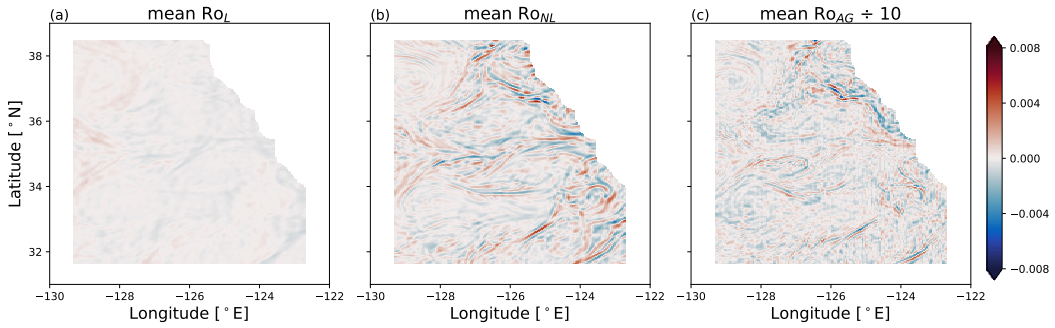

Figure 3.11: Examples of April monthly-averaged Ekman and ageostrophic Rossby number estimations. (a) Ro_L, (b) Ro_{NL}, and (c) Ro_{AG}. Note that the magnitude of Ro_{AG} (factor of 10) have been reduced to use the same color bar range as the linear and nonlinear Ekman Rossby numbers.

3.8 Appendix B: Spatial variability of coupling coefficients α and β

To extract the spatial structure of α and β at meso- and sub-mesoscale, they are calculated per grid point for the three-month time window, and sub-30 km correlation coefficients exhibit a more spatially uniform distribution than the mesoscale ones. For the full wind stress curl, large magnitudes of α tend to cluster near the centers of mesoscale eddies, where velocity

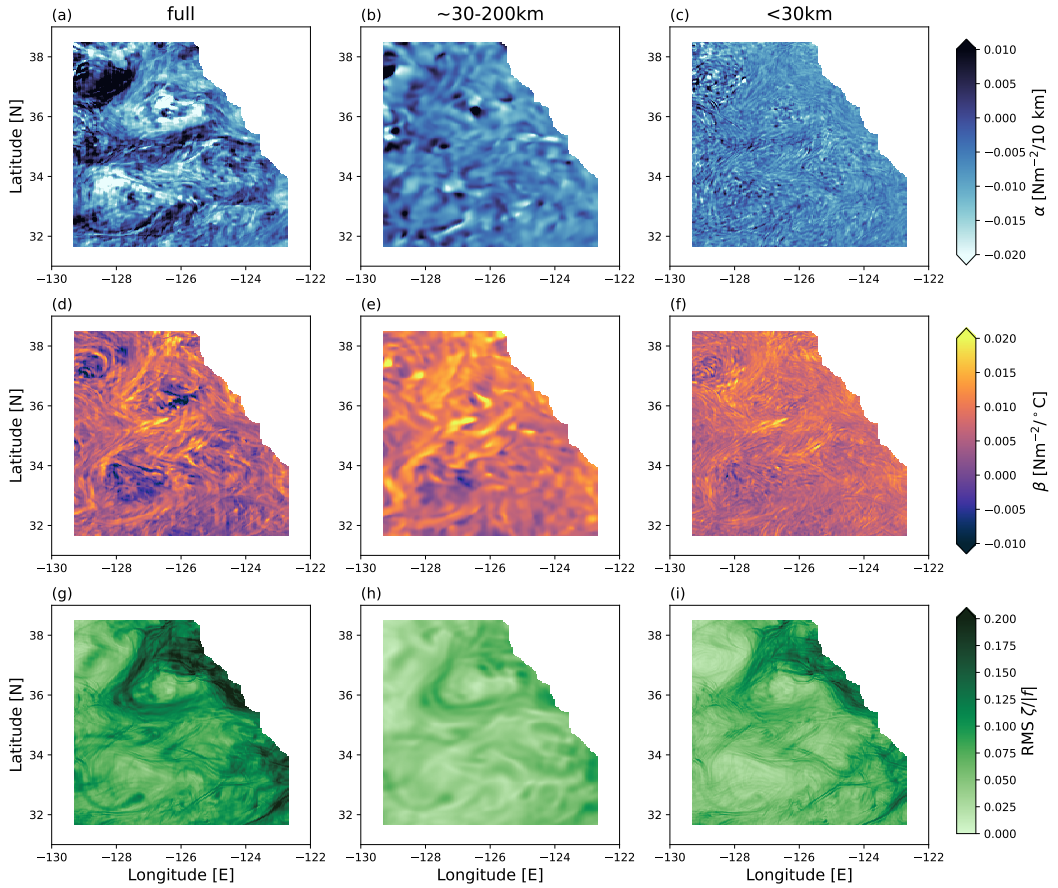

Figure 3.12: Spatial information of the joint correlation coefficients α and β at full, ∼30-200 km, and <30 km spatial scales. (a-c) The CFB coefficient α at the three spatial scales. (d-f) The TFB coefficient β at the three spatial scales. (g-i) The nondimensionalized RMS vorticity, which highlight surface ocean $O(100)$ km eddies and $O(10)$ km fronts and filaments.

gradients are typically strongest. In contrast, β values are enhanced at the edges of mesoscale eddies, where temperature gradients are sharpened by mesoscale straining or frontogenesis. In some regions, α and β have signs opposite to the canonical correlations, potentially reflecting the influence of synoptic-scale atmospheric variability. At 30–200 km and <30 km scales, α and β are no longer elevated at eddy centers. In particular, the sub-30 km α field shows a relatively uniform distribution throughout the domain, consistent with Conejero et al. (2024). In contrast, the tendency for β to intensify at eddy edges and frontal filaments persists across scales. Localized regions of large-magnitude β coincide with regions of elevated root-mean-square (RMS) vorticity, suggesting that sub-30km SST gradients are aligned with strong frontal structures and drive intense TFB.

Chapter 4

LAGRANGIAN TIME SCALES OF SUBMESOSCALE TURBULENCE

4.1 Abstract

Submesoscale turbulence affects a wide range of physical and biogeochemical processes. Previous work has emphasized a dynamical transition from geostrophically balanced motion at large to unbalanced motion at small scales, a transition that has important implications for energy transfers and tracer transport. It remains unclear, however, at what length scale this transition occurs. The time scale of submesoscale motion can indicate the dynamical regime because balanced motion evolves on time scales much longer than Earth's rotation period. It is pointed out here that the time scale of evolution must be diagnosed in the flow-following Lagrangian frame. A numerical simulation and observations consistently indicate that the Lagrangian time scale of submesoscale flow is much longer than that registered by a fixed Eulerian observer, putting the transition to unbalanced dynamics at ∼1 km, much shorter than what has previously been suggested based on Eulerian diagnostics.

4.2 Introduction

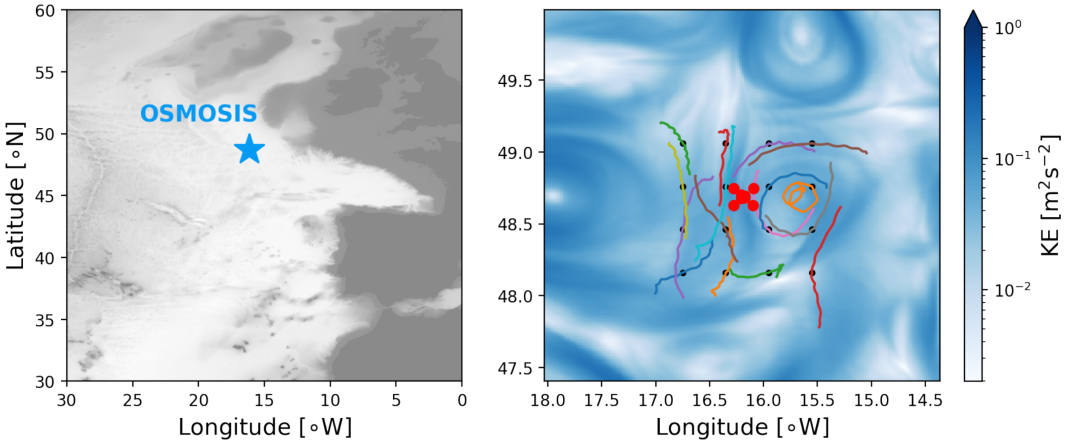

Figure 4.1: OSMOSIS array and particle advections. (left) Location of the OSMOSIS array in the Northeast Atlantic. The shading shows the elevation, which increases with the darkness. (right) Example Lagrangian advection in LLC 4320. Trajectories of 2-day forward and 2-day backward advections are shown on selected grid points. Red dots signify where the OSMOSIS mooring observations are. Shading is the mean surface kinetic energy in the 4-day advection window.

Submesoscale fronts and filaments have been observed in the upper ocean in a wide range of contexts (e.g., McWilliams, 2016; Shcherbina et al., 2013; Callies et al., 2015; Taylor et al., 2018). The submesoscale range here is broadly defined[1] as the scales ranging from ∼100 m to ∼10 km. A frequently emphasized feature of this range of scales is that it hosts the tran-

[1]Here and throughout, we use wavelengths to describe spatial scales and periods to describe time scales.

sition from geostrophically balanced to unbalanced dynamics, corresponding to the Rossby number $\mathrm{Ro} = U/fL$, where U is a velocity scale, L a length scale, and f the Coriolis frequency, transitioning from $\mathrm{Ro} \ll 1$ to $\mathrm{Ro} \gtrsim 1$. When the Ro begins to exceed one, which occurs when the length scale of the motion becomes sufficiently small, the flow can then at least partially escape the constraints imposed by Earth's rotation (e.g., Thomas et al., 2008; McWilliams, 2016; Taylor and Thompson, 2023). This transition to unbalanced dynamics is critical as it signifies important changes in the behavior of the flow. Horizontal divergence, negligible at mesoscales, now becomes comparable to the vertical component of vorticity (e.g., D'Asaro et al., 2018; Barkan et al., 2019). Subsequently, vertical velocities start to follow an aspect ratio scaling rather than being multiplied by the additional factor of Ro as in quasi-geostrophic (QG) and semi-geostrophic (SG) theory (Hoskins and Bretherton, 1972; Vallis, 2017), possibly augmented by vertical mixing in the surface boundary layer (e.g., Young, 1994; Gula et al., 2014). Understanding this transition is essential to understanding the physics of the submesoscale range, which is itself critical for understanding ocean climate: in numerical simulations, submesoscale motions dominate the near-surface vertical velocity fields (e.g., Mahadevan and Tandon, 2006; Capet et al., 2008b) and are thought to have a substantial impact on energy, heat, nutrient, and carbon budgets (Mahadevan, 2016; Rosso et al., 2016; Balwada et al., 2018; Su et al., 2018; Fox-Kemper et al., 2021).

Although previous work has emphasized this dynamical transition (e.g., Thomas et al., 2008; McWilliams, 2016), it remains unclear at what length scale the QG and SG assumptions break down and the flow becomes unbalanced. This is an important question because some previous work has used QG and SG theory to interpret observations and numerical simulations (e.g., Thomas et al., 2008; Callies et al., 2016) at small scales, whereas other studies have appealed to unbalanced dynamics (e.g., Barkan et al., 2019). The Rossby number that characterizes this dynamical transition can be written as the ratio between the time scale of Earth's rotation and the advective timescale $\tau = L/U$: $\mathrm{Ro} = (\tau f)^{-1}$. The transition occurs when the timescale τ becomes comparable to f^{-1}. It is important that τ measures the timescale at which the flow evolves following the path of a fluid parcel. It is this Lagrangian timescale that determines whether the flow is balanced or not. We demonstrate here that distinguishing between this Lagrangian timescale and the Eulerian one, registered by a fixed observer, drastically changes the inferred transition scale.

Previous work has not always made this distinction—and, as a result, produced seemingly inconsistent estimates of the transition scale between balanced and unbalanced dynamics. Torres et al. (2018) computed frequency–wavenumber (ω–κ) spectra of kinetic energy from a global submesoscale-permitting numerical simulation (the same as used below). Their decomposition of the kinetic energy into contributions from different temporal and spatial scales indicated that a substantial part of submesoscale turbulence has a timescale comparable to f^{-1}. This transition to super-inertial timescales, interpreted as the transition to unbalanced submesoscale motion, occurred at a length scale as large as $\sim$10 km. This con-

clusion would strongly undermine the applicability of QG and SG theory to submesoscale dynamics.

In stark contrast to this numerical result, Shcherbina et al. (2013) found that the vertical vorticity ζ was of a similar magnitude as f when measured at $\sim$1 km using two ships steaming in parallel south of the Gulf Stream. While $\zeta/f \sim 1$ does not necessarily imply unbalanced dynamics—SG theory produces frontal vorticities in excess of f without violating its assumptions (Hoskins and Bretherton, 1972)—this observation does put an upper bound of $\sim$1 km on the transition scale to unbalanced motion. From these and additional observations from the subtropical West Atlantic, Callies et al. (2015) furthermore calculated a scale-dependent Rossby number based on an advective time scale, which also approached $\sim$1 at a length scale of $\sim$1 km when submesoscale turbulence was vigorous. Similarly, Callies et al. (2020) estimated a scale-dependent Rossby number from the Ocean Surface Mixing, Ocean Sub-mesoscale Interaction Study (OSMOSIS mooring) observations in the Northeast Atlantic (also used below) and found Ro < 1 down to length scales $\sim$1 km. This observational evidence thus appears to imply that QG and SG ideas can be applied down to scales $\sim$1 km.

A potential resolution of this apparent contradiction is that the Eulerian timescales inferred in the ω–κ spectrum of Torres et al. (2018) substantially differ from the Lagrangian time scales characterizing the flow evolution along the paths of fluid parcels (Callies et al., 2020). If submesoscale features are embedded in and advected by a stronger mesoscale flow, a fixed observer may register a rapid change in the flow even if the submesoscale feature itself evolves relatively slowly. The low Lagrangian frequency of the submesoscale flow is Doppler shifted to a much higher Eulerian frequency. The rest of the paper is organized as follows. First, we illustrate the effect of Doppler shifting in a simple example. We then show that Doppler shifting substantially shifts the inferred transition scale between balanced and unbalanced dynamics in a realistic numerical simulation. Finally, we present observational evidence for the importance of Doppler shifting in the real ocean.

4.3 Lagrangian vs. Eulerian frequency spectra: an illustration

The Doppler shifting scenario described above is complicated: meso- and submesoscale flow is turbulent, with energy distributed across a wide range of scales. Submesoscale features are advected, sheared, and strained by a flow much more complicated than a uniform one that would produce a simple Doppler shift. Before facing this complicated reality in simulations and observations, we illustrate the effect in a drastically simplified kinematic example. We advect a simple submesoscale eddy field with a uniform flow and diagnose the differing Eulerian and Lagrangian timescales.

We prescribe a uniform mean flow U and an eddy field translating with U, mimicking the advecting mesoscale motion and the embedded submesoscale turbulence, respectively (Fig. 4.2a). The streamfunction is $\psi = -Uy + \psi_0 \cos\kappa(x - Ut)\cos\kappa y$. For an Eulerian

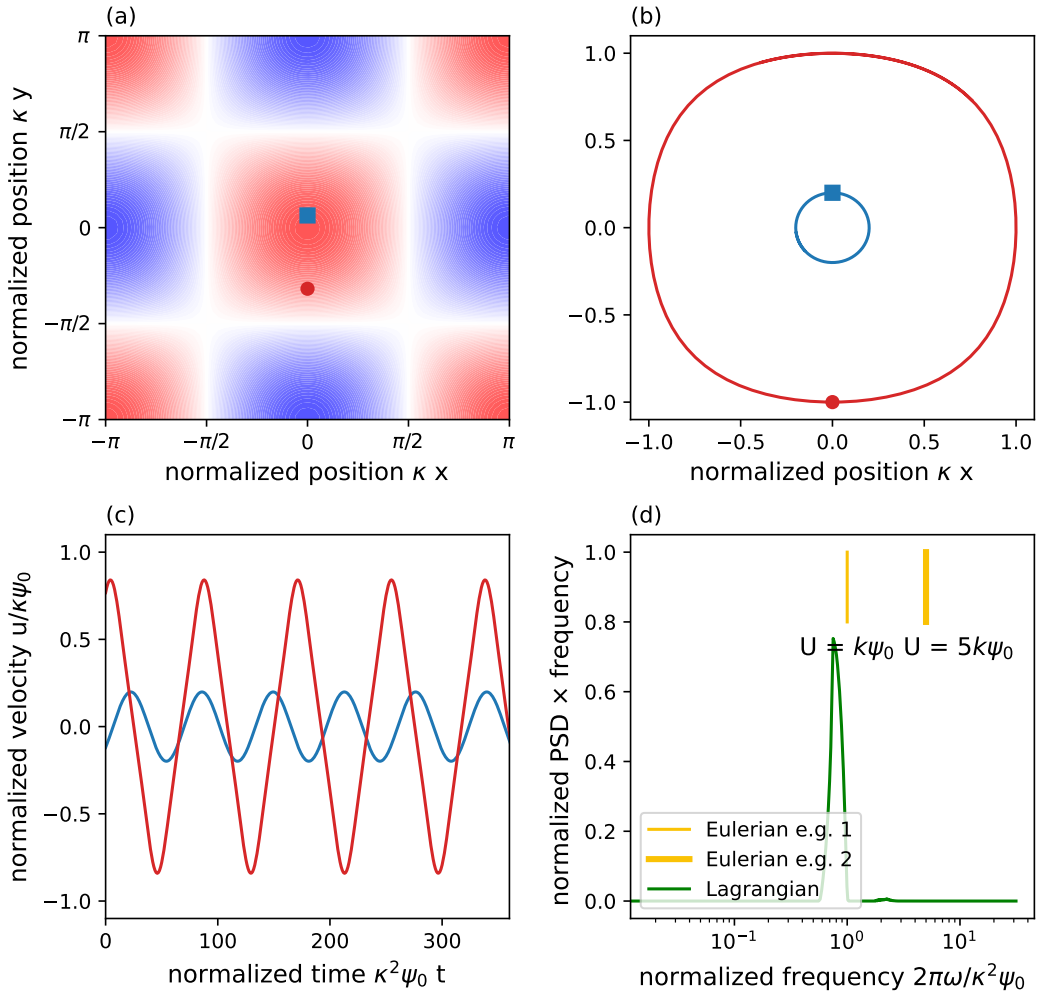

Figure 4.2: A simple model illustration of the impact of Doppler shifting on Eulerian and Lagrangian flow frequencies. (a) Prescribed eddy streamfunction $\psi + Uy$. The two dots represent two example particles in the Lagrangian advection. (b) Two example trajectories of the seeded particles in (a), one close to the origin, the other at the eddy edge. (c) Normalized velocity time series of the two example particles. Particles in the vicinity of the origin circulate faster and have higher frequencies. (d) Normalized frequency spectrum in variance preserving form. The Lagrangian spectrum is immune to changes in the background mean flow U, yet Eulerian spectrum adjusts based on the strength of U.

observer, the velocity signal is periodic with frequency $\omega_{\mathrm{E}} = \kappa U$. To assess the Lagrangian evolution, we release an ensemble of particles into the flow. These particles follow trajectories defined by $\dot{\xi} = -\partial_y \psi$ and $\dot{\eta} = \partial_x \psi$. Transformed into coordinates following the mean flow, $\xi' = \xi - Ut$, $\eta' = \eta$, these equations become

$$\dot{\xi}' = \kappa\psi_0 \cos\kappa\xi' \sin\kappa\eta', \qquad \text{and} \qquad \dot{\eta}' = -\kappa\psi_0 \sin\kappa\xi' \cos\kappa\eta'. \tag{4.1}$$

A Lagrangian observer sees the mean flow U as a constant, zero-frequency component that has no impact on the time-variable velocity recorded along the paths of fluid parcels. The characteristic Lagrangian frequency ω_{L} will be independent of U.

Near the eddy centers, e.g.,, near $(\xi', \eta') = (0, 0)$, (4.1) can be simplified into $\dot{\xi}' = \kappa^2 \psi_0 \eta'$ and $\dot{\eta}' = -\kappa^2 \psi_0 \xi'$. This describes a harmonic oscillator, and the solution is $\xi' = \xi'_0 \cos \omega_L t + \eta'_0 \sin \omega_L t$ and $\eta' = \eta'_0 \cos \omega_L t - \xi'_0 \sin \omega_L t$ with $\omega_L = \kappa^2 \psi_0$, which we emphasize has no dependence on U. Away from the eddy centers, the trajectories of particles will not be circular and take longer than $2\pi/\omega_L$ to complete an orbit (Fig. 4.2b,c). Therefore, a Langrangian frequency spectrum constructed by averaging over an ensemble of particles across the domain has some spread in frequency space (Fig. 4.2d). The peak of this spectrum is slightly below $\omega = \kappa^2 \psi_0$. We calculated this spectrum from 1600 particles released on a uniform grid covering one eddy and numerically advected in the flow-following coordinates ξ' and η' using a 4th order Runge–Kutta scheme (Fig. 4.2b,c).

The ratio between the mean flow U and the submesoscale eddy velocity scale $\kappa \psi_0$ can be freely varied to illustrate the impact of Doppler shifting (Fig. 4.2d). The Eulerian frequency $\omega_E = U\kappa$ scales with U, whereas the Lagrangian frequency $\omega_L = \kappa^2 \psi_0$ is independent of U. Because mesoscale velocities are larger than submesoscale velocities, $U > \kappa \psi_0$, and therefore $\omega_E > \omega_L$. In this regime, an Eulerian observer registers faster flow evolution than a Lagrangian one.

4.4 Energy reshuffling in a numerical simulation

We investigate the space–time variability of submesoscale flows from an Eulerian and Lagrangian perspective in output from a realistic high–resolution simulation (Fig. 4.1). In particular, we calculate Eulerian and Lagrangian ω–κ spectra that reveal the anticipated differences in timescales (i.e., Lagrangian time scales exceed Eulerian ones) at spatial scales of $\sim$10 km.

We use hourly output from a global (1/48)° MITgcm simulation (Su et al., 2018, LLC 4320;) in a region surrounding the site of the OSMOSIS field campaign in the Northeast Atlantic (Fig. 4.1b). This simulation resolves part of the submesoscale range down to $\sim$10 km. The simulated submesoscale energy falls into a reasonable range in the winter (Erickson et al., 2020), when observations indicate it is strongest (Buckingham et al., 2016; Callies et al., 2020; Lawrence and Callies, 2022). It has been noted that the simulation has too much submesoscale energy in spring and summer compared with the OSMOSIS observations (Erickson et al., 2020). The simulation underestimates near-inertial motion due to its use of 6-hourly reanalysis for the wind forcing (Rocha et al., 2016) and overestimates tidal motion (Arbic et al., 2022), but the present study does not focus on these wave motions. These discrepancies with the real ocean do not hinder our qualitative examination of Eulerian and Lagrangian timescales, but they should be kept in mind when interpreting the simulations results more quantitatively.

Eulerian ω–κ spectra are computed following standard practice (cf., e.g., Torres et al., 2018). We define a fixed Eulerian grid $\boldsymbol{x}_0$ of 806 points (a few of which are shown in Fig. 4.1b), on

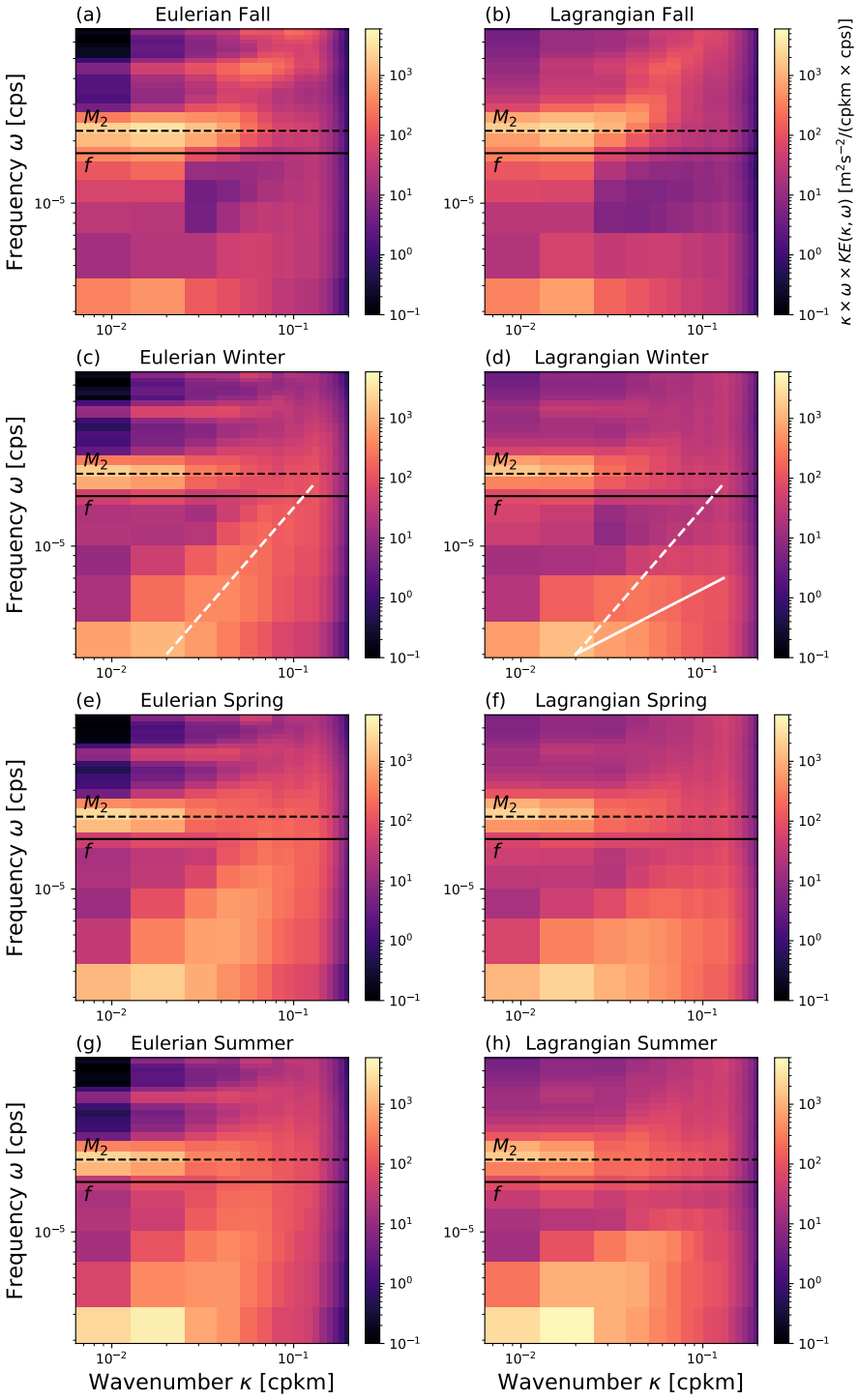

Figure 4.3: Eulerian (left) and Lagrangian (right) frequency–wavenumber (ω–κ) spectra of kinetic energy in LLC 4320 in each season. The spectra are multiplied by κ and ω and therefore variance-preserving. In the winter season, dashed and solid white lines highlight the difference in energy distribution associated with meso- and submesoscale turbulence in the Eulerian and Lagrangian frames, respectively.

which we extract hourly Eulerian velocities over a period of one year. The grid covers 48.31-49.06°N with increments of 0.03° and 15.25-16.75°W with increments of 0.05°. We cut these time series into 4-day chunks. To mitigate spectral aliasing, we apply a Hann window in space and time to each 4-day chunk. We overlap the 4-day chunks by 2 days to reduce the spectral estimation error. We then perform a Fourier transform in space and time for each time chunk,

$$\hat{\boldsymbol{u}}_{\mathrm{E}}(\boldsymbol{\kappa}, \omega) = \int w(\boldsymbol{x}_0, t)\, \boldsymbol{u}(\boldsymbol{x}_0, t)\, e^{-i(\boldsymbol{\kappa}\cdot\boldsymbol{x}_0 - \omega t)}\, \mathrm{d}\boldsymbol{x}_0\, \mathrm{d}t, \tag{4.2}$$

where $w(\boldsymbol{x}_0, t)$ is the Hann window. We average the resulting periodograms $|\hat{\boldsymbol{u}}_{\mathrm{E}}|^2$ over each season, using the same definition of seasons as in Callies et al. (2020), to obtain the seasonal spectra.

Lagrangian ω–κ spectra are constructed similarly but with the time evolution recorded along particle trajectories. Instead of recording the velocities on the fixed $\boldsymbol{x}_0$ grid, we initialize particles on the $\boldsymbol{x}_0$ grid and advect them forward and backward with the evolving velocity field to obtain the trajectories $\boldsymbol{x} = \boldsymbol{x}_0 + \boldsymbol{\xi}(t)$ and the corresponding velocity time series $\boldsymbol{u}(\boldsymbol{x}_0 + \boldsymbol{\xi}, t)$. We use a 4th-order Runge–Kutta scheme and initialize the particles at the midpoints of the same 4-day time chunks used in the Eulerian analysis. We thus obtain Lagrangian velocity time series referenced to the $\boldsymbol{x}_0$ grid, on which we perform the Fourier transform:

$$\hat{\boldsymbol{u}}_{\mathrm{L}}(\boldsymbol{\kappa}, \omega) = \int w(\boldsymbol{x}_0, t)\, \boldsymbol{u}(\boldsymbol{x}_0 + \boldsymbol{\xi}, t)\, e^{-i(\boldsymbol{\kappa}\cdot\boldsymbol{x}_0 - \omega t)}\, \mathrm{d}\boldsymbol{x}_0\, \mathrm{d}t. \tag{4.3}$$

Note that the spatial Fourier transform is performed with respect to the fixed grid $\boldsymbol{x}_0$, so the only difference between (4.2) and (4.3) is the velocity time series being transformed are evaluated at fixed locations or along the paths of fluid parcels. Spectra are estimated using the same averaging as for the Eulerian case.

Caution should be exercised when interpreting the Lagrangian ω–κ spectra. While advected forwards and backwards, the relative positions of the particles change—they do not remain on a fixed grid. The energy assigned to a wavenumber κ based on the reference particle positions $\boldsymbol{x}_0$ therefore does contains information from spatial scales other than $2\pi/\kappa$. We mitigate this smearing in wavenumber space in the Lagrangian ω–κ spectra by picking a relatively short 4-day window. This window length is just long enough to give enough frequency resolution to distinguish between sub- and superinertial motion but short enough to limit the distortion of the particle positions. Our application of a Hann window further limits the impact of the times when the particles are furthest from their reference positions and distortion is largest. Our forward and backward advection, together with these relatively short windows, also limits potential biases in the sampling produced by convergence or divergence (cf. Choi et al., 2017). Integrated over frequencies and wavenumbers, the Eulerian and Lagrangian spectra produce similar kinetic energy levels (e.g., 0.0131 $\mathrm{m^2\,s^{-2}}$ vs. 0.0129 $\mathrm{m^2\,s^{-2}}$ in winter).

A comparison of the distribution of energy in the ω–κ domain reveals a shift of submesoscale energy to lower frequencies when going from the Eulerian to the Lagrangian frame (Fig. 4.3). Consistent with previous work (Torres et al., 2018; Jones et al., 2023), the kinetic energy is enhanced along a straight line in the logarithmic ω–κ space (Fig. 4.3, left column). This population of energy is associated with meso- and submesoscale turbulence and distinct from inertial, tidal, and other inertia–gravity wave motion. This feature is visible in all seasons but more pronounced when the model produces energetic submesoscales (winter, spring, and summer). This population of energy intersects the inertial frequency f at $\sim$10 km (Fig. 4.3, solid black lines), signifying that the Eulerian evolution of submesoscale turbulence becomes superinertial at $\sim$10 km. This length scale is at the same order of magnitude although slightly smaller than in the Kuroshio region and Drake Passage (Torres et al., 2018; Rocha et al., 2016). This is not surprising given that the meso- and submesoscale energy level is consistently lower at the site of the OSMOSIS campaign, so Ro $\sim$ 1 is reached at smaller scales.

In the Lagrangian spectra (Fig. 4.3, right column), the energy associated with meso- and submesoscale turbulence also clusters along straight lines in all seasons, but these lines have smaller slopes than in the Eulerian spectra (Fig. 4.3c-d). This slope change opens up a "gap" between the energy associated with submesoscale turbulence and the inertial frequency. The submesoscale energy that occupies frequencies around f in the Eulerian ω–κ spectra is now shifted—or reshuffled—to lower frequencies in the Lagrangian frame. This is consistent with the illustrative example of Section 4.3, in which submesoscale eddies are advected by swift mesoscale flows and therefore occupy a higher frequency when viewed by an Eulerian observer. Down to the model's effective resolution of $\sim$10 km, the energy associated with submesoscale turbulence remains subinertial when viewed in the Lagrangian frame. If extrapolated to unresolved scales, the line along which energy is concentrated would intersect f at $\sim$1 km—that is, at substantially smaller scales than in the Eulerian spectra. The transition to unbalanced motion occurs at much smaller scales if care is taken to consider the evolution along the path of fluid parcels.

In the next section, we present observational evidence of this energy reshuffling between the Eulerian and Lagrangian frames. The observations do not allow us to compute full ω–κ spectra, but the reshuffling can also be seen if these spectra are collapsed to frequency space. To compare to observations, we calculate Eulerian and Lagrangian frequency spectra at the location of the central OSMOSIS mooring (see Fig. 4.1, Buckingham et al., 2016; Yu et al., 2019) from the model output, using the same 4-day chunks and forward and backward advection to obtain the Lagrangian time series. These spectra exhibit the same energy reshuffling identified in the ω–κ spectra, albeit less clearly (Fig. 4.4a). The reshuffling leads to an increase of energy at slightly subinertial frequencies in Eulerian spectra compared to Lagrangian ones and to a compensating reduction at lower frequencies. The difference (Eulerian minus Lagrangian) of the spectra demonstrates this reshuffling more

clearly (Fig. 4.4i). Integration of the ω–κ spectrum over wavenumbers, however, inevitably obscures the reshuffling somewhat. Especially inertial, tidal, and other inertia–gravity wave motion block our view of the small-scale submesoscale energy in the super-inertial band.

4.5 Evidence from mooring observations

In this section, we substantiate the conclusions drawn from the simulation with observations from the OSMOSIS mooring array. Lacking sufficient actual Lagrangian data (see below), we construct synthetic particle trajectories and Lagrangian velocity time series along those trajectories, using a spatially mapped velocity field estimated from the mooring array. The differences between the resulting Lagrangian frequency spectra and their Eulerian counterparts are similar to those in the simulation, suggesting that Doppler shifting is also at play in the real ocean.

The OSMOSIS mooring array has nine near-surface acoustic current meters, arranged in two squares centered on a central mooring, with the outer square enclosing a $14\,\mathrm{km} \times 14\,\mathrm{km}$ box (Fig. 4.1b; Buckingham et al., 2016, Fig. 1). Although the nominal depths of these top current meters range from 30 m to 60 m, we treat them as if they were at the same depth, ignoring vertical shear that is likely minor at the scales of interest here. The moorings return current measurements from September 2012 to September 2013 averaged to 10-minute intervals. Erickson et al. (2020) and Callies et al. (2020) used structure functions to extract limited spatial information from the array, but the coverage is too sparse for a spatial Fourier analysis. We therefore restrict our spectral analysis to the time domain.

The moorings act as Eulerian observers and yield Eulerian time series of velocity, yet obtaining sufficient Lagrangian observations around moorings is less straightforward. Surface drifters, floating devices that drift with near-surface currents (Elipot et al., 2016; D'Asaro et al., 2018), would have been an ideal source of flow-following velocities. There were only eighteen drifter trajectories in the vicinity of the moorings during the deployment of the OSMOSIS array, unevenly distributed across the seasons. We attempted to use drifter data to calculate the Lagrangian spectra, but with so few drifters the substantial seasonal and interannual variability make it difficult to obtain robust statistics. This necessitates an alternative strategy to generate Lagrangian velocity time series.

To sidestep the difficulty of limited direct Lagrangian measurements, we generate synthetic trajectories from an interpolated mapping of the mooring velocities. We use the mapped velocity fields to advect particles forward and backward for 2 days starting from the central mooring location. We use the central mooring location as the reference because particles are most likely to remain within or close to the confines of the mooring array. The Lagrangian spectra for all four seasons are then estimated from these synthetic Lagrangian data using the same procedure as above. We tested the approach (described in the SI) with the output from the numerical simulation and were able to reconstruct Lagrangian spectra in the subin-

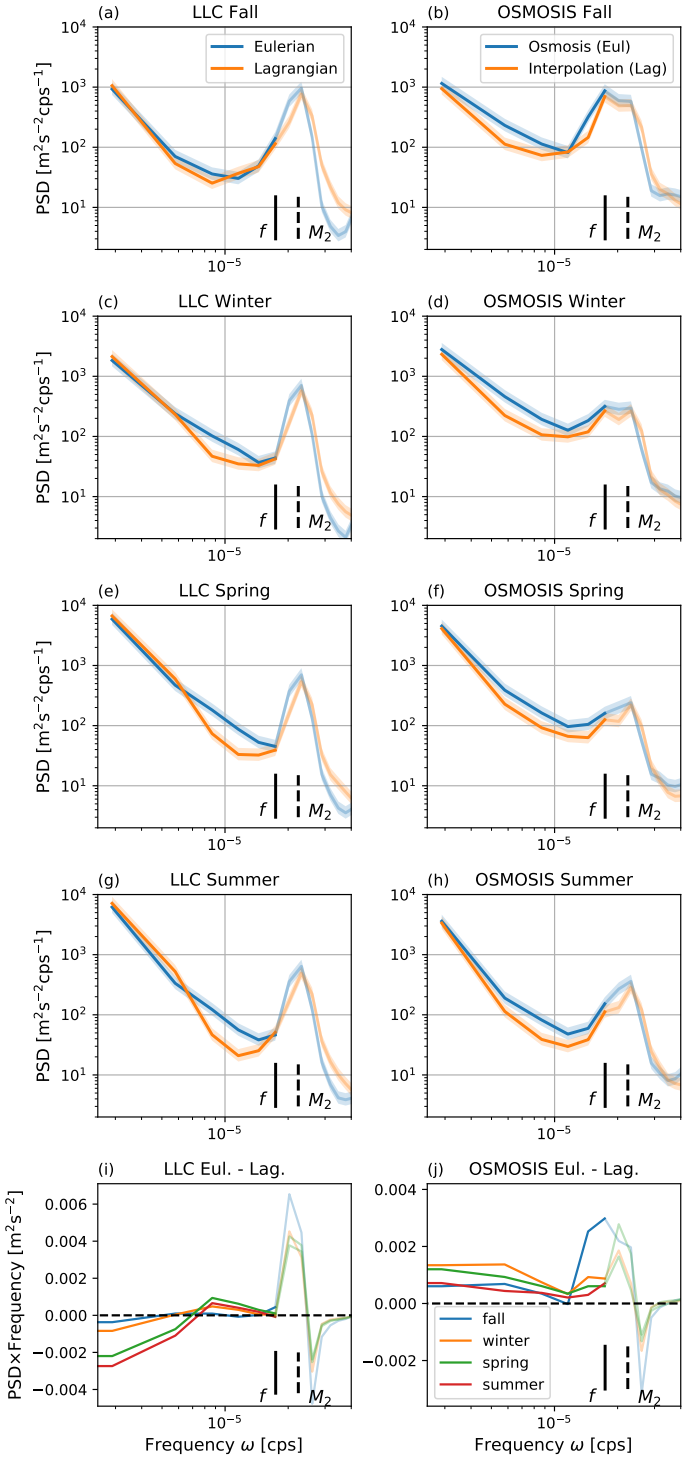

Figure 4.4: (a,c,e,g) LLC 4320 and (b,d,f,h) OSMOSIS interpolation seasonal frequency spectra of kinetic energy. The error bars are shaded around the spectra. (i) LLC 4320 and (j) OSMOSIS interpolation seasonal kinetic energy difference (Eulerian minus Lagrangian) per frequency. The superinertial frequency bands ($>f$) are not the focus of the study and therefore lightly masked.

ertial frequency band. The corresponding Eulerian frequency spectra are estimated from the central mooring using the same spectral estimation procedure.

The Eulerian and Lagrangian frequency spectra obtained this way from OSMOSIS observations resemble those from the numerical simulation (Fig. 4.4). At slightly subinertial (but not the lowest) frequencies, the Lagrangian spectra show less energy than their Eulerian counterparts (Fig. 4.4, right column). This reduction is also visible in the spectral energy difference (Fig. 4.4j), supporting the inference that the Lagrangian evolution of submesoscale turbulence is slower than the Eulerian one. In contrast to the simulation, however, these observationally derived estimates do not show an excess in the Lagrangian spectra at the lowest resolved frequencies. We show in the SI that our reconstruction of the Lagrangian velocity time series, while robustly capturing the reduction at intermediate frequencies, can artificially suppress the Lagrangian spectra at the lowest frequencies. Although not the focus here, the simulations and observations differ substantially at the inertial and tidal frequencies.

4.6 Discussion

The numerical simulation allows us to analyze the full time-evolving velocity field in ways that are difficult—if not impossible—to apply to observations. While the simulation with an effective resolution of about 10 km does capture the key physics at play in the Doppler shifting of submesoscale features by mesoscale flow, it still artificially suppresses motion with scales much smaller than $\sim$10 km. As a result, the simulation does not capture the transition to unbalanced motion. We rely on an extrapolation of the Lagrangian energy spectrum to infer that Ro $\sim$ 1 occurs at $\sim$1 km in the OSMOSIS region. Dynamics operating at scales $\lesssim$1 km, such as energy transfer to small scales (e.g., Capet et al., 2008a; Naveira Garabato et al., 2022) or atmospherically forced unbalanced instabilities (e.g., Thomas et al., 2013), are not captured by the simulation. Future investigations of the transition to unbalanced submesoscale motion should attempt to encompass a much wider range of scales to allow for these dynamics and their potential back-reaction on balanced submesoscale turbulence.

The observational support for substantial Doppler shifting presented above is far from comprehensive. A direct estimation of an ω–κ spectrum, for example from a more regularly spaced mooring array, combined with dense Lagrangian sampling (e.g., D'Asaro et al., 2018), would be desirable. Our analysis does show, however, that Eulerian energy is enhanced relative to Lagrangian energy at slightly subinertial frequencies in both the simulation and the observations. This consistency supports the idea that Doppler shifting of submesoscale motions by mesoscale eddies is at play.

The energy reshuffling identified here is also consistent with the work of Jones et al. (2023), who used Lagrangian filtering to isolate balanced motion (cf., Nagai et al., 2015; Shakespeare et al., 2021). They low-pass filtered simulated velocities in the Agulhas region, using

a filter acting on velocity time series recorded following the path of fluid parcels and with a cutoff around the inertial frequency. When calculating an ω–κ spectrum from these filtered velocities, referenced back to their mean positions on an Eulerian grid, these authors found that submesoscale motion with superinertial Eulerian frequencies had survived the Lagrangian filtering. This observation is consistent with a sizable difference between the timescale of Lagrangian evolution and the timescale registered by a fixed observer. The work presented here extends the analysis of Jones et al. (2023) by providing a full decomposition of the energy into wavenumbers and frequencies in the Lagrangian frame and by supporting the conclusions with observations from the real ocean.

The above analysis has considered the OSMOSIS region, but we expect Doppler shifting to be at play universally. How much energy reshuffling occurs should depend on the relative energy levels of meso- and submesoscale turbulence. The simple model of Section 4.3 produces a frequency ratio $\omega_\mathrm{E}/\omega_\mathrm{L} = U/\kappa\psi_0$, the ratio between meso- and submesoscale velocities. This suggests that Doppler shifting is more pronounced relatively in regimes with weak submesoscale turbulence, as measured relative to mesoscales. For interior geostrophic turbulence (Charney, 1971), for example, the dynamical time scale is close to invariant with scale (e.g., Vallis, 2017), yet QG simulations show a marked increase in Eulerian frequency with wavenumber (Arbic et al., 2014). Strong Doppler shifting also occurs when submesoscale turbulence is vigorous because in these regimes mesoscale flows still dominate over submesoscale motion.

At what scale Eulerian frequencies become superinertial should depend largely on the mesoscale energy level. In the simple model, $\omega_\mathrm{E} = U\kappa \sim f$ implies $\kappa^{-1} \sim U/f$. Given the large variations in the mesoscale energy levels across the world ocean (e.g., Wunsch and Stammer, 1998), this scale should be modulated quite strongly, for example explaining the shift to superinertial frequencies at ∼10 km in the OSMOSIS region and at ∼50 km in the more energetic Kuroshio region analyzed by Torres et al. (2018). The varying energy levels of submesoscale turbulence between regions and seasons also imply that the transition to unbalanced motion, i.e., to Lagrangian time scales $\sim f^{-1}$, should show sizable variations in space and in time.

It should be noted that some authors define "submesoscale" motions as those with $\mathrm{Ro} \gtrsim 1$ (e.g., Thomas et al., 2008; McWilliams, 2016; Taylor and Thompson, 2023). If the transition to this regime occurs at scales ∼1 km, however, this would leave two order of magnitude in spatial scales between what is traditionally thought of as the "mesoscale" (∼100 km) and this "submesoscale" regime. The dynamics at these intermediate scales are distinct from mesoscale eddies, energized importantly by baroclinic instabilities concentrated in the mixed layer rather than spanning the thermocline. And even in entirely balanced dynamics, vertical velocities can sharply increase as the horizontal scale is reduced, as suggested by the QG scaling $W \sim \mathrm{Ro}HU/L$. If balanced turbulence is energetic in a mixed layer of depth H,

the increase in Ro and the decrease in L overwhelm the decrease in U and produce more vigorous vertical motion as we move to small scales (e.g., Capet et al., 2008b; Callies et al., 2016). We therefore find that it is warranted to include this range of intermediate scales in what we mean by "submesoscales" but suggest that future work should clearly state how the term "submesoscale" is deployed until a more widely accepted use is established.

While we have discussed QG and SG theory together as describing the balanced part of the flow, SG theory can explain features of submesoscale turbulence that QG theory cannot. The advection by ageostrophic flow included in SG theory allows for accelerated frontogenesis and the production of asymmetries between cyclonic and anticyclonic regions, which has been observed repeatedly in energetic submesoscale turbulence (Rudnick, 2001; Shcherbina et al., 2013; Buckingham et al., 2016). As emphasized by Hoskins (1975), SG theory avoids assuming universal scales to define Ro but instead compares the evolution along the path of fluid parcels with the inertial time scale, in line with how we have argued here that the transition to unbalanced motion should be characterized by the Lagrangian time scale. We therefore expect that SG theory could be used with considerable success to explain motions down to $\sim$1 km in the upper ocean (cf., Thomas et al., 2008; Badin, 2013).

4.7 Conclusion

Submesoscale turbulence in the upper ocean is affected by Doppler shifting. An Eulerian observer measures rapid flow variations because submesoscale features are swept past the observer by the mesoscale flow, while the Lagrangian evolution of the submesoscale feature is substantially slower. This effect is important for our dynamical understanding of submesoscale turbulence because submesoscale flow can appear superinertial in the Eulerian frame while remaining subinertial in the Lagrangian frame. Despite the superinertial Eulerian evolution, momentum advection then remains subdominant to Coriolis and pressure gradient terms (Ro $\ll 1$), and theories built on subinertial evolution can be applied. In the region of the Northeast Atlantic analyzed here, simulation and observations indicate that this effect shifts the transition to superinertial motion from $\sim$10 km in the Eulerian frame to $\sim$1 km in the Lagrangian frame. Balanced theories should be successful down to scales $\sim$1 km, consistent with previous more indirect inferences (Shcherbina et al., 2013; Callies et al., 2015, 2020).

These observations support the view that submesoscale turbulence at $\sim$10 km is energized primarily by balanced baroclinic instabilities in the winter mixed layer (Boccaletti et al., 2007; Callies et al., 2015). A wide range of properties of the observed spectral and vertical distribution of energy can be captured using QG theory (Callies et al., 2016), which would have been surprising if balance broke down at $\sim$10 km (cf. Torres et al., 2018). These instabilities can be modified by vertical mixing in the mixed layer (e.g., Young and Chen, 1995; Callies and Ferrari, 2018; Crowe and Taylor, 2018, 2019) and by the frontal sharpening described by SG theory, which we view as the most plausible explanation of substantial

dominance of cyclonic over anticyclonic vorticities at scales $\sim$1 km. We recommend that future work explore SG theory more fully as a tool to understand submesoscale dynamics.

Data Availability Statement

The high-resolution MITgcm simulation (LLC 4320) data used in this study can be accessed through `https://data.nas.nasa.gov/ecco/`. OSMOSIS observational data is available via `https://www.bodc.ac.uk/data/bodc_database/nodb/data_collection/6093/` with specifications of data type as "Current–subsurface Eulerian" and platform as "Subsurface mooring."

Acknowledgment

Y. B. acknowledges support from the National Aeronautics and Space Administration Science Mission Directorate FINESST program under Award
No. 80NSSC21K1635. J. G. F. and J. C. acknowledge support from the National Science Foundation under Grant No. OCE-1924354.

4.8 Supplementary Information

4.8.1 Introduction

This supplementary information provides details on the synthetic velocity mapping from OSMOSIS moorings in Sec. 4.5. We introduce the procedures of generating the synthetic velocity field and validate the Lagrangian advection based on that in the numerical simulation.

4.8.2 Synthetic Lagrangian data from OSMOSIS moorings

Near the OSMOSIS mooring arrays, insufficient Lagrangian observations motivate us to generate synthetic velocity trajectories from a mapping of the velocities measured by the mooring array. To generate this mapping, we divide the ocean in the vicinity of the mooring array into two sub-domains: within and outside of the polygon formed by the outer four moorings. Due to the tight spacing of the four inner moorings with the central mooring, we exclude the measurements from the four inner mooring from the mapping to simplify the interpolation process at minimal cost for the accuracy of the reconstruction. Within the mooring array, triangles are formed by connecting each outer mooring with the center one. Within each of the four triangles thus formed, the mapped velocities are obtained from the mooring measurements on the three vertices by linear interpolation. Outside of the polygon, we assign the mapped velocities based on the velocities at the nearest point on the polygon, which in turn are linearly interpolated between the vertices. An example snapshot of the mapped velocity field is shown in Fig. 4.5.

With these mapped velocities, we can now generate trajectories and Lagrangian time series of velocities along these trajectories, which we subsequently use to estimate Lagrangian

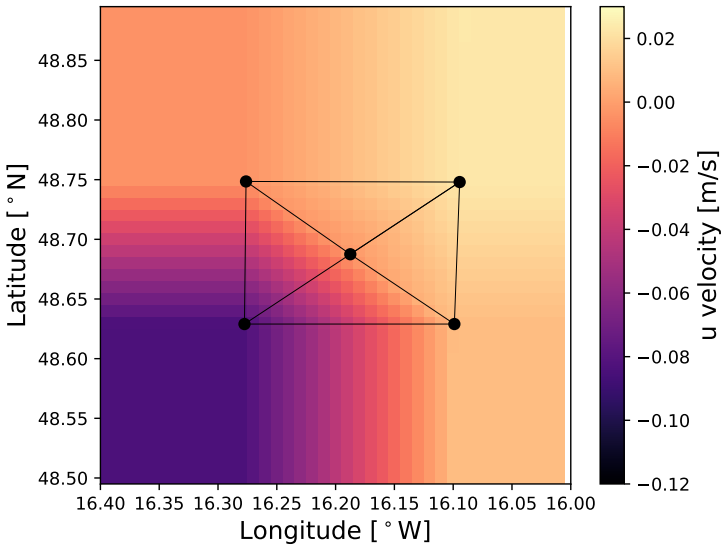

Figure 4.5: Visualization of the velocity mapping from mooring observations, here using data the numerical simulation. Shading represents the mapped velocity field. Black dots show the outer and central mooring locations, where velocity measurements are available. Due to the nature of the triangular interpolation within the polygon, mapped velocities at the vertices exactly match the original measurements, and the reconstructed velocity field is continuous.

frequency spectra (Fig. 4.3). We release the particles at the location of the central mooring and advect them forward and backward for two days. We test this approach here with output from the numerical simulations, comparing the spectra estimated from the limited information captured by the mooring array to those estimated from the full model data. We furthermore test different window lengths for the advection, justifying our choice of a 4-day window as a compromise between the need for a long window for sufficient frequency resolution to differentiate sub- and superinertial frequencies and the need to be short enough for acceptable errors associated with the mapping (Fig. 4.6).

To assess the error in the mapping, we obtain Lagrangian velocity time series from the model simulation by advecting particles with the mapped velocity field, pretending we have velocity data at the mooring locations only (Fig. 4.5). We compare these estimated Lagrangian velocity times series to those obtained by advecting particles with the fully simulated velocity field. We perform this procedure for 2, 4, and 6-day advection windows and evaluate the ratio between the spectral estimate from reconstructed and full velocities (Fig. 4.6). The error in the reconstruction increases with the length of the time window, as expected, because the particles start leaving the confines of the mooring array, such that errors in the velocity mapping become large. The reconstruction underestimates the true spectrum at the lowest frequencies and overestimates it at higher but still subinertial frequencies. This reconstruction error opposes the effect expected from reshuffling between the Eulerian and Lagrangian perspectives, so a remaining reshuffling signal is unlikely caused by the resonstruction. We further evaluate the error in the reconstruction of the 4-day Lagrangian spectrum in relation

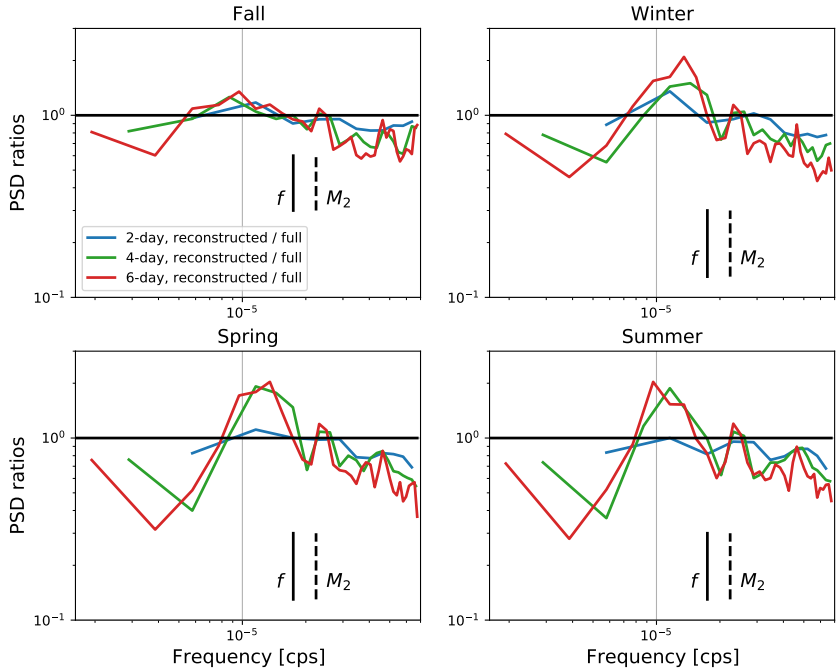

Figure 4.6: Reconstruction error in Lagrangian frequency spectra at different advection windows. Shown are the ratios between the reconstructed and full Lagrangian spectra, both calculated from the numerical simulation, for each season. The advection intervals are 2, 4, and 6 days (blue, green, and red, respectively). Particles are advected forward and backward for half of these intervals, with a reference location at the central mooring.

to the difference with the Eulerian spectrum at the central mooring—the target of our investigation (Fig. 4.7). The errors arising from the reconstruction are of a similar magnitude as the difference with the Eulerian spectra, but they are generally small enough to not qualitatively change the diagnosed energy reshuffling. One exception is that underestimation at the lowest frequencies is large enough to suppress the reconstructed Lagrangian spectra to below the energy level of the Eulerian frequency spectra, reversing the ordering. For the OSMOSIS observations, we also find that the reconstructed Lagrangian spectra fall below the Eulerian ones at the lowest resolved frequencies (Fig. 4.4). Based on this consistency between the observations and the model results, we surmise that this suppression at low frequencies is again due to the reconstruction error, caused by the small spatial coverage of available mooring measurements limiting the ability to capture mesoscale features.

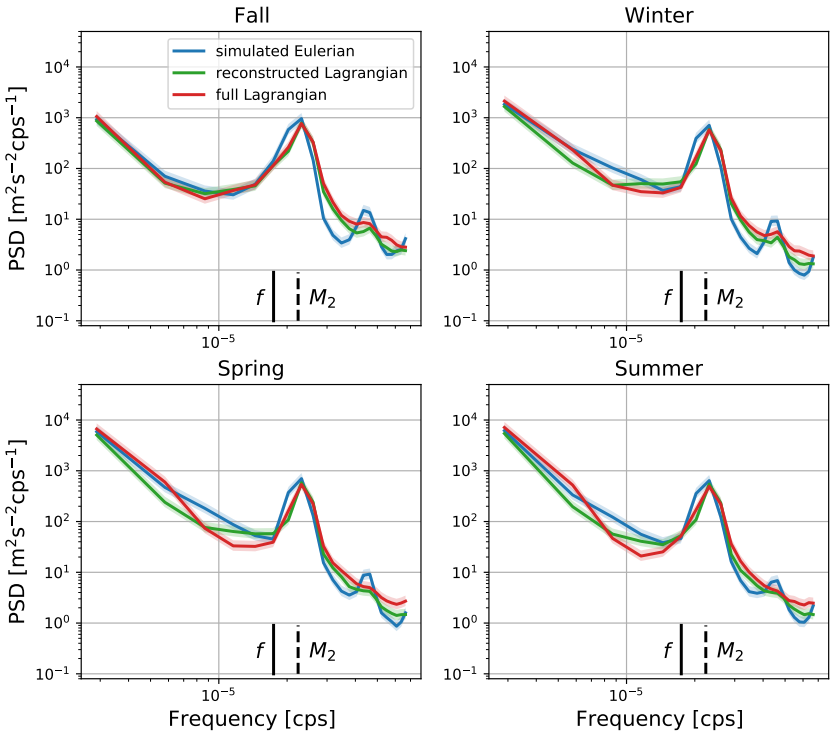

Figure 4.7: Comparison between Lagrangian (full and reconstructed) and Eulerian frequency spectra in the numerical simulation using a 4-day advection window. Seasonal kinetic energy spectra are calculated following the same procedure as in the main text. The Lagrangian spectra estimated using the velocities reconstructed from (simulated) mooring observations (green) match the Lagrangian spectra estimated using the full velocities (red) fairly closely in the subinertial frequency band. For all seasons other than fall, the reconstructed spectra underestimate the true spectra at the lowest resolved frequencies and overestimate it at higher but still subinertial frequencies. The comparison to the Eulerian spectra (blue) is not qualitatively distorted.

Chapter 5

ENERGETICS OF FRONTOGENESIS IN SIMPLE BALANCED MODELS

5.1 Abstract

Submesoscale fronts have been proposed to act as conduits funneling kinetic energy from geostrophically constrained mesoscale eddies down to small scales, where the energy can be dissipated. Realistic primitive-equation simulations suggest that the downscale energy transfer at submesoscales is strongly concentrated in sharpening fronts, and the convergence on the cyclonic side of fronts has been found to dominate the transfer. This study explores how much of this phenomenology can be captured by simple quasi-geostrophic (QG) and semi-geostrophic (SG) theories of frontogenesis. An analysis of the kinetic energy budget of classical strain-induced frontogenesis shows that there is downscale transfer in both QG and SG fronts. In QG frontogenesis, the narrowing jet along the sharpening front is powered by buoyancy production, but downscale transfer due to the strain field plays an important role. In SG frontogenesis, where the sharpening of the front is accelerated by the ageostrophic cross-frontal circulation, ageostrophic advection enhances this downscale transfer on the cyclonic side of the front, where the surface flow is convergent. On the anticyclonic side, where the ageostrophic circulation is divergent, the ageostrophic scale transfer of kinetic energy is upscale, counteracting the geostrophic downscale transfer. While matching the patterns found in primitive-equation simulations, the ageostrophic scale transfers play an important but not dominant role in the adiabatic and frictionless theory considered here. This points to the importance of mixed-layer turbulence in inducing the ageostrophic circulation and the associated scale transfers.

5.2 Introduction

Kinetic energy in the ocean is distributed across a wide range of spatial scales, with mesoscale eddies containing some 80% of the total (Ferrari and Wunsch, 2009; Chelton et al., 2011b). At mesoscales, the ocean is strongly influenced by Earth's rotation and stratification, placing mesoscale eddies in the quasi-geostrophic regime. In this regime, the classical dual-cascade paradigm of geostrophic turbulence is thought to apply (Rhines, 1977; Salmon, 1978). Large-scale available potential energy is transferred downscale and converted to kinetic energy by mesoscale baroclinic instability. Due to the geostrophic constraint, nonlinear triad interactions subsequently transfer this kinetic energy back to larger scales (Kraichnan, 1967; Charney, 1971; Scott and Wang, 2005; Tulloch et al., 2011; Arbic et al., 2013). This inverse cascade prompts the question of how kinetic energy is dissipated to balance the mesoscale source—somehow, the energy must be transferred to small scales where viscous dissipation can act. Many processes are thought to play a role. Interaction with the bottom,

especially at western boundaries (Zhai et al., 2010), can generate boundary layer turbulence and produce dissipation (e.g., Ferrari and Wunsch, 2009). Flow over topography also produces lee waves, whose breaking allows them exert a net drag (e.g., Nikurashin et al., 2013). Wind forcing, although acting as a net source of kinetic energy at large scales, produces a top drag at mesoscales through the current dependence of the wind stress (Dewar and Flierl, 1987; Duhaut and Straub, 2006; Renault et al., 2016b), and it can cause symmetric instabilities that extract kinetic energy from the geostrophic flow (Thomas et al., 2013). The interaction with internal waves, especially wind-forced near-inertial waves, can extract energy from mesoscale eddies (Xie and Vanneste, 2015; Rocha et al., 2018; Asselin and Young, 2020).

Another route to dissipation is the possibility that the geostrophic constraint is broken in the upper ocean and energy is transferred to small scales by energetic submesoscale turbulence (Capet et al., 2008c; Müller et al., 2011). The close analogy between geostrophic turbulence (Charney, 1971) and two-dimensional turbulence (Kraichnan, 1967) is broken in the upper ocean, and observations deviate from the geostrophic turbulence prediction of weak submesoscales (Shcherbina et al., 2013; Callies et al., 2015; Buckingham et al., 2016). The mere presence of the ocean's surface allows for the sharpening of buoyancy gradients and energization of submesoscale turbulence through surface quasi-geostrophic dynamics (Blumen, 1978-; Held et al., 1995; Lapeyre and Klein, 2006; Capet et al., 2008a). Furthermore, the discontinuity of potential vorticity (PV) at the base of the mixed layer allows for a submesoscale baroclinic instability of lateral buoyancy gradients (Haine and Marshall, 1998; Boccaletti et al., 2007; Fox-Kemper et al., 2008; Callies et al., 2016). Especially in deep winter mixed layers, these mixed-layer instabilities appear to inject kinetic energy at submesoscales (Mensa et al., 2013; Callies et al., 2015), and triad interactions spread it across a wide range of scales (Sasaki et al., 2014; Callies et al., 2016; Schubert et al., 2020; Lawrence and Callies, 2022). While both of these scenarios produce a submesoscale energy transfer that is primarily to large scales, primitive-equation simulations exhibit a small but robust downscale transfer if the resolution is sufficiently high (Capet et al., 2008c).

Recently, Srinivasan et al. (2023) linked this downscale transfer of kinetic energy to the formation of fronts. Both flavors of submesoscale turbulence mentioned above tend to generate fronts, either by straining between mesoscale eddies or by lateral shearing induced by mixed-layer instabilities. At the surface, these fronts can sharpen without bound (Stone, 1966) and collapse into discontinuities (Hoskins and Bretherton, 1972). When Srinivasan et al. (2023) mapped out the submesoscale scale transfer of kinetic energy, fronts were revealed to play the dominant role (Fig. 5.1). Fronts tended to show a dipole of energy transfer, with a downscale transfer on the cyclonic side of the front, at which the horizontal flow is convergent, dominating over an upscale transfer on the anticyclonic side, at which the horizontal flow is divergent. Barkan et al. (2019); Srinivasan et al. (2023) emphasized the role of convergence in frontogenesis and the downscale energy transfer, and they appealed to mixed-layer turbu-

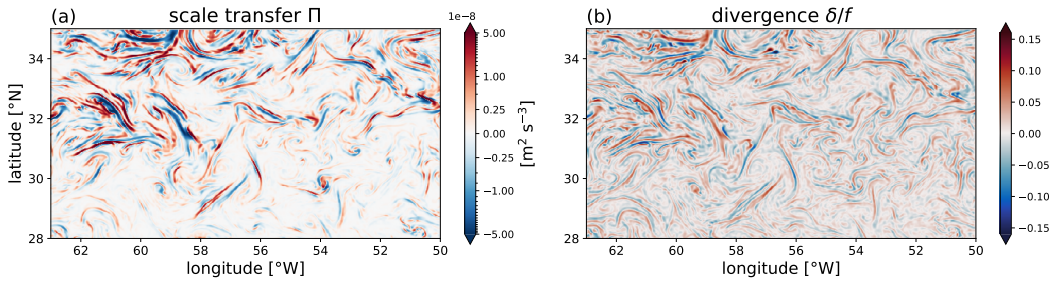

Figure 5.1: Scale transfer and horizontal divergence at submesoscale fronts in a realistic primitive-equation model. Shown are (a) the scale transfers at a Gaussian filter scale of $\sigma = 3$ km and (b) a coincident snapshot of divergence filtered to the same scale, exhibiting a tight correspondence (anti-correlation) between the two. Note the arsinh-scaled color map in (a). The simulation is described in Sinha et al. (2023); we here show surface fields from January 3rd.

lence as an important driver of an ageostrophic cross-frontal circulation, convergence, and frontal sharpening.

Nevertheless, the mechanism of a downscale transfer of kinetic energy at sharpening fronts should be generic, and we explore it here using simple balanced models of frontogenesis. We ask how much of the phenomenology of kinetic energy transfer observed in realistic primitive-equation models and drifter observations (Barkan et al., 2019; Srinivasan et al., 2023) can be reproduced by these simple models. In particular, we consider the strain-induced sharpening of a surface front as the archetype of frontogenesis. We consider the QG dynamics as described by Stone (1966) and the SG dynamics as described by Hoskins and Bretherton (1972). In QG dynamics, as the strain field pushes together a pre-existing buoyancy gradient, a secondary circulation develops that upwells dense water on the light side of the front and downwells light water on the dense side, counteracting its sharpening. At the surface, however, no such vertical advection is present, and the strain field is left to sharpen the buoyancy field exponentially. In SG dynamics, this sharpening at the surface is further enhanced by the horizontal advection by the ageostrophic circulation, which is neglected in QG dynamics but taken into account in SG dynamics. The ageostrophic circulation pushes the sharpening front over to the cyclonic side, leaving it in a region of surface convergence that accelerates its sharpening. The front sharpens super-exponentially and collapses into a discontinuity in finite time. While these austere models of frontogenesis do not capture the fact that fronts are embedded in a turbulent meso- and submesoscale eddy field, and they neglect the impact of mixed-layer turbulence, the dynamics are transparent and well-understood, offering clear insight into how kinetic energy is transferred downscale at fronts.

We quantify the scale-resolved kinetic energy budget of frontogenesis using a spectral budget and a coarse-graining approach. The spectral budget quantifies the net role of downscale kinetic energy transfer in energizing the sharpening along-front jet, relative to buoyancy production and other terms in the budget (Section 5.4.1). The coarse-graining approach further

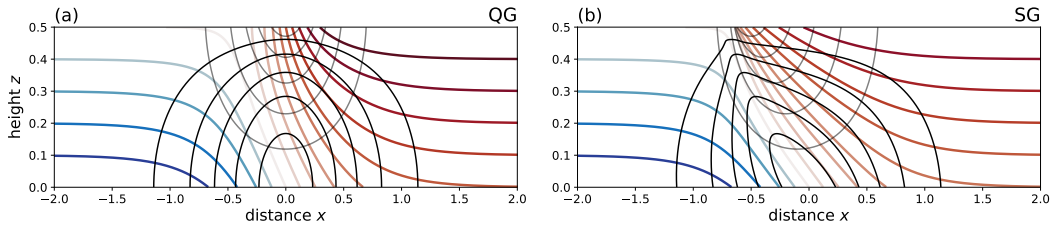

Figure 5.2: Quasi-geostrophic and semi-geostrophic fronts. (a) The buoyancy field $N^2z + b_0$ (color), the along-front flow v_0 (gray), and the ageostrophic cross-frontal circulation χ (black) for the QG solution. (b) The buoyancy field b (color), the along-front flow v_g (gray), and the ageostrophic cross-frontal circulation χ (black) for the SG solution. The fields are shown at $t = 1.33$ and for $\gamma = 1$. All variables are dimensionless (see Appendix 5.7).

localizes scale transfers, revealing geostrophic downscale transfer on both flanks of the front and a dipole of ageostrophic transfer, with a downscale transfer on the cyclonic side of the front and an upscale transfer on the anticyclonic side (Section 5.4.2). We discuss how these results compare to more realistic flows and highlight the limitations of the simple models studied here (Section 5.5).

5.3 Frontogenesis: evolution and energy budget

This section introduces the frontal setup and reviews the frontal evolution under both QG and SG dynamics, closely following Stone (1966); Hoskins and Bretherton (1972). We derive kinetic energy equations in physical and spectral space, and we apply the coarse-graining framework to the frontal setup. Readers already familiar with the QG and SG dynamics of a strain-driven front may skip Sections 5.3.2 and 5.3.3 and proceed to Sections 5.3.4 and 5.3.5 for the discussion of scale-resolved energy budgets, although we encourage them to review the kinetic energy budgets (5.14) and (5.35) before proceeding.

5.3.1 Frontal setup

We consider classic strain-driven frontogenesis. A strain field $U = -\alpha x$ and $V = \alpha y$, with a fixed strain rate α, is imposed and acts on a pre-existing buoyancy gradient in the x-direction. The initial buoyancy field $b = N^2z + B(x)$ is prescribed at the top and bottom boundaries of the domain, taken to be rigid and located at $z = \pm H/2$:

$$b = N^2z + B(x) = N^2z + \frac{\Delta}{2}\tanh\frac{x}{L} \quad \text{at} \quad z = \pm\frac{H}{2}, \quad t = 0. \tag{5.1}$$

This represents a buoyancy front with initial width L and a buoyancy difference Δ across the front. In the interior, we assume that the potential vorticity (PV) is uniform, which implies the interior buoyancy and flow fields by the respective balance statement (see below). The buoyancy field is independent of y and remains so over the course of the evolution because the frontal flow, the departure from the imposed strain field, is also independent of y. Frontal instabilities are not allowed to develop.

We proceed by listing the momentum and buoyancy equations that describe the evolution of

the front under QG and SG assumptions. In both cases, the dynamics are best cast in terms of buoyancy advection at the boundaries and an inversion statement that determines the flow given the field of buoyancy at the boundaries. We also state the respective omega equations that allow us to explicitly calculate the ageostrophic cross-frontal circulation, and we derive the respective kinetic energy equations. While the cross-frontal circulation is not needed to determine the evolution, it plays an important role in the dynamics. Horizontal advection by the ageostrophic circulation, neglected in QG and retained in SG, distinguishes the two theories. While the front remains symmetric in QG, it is tilted over by the ageostrophic circulation in SG, and frontogenesis is accelerated by the horizontal convergence of the ageostrophic flow on the cyclonic side of the front (Fig. 5.2), leading to frontal collapse in finite time.

5.3.2 Frontal evolution and kinetic energy in QG

Following the usual approach to QG dynamics (e.g., Pedlosky, 1987), we expand the flow variables of the Boussinesq equations in a perturbation series in a Rossby number $\varepsilon \ll 1$: the cross-front velocity $u = u_0 + \varepsilon u_1 + \ldots$, the along-front velocity $v = v_0 + \varepsilon v_1 + \ldots$, the vertical velocity $w = w_0 + w_1 + \ldots$, the buoyancy $b = N^2 z + b_0 + \varepsilon b_1 + \ldots$, and the geopotential $\phi = \frac{1}{2} N^2 z^2 + \phi_0 + \varepsilon \phi_1 + \ldots$ The buoyancy and geopotential $\phi = p/\rho_0$ include background terms that represent a hydrostatically balanced constant stratification N^2. In QG scaling, the background stratification is assumed to be strong, such that the zeroth-order buoyancy equation implies $w_0 = 0$. The zeroth-order momentum equations are

$$-f v_0 = -\frac{\partial \phi_0}{\partial x}, \tag{5.2}$$

$$f u_0 = 0, \tag{5.3}$$

$$0 = -\frac{\partial \phi_0}{\partial z} + b_0; \tag{5.4}$$

and the first-order equations are

$$-f v_1 = -\frac{\partial \phi_1}{\partial x}, \tag{5.5}$$

$$\frac{\partial v_0}{\partial t} - \alpha x \frac{\partial v_0}{\partial x} + \alpha v_0 + f u_1 = 0, \tag{5.6}$$

$$0 = -\frac{\partial \phi_1}{\partial z} + b_1. \tag{5.7}$$

The advection terms in (5.6) arise from the strain field advecting the geostrophic along-front geostrophic flow v_0 and the along-front geostrophic flow v_0 advecting the strain field.

The assumption of a uniform interior PV implies that the QGPV vanishes identically, such that the evolution is fully governed by the advection of zeroth-order buoyancy at the top and bottom boundaries:

$$\frac{\partial b_0}{\partial t} - \alpha x \frac{\partial b_0}{\partial x} = 0 \quad \text{at} \quad z = \pm \frac{H}{2}. \tag{5.8}$$

Given the absence of along-front buoyancy gradients and of a cross-front geostrophic flow, buoyancy is advected by the strain field only, and the initial buoyancy gradient is sharpened exponentially:

$$b_0(x, z, t) = B(xe^{\alpha t}) \quad \text{at} \quad z = \pm\frac{H}{2}. \tag{5.9}$$

This buoyancy solution at the boundaries can be applied at any time t and provides the boundary conditions for the inversion relation that can be solved for the zeroth-order geopotential ϕ_0:

$$\frac{\partial^2\phi_0}{\partial x^2} + \frac{f^2}{N^2}\frac{\partial^2\phi_0}{\partial z^2} = 0, \quad \frac{\partial\phi_0}{\partial z} = B(x^{\alpha t}) \quad \text{at} \quad z = \pm\frac{H}{2}. \tag{5.10}$$

The streamfunction then determines the interior buoyancy field $b_0 = \partial_z\phi_0$ and the along-front geostrophic flow $v_0 = f^{-1}\partial_x\phi_0$.

The sharpening of the buoyancy gradient by the strain field induces an ageostrophic cross-frontal circulation. In the x–z plane, we define the streamfunction χ of the cross-frontal circulation,

$$u_1 = -\frac{\partial\chi}{\partial z} \quad \text{and} \quad w_1 = \frac{\partial\chi}{\partial x}, \tag{5.11}$$

and diagnose it using the omega equation

$$N^2\frac{\partial^2\chi}{\partial x^2} + f^2\frac{\partial^2\chi}{\partial z^2} = 2\alpha\frac{\partial b_0}{\partial x}. \tag{5.12}$$

As usual, the vertical advection by this ageostrophic circulation is taken into account implicitly in the evolution of the front as described by buoyancy advection on the boundaries and the inversion relation. We solve all equations in Fourier space in the horizontal, using discrete sine and cosine transforms, and we apply an analytical vertical structure for each horizontal wavenumber.

The rigid-lid condition $w_1 = 0$ at $z = \pm H/2$ allows the strain field to sharpen the front most rapidly there (Fig. 5.2a, colored contours). An along-front geostrophic flow v_0 develops with its maximum at the surface and center of the domain (Fig. 5.2a, gray). In the interior, the sharpening of the cross-frontal buoyancy gradient induces an ageostrophic circulation (Fig. 5.2a, black) that consists of downwelling on the dense side of the front and upwelling on the light side. This acts to flatten the cross-frontal buoyancy gradient and counteracts its sharpening by the strain field in the interior, such that the interior buoyancy gradient remains modest. This QG frontal evolution remains symmetric around $x = 0$ because only the strain field advects buoyancy and the geostrophic along-front momentum.

The kinetic energy budget involves both zeroth-order and first-order quantities, diagnosed from the inversion relation (5.10) and omega equation (5.12). The equation for the geostrophic kinetic energy $\frac{1}{2}v_0^2$ is formed by taking the sum of (5.2)–(5.4) dotted with the first-order velocity vector (u_1, v_1, w_1) and (5.5)–(5.7) dotted with the zeroth-order velocity vector $(0, v_0, 0)$:

$$\frac{\partial}{\partial t}\frac{v_0^2}{2} - \alpha x\frac{\partial}{\partial x}\frac{v_0^2}{2} + \alpha v_0^2 + u_1\frac{\partial\phi_0}{\partial x} + w_1\frac{\partial\phi_0}{\partial z} = w_1 b_0. \tag{5.13}$$

Written in flux form, taking advantage of the non-divergence of (u_1, w_1) in the x–z plane, this becomes

$$\frac{\partial}{\partial t}\frac{v_0^2}{2} + \frac{\partial}{\partial x}\left(-\alpha x \frac{v_0^2}{2} + u_1\phi_0 \right) + \frac{\partial}{\partial z}\left(w_1\phi_0 \right) + \frac{3}{2}\alpha v_0^2 = w_1 b_0. \tag{5.14}$$

This equation indicates that there is a sink $-\frac{3}{2}\alpha v_0^2$ of geostrophic kinetic energy density that arises from a combination of the strain field stretching out the front in the y-direction and the shear production term $-\alpha v_0^2$. It is important to treat this term as a sink rather an advective redistribution. The redistribution terms, in contrast, vanish upon integration over x and z as long as the front is sufficiently confined, as is the case in the example considered in this paper.

5.3.3 Frontal evolution and kinetic energy in SG

Following Hoskins and Bretherton (1972), we now take into account the horizontal advection by the ageostrophic cross-frontal circulation by making the geostrophic momentum approximation rather than the QG approximation. We define the geostrophic velocities as

$$v_g \equiv \frac{1}{f}\frac{\partial \phi}{\partial x} \quad \text{and} \quad u_g \equiv -\frac{1}{f}\frac{\partial \phi}{\partial y} = 0, \tag{5.15}$$

and we write the SG momentum equations as

$$-fv = -\frac{\partial \phi}{\partial x}, \tag{5.16}$$

$$\frac{\partial v_g}{\partial t} + (-\alpha x + u)\frac{\partial v_g}{\partial x} + w\frac{\partial v_g}{\partial z} + \alpha v_g + fu = 0, \tag{5.17}$$

$$0 = -\frac{\partial \phi}{\partial z} + b. \tag{5.18}$$

We note that (5.16) implies that $v = v_g$. The buoyancy equation also now includes the full ageostrophic advection:

$$\frac{\partial b}{\partial t} + (-\alpha x + u)\frac{\partial b}{\partial x} + w\frac{\partial b}{\partial z} = 0. \tag{5.19}$$

These equations for the evolution of a strain-driven front are most easily solved by performing a coordinate transformation to geostrophic coordinates:

$$X = x + \frac{v_g}{f}, \quad Z = z, \quad T = t. \tag{5.20}$$

We further define the modified geopotential

$$\Phi = \phi + \frac{v_g^2}{2}, \tag{5.21}$$

such that

$$fv_g = \frac{\partial \phi}{\partial x} = \frac{\partial \Phi}{\partial X}, \quad b = \frac{\partial \phi}{\partial z} = \frac{\partial \Phi}{\partial Z}, \tag{5.22}$$

in close analogy with the leading-order balances in QG. Based on this coordinate transformation, the along-front momentum and buoyancy equations (5.17) and (5.19) simplify to:

$$\frac{\partial v_g}{\partial T} - \alpha X \frac{\partial v_g}{\partial X} + w \frac{\partial v_g}{\partial Z} + \alpha v_g + f u = 0, \tag{5.23}$$

$$\frac{\partial b}{\partial T} - \alpha X \frac{\partial b}{\partial X} + w \frac{\partial b}{\partial Z} = 0. \tag{5.24}$$

Notably, horizontal advection is by the strain field only in these coordinates, just like in QG. At $z = \pm H/2$, where $w = 0$, the buoyancy equation takes the same form as in QG. The perturbation buoyancy $b' \equiv b - N^2 z$ can thus be solved for at the boundaries as before:

$$b'(X, Z, T) = B(X e^{\alpha T}) \quad \text{at} \quad Z = \pm \frac{H}{2}. \tag{5.25}$$

Furthermore, the inversion relation takes the same form as in QG as well, such that the evolution is entirely analogous except that it occurs in geostrophic coordinates—the ageostrophic advection is implicit in the coordinate transformation back to physical space.

The SG inversion relation in geostrophic coordinates is

$$\frac{1}{f^2} \frac{\partial^2 \Phi}{\partial X^2} + \frac{f}{q_g} \frac{\partial^2 \Phi}{\partial Z^2} = 1, \tag{5.26}$$

in which

$$q_g = \left(f + \frac{\partial v_g}{\partial x} \right) \frac{\partial b}{\partial z} - \frac{\partial v_g}{\partial z} \frac{\partial b}{\partial x} = f N^2 \tag{5.27}$$

is the geostrophic potential vorticity, which we set to the uniform value of the unperturbed fluid. Conservation of geostrophic potential vorticity implies that q_g will remain at this value for all time. If we further split Φ into a background and a perturbation component,

$$\Phi = \frac{1}{2} N^2 z^2 + \Phi', \tag{5.28}$$

the inversion relation for the perturbation becomes

$$\frac{\partial^2 \Phi'}{\partial X^2} + \frac{f^2}{N^2} \frac{\partial^2 \Phi'}{\partial Z^2} = 0, \quad \frac{\partial \Phi'}{\partial z} = B(X e^{\alpha T}) \quad \text{at} \quad Z = \pm \frac{H}{2}, \tag{5.29}$$

which has the same form as the QG inversion relation in (5.10).

The SG omega equation is derived following Hoskins and Draghici (1977). We write (5.23) and (5.24) as

$$\frac{\partial v_g}{\partial T} - \alpha X \frac{\partial v_g}{\partial X} + \alpha v_g + f \tilde{u} = 0, \tag{5.30}$$

$$\frac{\partial b}{\partial T} - \alpha X \frac{\partial b}{\partial X} + \tilde{w} N^2 = 0, \tag{5.31}$$

where

$$\tilde{u} = u + \frac{w}{f} \frac{\partial v_g}{\partial Z}, \quad \tilde{w} = \frac{w}{J}, \quad \text{and} \quad J \equiv 1 + \frac{1}{f} \frac{\partial v_g}{\partial x} = \left(1 - \frac{1}{f} \frac{\partial v_g}{\partial X} \right)^{-1}. \tag{5.32}$$

These redefined velocities in the cross-front plane are also nondivergent, so we obtain the SG omega equation

$$N^2 \frac{\partial^2 \tilde{\chi}}{\partial X^2} + f^2 \frac{\partial^2 \tilde{\chi}}{\partial Z^2} = 2\alpha \frac{\partial b}{\partial X} \tag{5.33}$$

for the cross-front streamfunction of the redefined velocities,

$$\tilde{u} = -\frac{\partial \tilde{\chi}}{\partial Z}, \quad \tilde{w} = \frac{\partial \tilde{\chi}}{\partial X}. \tag{5.34}$$

Aside from being formulated in geostrophic coordinates and for the redefined velocities, this has again the same form as the QG omega equation, so QG solutions to the frontal evolution can be translated to SG by applying the transformation (5.32) and the coordinate transformation (5.20).

In physical space, the frontal evolution in SG (Fig. 5.2b) differs distinctly from the QG case (Fig. 5.2a). The coordinate transformation in (5.20), which encodes the ageostrophic advection, slumps the surface front toward the dense cyclonic side. The core of the front, where the along-front geostrophic velocity v_g is the strongest (Fig. 5.2b, grey), is also shifted. The cyclonic side of the front is compressed, while the anticyclonic side is stretched. This slumping further places the front in a region in which the ageostrophic cross-frontal circulation is horizontally convergent, which accelerates the sharpening of the surface buoyancy gradient (Fig. 5.2b, color) and causes frontal collapse in finite time. In the interior, the ageostrophic circulation (Fig. 5.2b, black) is also visibly distorted compared with the QG solution. It is characterized by a stronger and concentrated downwelling on the dense cyclonic side of the front, while the upwelling becomes weaker and more expansive on the light anticyclonic side.

With the solution for the geostrophic and ageostrophic flow as well as the buoyancy field in hand, we can diagnose all terms in the SG kinetic energy budget. We form this budget by dotting (5.16)–(5.18) with the flow (u, v, w):

$$\frac{\partial}{\partial t}\frac{v_g^2}{2} + \frac{\partial}{\partial x}\left[(-\alpha x + u)\frac{v_g^2}{2} + u\phi\right] + \frac{\partial}{\partial z}\left[w\frac{v_g^2}{2} + w\phi\right] + \frac{3}{2}\alpha v_g^2 = wb. \tag{5.35}$$

This equation, in comparison with the QG budget (5.13), includes the additional advection terms of geostrophic kinetic energy by the ageostrophic velocities (u, w). This ageostrophic advection contributes to the scale transfer of kinetic energy, as discussed next.

5.3.4 Spectral kinetic energy budgets

The spectral energy budgets are derived following a standard procedure. First, a Fourier transform is applied to the momentum equations. The transformed equations are then dotted with the complex conjugate of the Fourier transform of the velocity vector, analogous to the formation of the kinetic energy equations in physical space discussed above. Taking the real

part then yields the respective kinetic energy equation. For QG,

$$\underbrace{\frac{\partial}{\partial t}\frac{|\hat{v}_0|^2}{2}}_{\text{tendency}} \underbrace{- \operatorname{Re} \hat{v}_0^* \widehat{\alpha x \frac{\partial v_0}{\partial x}} - \frac{\alpha}{2}|\hat{v}_0|^2}_{\text{geostrophic advection}} \underbrace{+ k \operatorname{Im} \hat{u}_1^* \hat{\phi}_0 + \operatorname{Re} \frac{\partial}{\partial z}\left(\hat{w}_1^* \hat{\phi}_0\right)}_{\text{pressure work}} \underbrace{+ \frac{3}{2}\alpha|\hat{v}_0|^2}_{\text{sink}} = \underbrace{\operatorname{Re} \hat{w}_1^* \hat{b}_0}_{\text{buoy. prod.}}, \tag{5.36}$$

and for SG,

$$\underbrace{\frac{\partial}{\partial t}\frac{|\hat{v}_g|^2}{2}}_{\text{tendency}} \underbrace{- \operatorname{Re} \hat{v}_g^* \widehat{\alpha x \frac{\partial v_g}{\partial x}} - \frac{\alpha}{2}|\hat{v}_g|^2}_{\text{geostrophic advection}} \underbrace{+ \operatorname{Re} \hat{v}_g^* \widehat{u \frac{\partial v_g}{\partial x}} + \operatorname{Re} \hat{v}_g^* \widehat{w \frac{\partial v_g}{\partial z}}}_{\text{agostrophic advection}}$$

$$\underbrace{+ k \operatorname{Im} \hat{u}^* \hat{\phi} + \operatorname{Re} \frac{\partial}{\partial z} \hat{w}^* \hat{\phi}}_{\text{pressure work}} + \underbrace{\frac{3}{2}\alpha|\hat{v}_g|^2}_{\text{sink}} = \underbrace{\operatorname{Re} \hat{w}^* \hat{b}}_{\text{buoy. prod.}} . \tag{5.37}$$

The terms are annotated with the corresponding physical process. As in the budgets in physical space, the sink terms arise from a combination of the along-front stretching and shear production involving the strain field. These processes dilute the kinetic energy density of the front and should be treated as sinks rather than advective scale transfers.

We write the SG spectral energy budget in physical rather than geostrophic coordinates to understand the role of ageostrophic advection and analyze the transfer across the actual spatial scales of the front. In geostrophic coordinates, where the horizontal advection by the ageostrophic flow is implicit, the SG energy budget would take a form very similar to the QG budget, with the exception that vertical advection of geostrophic momentum would still remain. The budget in physical coordinates also allows a more direct comparison with previous diagnostics from realistic primitive-equation simulations as well as observations, which invariably operate in physical coordinates, where ageostrophic advection has been singled out to play an outsized role.

The advection terms in (5.36) and (5.37) redistribute energy and can be written as the divergence of a spectral flux $\Pi(k)$, defined as

$$\Pi(k) = \int_0^k A(\kappa)\, \mathrm{d}\kappa. \tag{5.38}$$

Here, $A(k)$ denotes the advection term under consideration, geostrophic or ageostrophic, QG or SG, as written on the left-hand sides of (5.36) and (5.37). If $\Pi(k) > 0$, energy is transferred from scales larger than k^{-1} to scales smaller than k^{-1}, which we refer to as a downscale transfer. Conversely, a negative $\Pi(k)$ implies an upscale transfer from small to large scales.

5.3.5 Coarse-grained kinetic energy budget

Coarse-grained kinetic energy budgets are derived to assess the spatial distribution of kinetic energy transfer in physical space. The derivation closely follows Aluie et al. (2018), where

additional detail can be found. Here, we specialize the approach to the frontal evolution with a prescribed strain field. We decompose fields into scales larger and smaller than a spatial filter length L using a Gaussian filter. Filtered fields are denoted with an overbar. We begin with a general discussion of the coarse-graining technique applied to departures from a prescribed mean flow. The resulting coarse-grained kinetic energy balance is then applied specifically to the QG and SG frontal cases.

The Boussinesq momentum equation governing the evolution of the flow deviation from a prescribed mean flow is:

$$\frac{\partial u_i}{\partial t} + (U_j + u_j)\frac{\partial u_i}{\partial x_j} + u_j\frac{\partial U_i}{\partial x_j} + f e_{ijk} z_j u_k = -\frac{\partial \phi}{\partial x_i} + b z_i, \tag{5.39}$$

with U_i representing the mean flow, u_i the departure from the mean, z the vertical unit vector, and e_{ijk} the Levi-Civita symbol. Summation over repeated indices is implied. Following Aluie et al. (2018), we apply the filter to (5.39) before multiplying it by the filtered velocity $\overline{u}_i$. After some rearranging, one obtains the following coarse-grained kinetic energy budget:

$$\underbrace{\frac{\partial}{\partial t}\frac{\overline{u}_i^2}{2}}_{\text{tendency}} + \underbrace{\frac{\partial}{\partial x_j}\left[(\overline{U}_j + \overline{u}_j)\frac{\overline{u}_i^2}{2}\right]}_{\text{resolved advection}} + \underbrace{\frac{\partial}{\partial x_j}\left[\overline{u}_i\left(\overline{U_j u_i} - \overline{U}_j\overline{u}_i + \overline{u_j U_i} - \overline{u}_j\overline{U}_i + \overline{u_j u_i} - \overline{u}_j\overline{u}_i\right)\right]}_{\text{subgrid advection}}$$

$$\underbrace{-\frac{\partial \overline{u}_i}{\partial x_j}\left[\overline{U_j u_i} - \overline{U}_j\overline{u}_i + \overline{u_j U_i} - \overline{u}_j\overline{U}_i + \overline{u_j u_i} - \overline{u}_j\overline{u}_i\right]}_{\text{scale transfer }\Pi} + \underbrace{\overline{u}_i\overline{u}_j\frac{\partial \overline{U}_i}{\partial x_j}}_{\text{shear prod.}} + \underbrace{\frac{\partial}{\partial x_i}\left(\overline{u}_i\overline{\phi}\right)}_{\text{pressure work}} = \underbrace{\overline{w}\overline{b}}_{\text{buoy. prod.}}, \tag{5.40}$$

where $w = u_i z_i$ is the vertical velocity. Each term is annotated with the corresponding physical process. The sum of the terms labeled "resolved advection," "subgrid advection," "shear production," and "pressure work" corresponds to the divergence of the transport terms defined in Aluie et al. (2018). We note that Π in this context depends on both the filter scale L and the position x; it must be integrated over x to obtain the scale transfer analogous to the $\Pi(k)$ in the spectral budget.

To apply (5.40) to the QG front, we identify the background strain field components $-\alpha x$ and αy with the mean flow U_i, while the geostrophic velocity v_0 and the ageostrophic velocity components (u_1, w_1) correspond to the fluctuation field u_i. Because the ageostrophic velocities do not participate in momentum advection in QG dynamics, however, only the geostrophic component contributes to the advective terms. We then obtain the following form of the coarse-grained QG kinetic energy equation for the developing front:

$$\underbrace{\frac{\partial}{\partial t}\frac{\overline{v}_0^2}{2}}_{\text{tendency}} + \underbrace{\frac{\partial}{\partial x}\left[\overline{(-\alpha x)}\frac{\overline{v}_0^2}{2}\right]}_{\text{resolved advection}} + \underbrace{\frac{\partial}{\partial x}\left(\overline{v}_0\left[\overline{v_0(-\alpha x)} - \overline{v}_0\overline{(-\alpha x)}\right]\right)}_{\text{subgrid advection}}$$

$$\underbrace{-\frac{\partial \overline{v}_0}{\partial x}\left[\overline{v_0(-\alpha x)} - \overline{v}_0\overline{(-\alpha x)}\right]}_{\text{scale transfer }\Pi} + \underbrace{\frac{3}{2}\alpha\overline{v}_0^2}_{\text{sink}} + \underbrace{\frac{\partial}{\partial z}(\overline{w}_1\overline{\phi}_0) + \frac{\partial}{\partial x}(\overline{u}_1\overline{\phi}_0)}_{\text{pressure work}} = \underbrace{\overline{w}_1\overline{b}_0}_{\text{buoy. prod.}} \quad . \tag{5.41}$$

We note that $\overline{x} = x$.

Similarly, the coarse-grained equation for SG dynamics is derived based on (5.40), with the distinction that the SG geostrophic momentum is additionally advected by the ageostrophic velocities. The coarse-grained SG kinetic energy equation for the strain-driven front is therefore:

$$\underbrace{\frac{\partial}{\partial t}\frac{\overline{v}_g^2}{2}}_{\text{tendency}} + \underbrace{\frac{\partial}{\partial x}\left[\overline{(-\alpha x + u)}\frac{\overline{v}_g^2}{2}\right] + \frac{\partial}{\partial z}\left(\overline{w}\frac{\overline{v}_g^2}{2}\right)}_{\text{resolved advection}}$$

$$\underbrace{+\frac{\partial}{\partial x}\left(\overline{v}_g\left[\overline{v_g(-\alpha x + u)} - \overline{v}_g\overline{(-\alpha x + u)}\right]\right) + \frac{\partial}{\partial z}\left[\overline{v}_g(\overline{v_g w} - \overline{v}_g\overline{w})\right]}_{\text{subgrid advection}}$$

$$\underbrace{-\frac{\partial \overline{v}_g}{\partial x}\left[\overline{v_g(-\alpha x)} - \overline{v}_g\overline{(-\alpha x)}\right] - \frac{\partial \overline{v}_g}{\partial x}(\overline{v_g u} - \overline{v}_g\overline{u}) - \frac{\partial \overline{v}_g}{\partial z}(\overline{v_g w} - \overline{v}_g\overline{w})}_{\text{scale transfer }\Pi}$$

$$\underbrace{+\frac{3}{2}\alpha\overline{v}_g^2}_{\text{sink}} + \underbrace{\frac{\partial}{\partial z}(\overline{w}\overline{\phi}) + \frac{\partial}{\partial x}(\overline{u}\overline{\phi})}_{\text{pressure work}} = \underbrace{\overline{w}\overline{b}}_{\text{buoy. prod.}}. \tag{5.42}$$

The resolved kinetic energy is not only transported by the resolved flow, but the subgrid flow also affects such a transport (labeled "subgrid advection"). Note that the sink terms $\frac{3}{2}\alpha\overline{v}_0^2$ in QG and $\frac{3}{2}\alpha\overline{v}_g^2$ in SG again stem from shear production and the resolved advection in the along-front direction in (5.40), the same as in physical and spectral space. We will further distinguish between the geostrophic (first term) and ageostrophic (second and third terms) scale transfers in SG.

5.3.6 Nondimensionalization

All analysis will be presented in dimensionless form. We use the following scales to nondimensionalize the QG equations:

$$t \sim \alpha^{-1}, \quad x \sim \frac{NH}{f}, \quad z \sim H, \quad v_0 \sim \frac{\Delta}{N}, \quad u_1 \sim \frac{\alpha\Delta}{fN} \quad w_1 \sim \frac{\alpha\Delta}{N^2}, \quad \phi_0 \sim \Delta H, \quad b_0 \sim \Delta. \tag{5.43}$$

This eliminates all dimensional factors and leaves the frontal evolution independent of any dimensionless parameters. In the SG case, we apply the equivalent scaling:

$$t \sim \alpha^{-1}, \quad x \sim \frac{NH}{f}, \quad z \sim H, \quad v_g \sim \frac{\Delta}{N}, \quad u \sim \frac{\alpha\Delta}{fN} \quad w \sim \frac{\alpha\Delta}{N^2}, \quad \phi \sim \Delta H, \quad b \sim \Delta. \tag{5.44}$$

The dimensionless SG equations depend on the parameter $\gamma \equiv \Delta/N^2H$, which multiplies the ageostrophic advection terms and also appears in the Jacobian of the coordinate transformation to geostrophic coordinates (see Appendix 5.7 for details). This parameter is the ratio between the buoyancy drop Δ across the front and the vertical buoyancy contrast N^2H. Equivalently, it measures the vertical excursion Δ/N^2 of isopycnals across the front relative to the domain height H (Fig. 5.2). In the following, we consider the case $\gamma = 1$ in detail and examine the γ dependence of the SG case in Section 5.5.1. From hereon, all quantities are understood to be nondimensionalized, and we omit decorations for simplicity.

5.4 Energy budget analysis

We now apply the energy diagnostics developed in the previous section to the frontal evolution at a time close to the collapse of the SG front ($t = 1.33$ for $\gamma = 1$, see Fig. 5.7a). We assess the importance of the various physical processes in the spectral energy budget and highlight the role of ageostrophic advection in transferring energy to small scales in the SG case. We then apply the coarse-graining approach to further investigate the spatial pattern of cross-scale energy transfer and exhibit the asymmetry of these transfers between the cyclonic and anticyclonic sides of the front.

5.4.1 Spectral kinetic energy budgets

he spectral kinetic energy budgets for QG and SG frontogenesis exhibit strong similarities (Fig. 5.3). Both cases show a transfer of energy from large to small spatial scales, as expected for a sharpening front, with the key difference that ageostrophic advection enhances this transfer in the SG case.

In the depth-integrated budget (Fig. 5.3a,c), buoyancy production serves as the source of kinetic energy and peaks at a wavenumber $k \sim 1$. Dense water sinks on the dense side of the front, and light water rises on the light side of the front (Fig. 5.2). Some of the kinetic energy thus produced is transferred from large to small scales by geostrophic and ageostrophic (in the SG case) advection. The geostrophic advection term is negative at large scales and positive at small scales, indicating a downscale transfer. The ageostrophic advection term has a similar pattern but shifted to smaller scales and with a smaller amplitude. Some of the kinetic energy generated by buoyancy production and transferred to smaller scales by advection leads to a strengthening of the frontal jet, as exhibited by the positive tendency, which peaks at noticeably smaller scales than the buoyancy production. Much of the kinetic energy production, however, is balanced by the sink term.

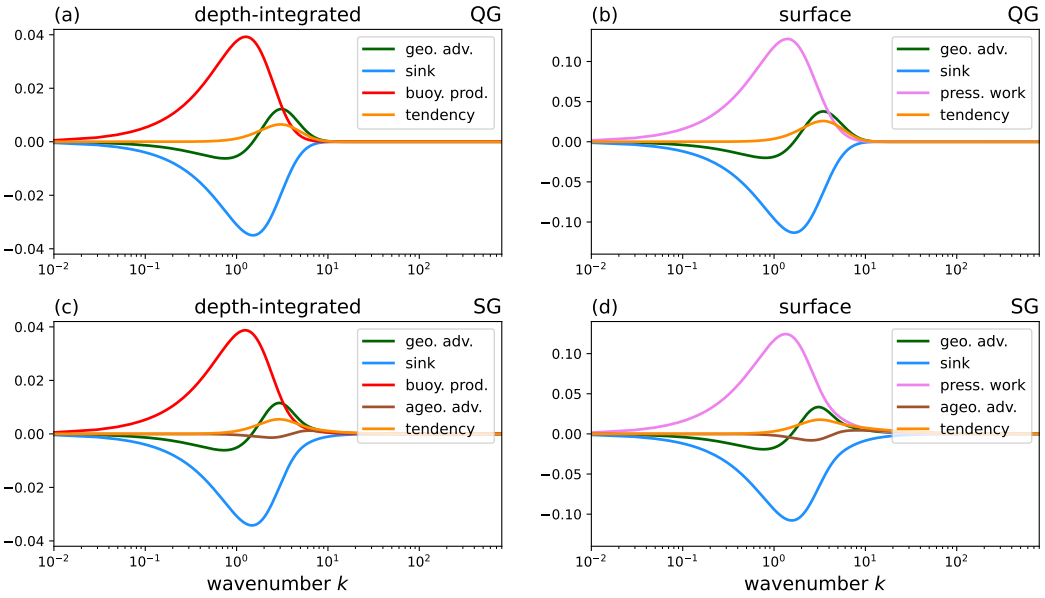

Figure 5.3: Spectral kinetic energy budget for the QG and SG fronts. The terms in (5.36) and (5.37) are shown with a sign convention as if all terms except the tendency were on the right-hand sides of these equations. The budgets are evaluated at $t = 1.33$, shortly before the collapse of the SG front. (a,c) Budgets integrated over the depth of the domain. (b,d) Budgets at the surface ($z = \frac{1}{2}$). All variables are dimensionless (see Appendix 5.7).

The budgets at the surface (Fig. 5.4b,d) mirror the depth-integrated budgets, except that pressure work takes the place of buoyancy production. At the surface, where $w = 0$, buoyancy production vanishes identically. Kinetic energy generated by buoyancy production in the interior is transported to the surface by pressure work.

To further illustrate the energy transfer to small scales and highlight the role of ageostrophic advection in the SG case, we calculate the spectra flux (5.38) of these two components at the surface (Fig. 5.4a,b). The geostrophic spectral flux is comparable between the QG and SG cases, with similar magnitudes and peaking at $k^{-1} = 0.61$ for QG and $k^{-1} = 0.64$ for SG. The ageostrophic spectral flux, present in SG only, peaks at a smaller scale ($k^{-1} = 0.22$) and dominates the scale transfer at small scales. This behavior is entirely expected, given that it is ageostrophic advection that accelerates frontogenesis in SG. It should be kept in mind, however, that the ageostrophic surface circulation is horizontally convergent on the cyclonic side of the front and divergent on the anticyclonic side (Fig. 5.2). The convergence on the cyclonic side collapses the front and causes downscale energy transfer, but the divergence on the anticyclonic side weakens the buoyancy gradient and broadens the front there. The downscale transfer of kinetic energy in the spectral budget is an integral over both regions, indicating that the downscale transfer caused by convergence on the cyclonic side dominates. The spectral transfer may mask substantial compensation between the distinct behaviors on the two sides of the front. We take this as motivation to next pursue a localized budget using the coarse-graining framework.

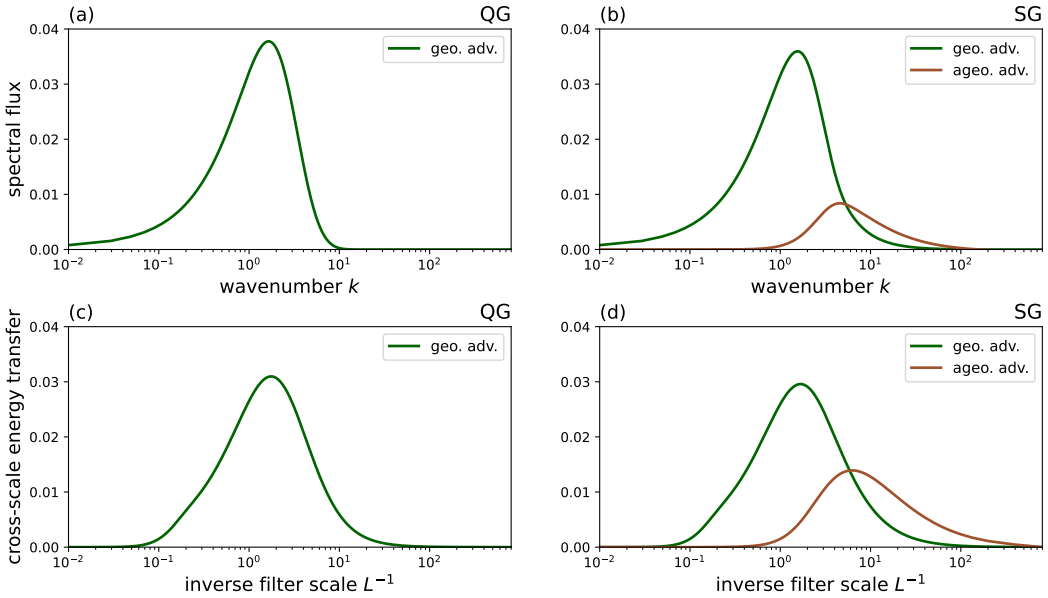

Figure 5.4: Integrated downscale kinetic energy transfer for the QG and SG fronts. Shown are the surface transfers calculated from the spectral budget (top) and the coarse-grained budget (bottom). For the SG case, the transfers are separated into geostrophic and ageostrophic contributions. All variables are dimensionless (see Appendix 5.7).

5.4.2 Coarse-grained kinetic energy budget

Although the spectral approach provides important information on the magnitude and sense of cross-scale energy transfer, it operates in wavenumber space and reflects spatially integrated behavior, giving no insight into the location of the energy transfer in physical space. To complement the spectral budget, we therefore apply the coarse-grained budgets (5.41) and (5.42) to the sharpening front, focusing as before on $\gamma = 1$ and $t = 1.33$, immediately before frontal collapse in the SG case.

The Gaussian filter employed here for coarse graining offers an optimal compromise between resolution in spectral and physical space. While it is less sharp in spectral space than the Fourier filter used in the spectral budget, it yields a spatially integrated scale transfer Π that is qualitatively similar to the spectral flux at the surface (Fig. 5.4c,d). The geostrophic scale transfer peaks at a filter scale $L = 0.57$ in QG and $L = 0.60$ in SG, similar to the respective inverse wavenumbers in the spectral budget. However, the geostrophic scale transfers are somewhat reduced in magnitude, and their peaks are broadened. The ageostrophic scale transfer in SG peaks at $L = 0.16$, and its peak magnitude is elevated compared to the spectral budget, giving the impression of a relatively more important contribution from ageostrophic advection to the total scale transfer than in the spectral fluxes. Despite the quantitative differences, the qualitative behavior is similar between these two descriptions of scale transfer. We next demonstrate the additional spatial information that the coarse-graining approach offers.

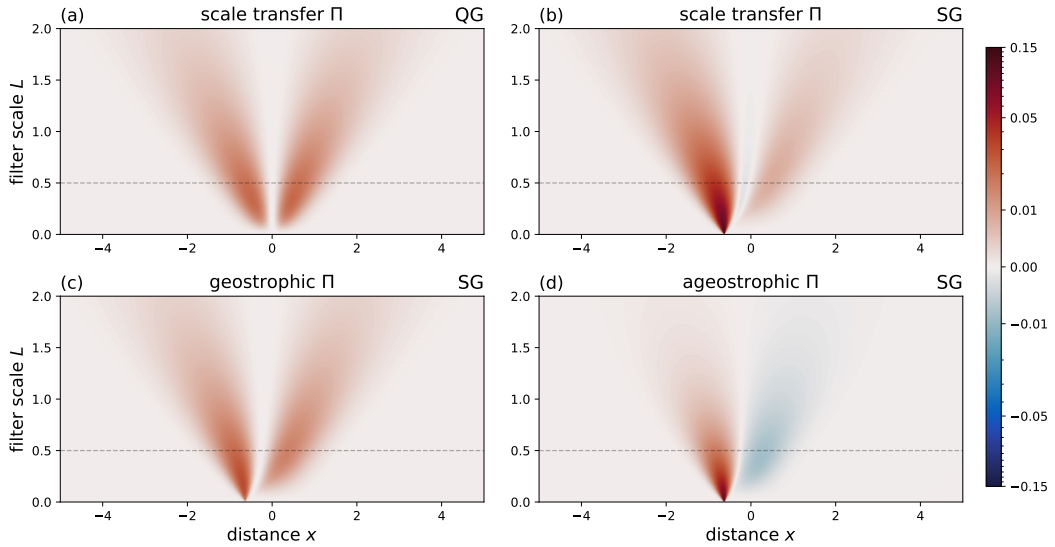

Figure 5.5: Cross-scale kinetic energy transfer Π from the coarse-grained budget. (a) Geostrophic scale transfer for the QG front. (b) Full scale transfer for the SG front. (c) Geostrophic contribution to the scale transfer for the SG front. (d) Ageostrophic contribution to the scale transfer for the SG front. The dashed line at $L = 0.5$ shows the filter scale used in Fig. 5.6. Note the arcsinh-scaled color map. All variables are dimensionless (see Appendix 5.7).

In physical space, the scale transfer shows distinct maxima on either side of the surface front, increasingly concentrated near the front with decreasing filter scales (Fig. 3.1a,b). This pattern is symmetric in QG because only the strain field sharpens the front through geostrophic advection. In SG, there is a marked asymmetry, with a much stronger downscale transfer on the cyclonic side of the front than on the anticyclonic side. This asymmetry arises because the front itself is asymmetric, so even geostrophic advection by the strain field produces an asymmetric pattern (Fig. 3.1c). More importantly, the ageostrophic scale transfer has opposite signs on the two sides of the front (Fig. 3.1d). Ageostrophic advection causes a downscale transfer on the cyclonic side and an upscale transfer on the anticyclonic side. This is expected because the ageostrophic circulation is horizontally convergent on the cyclonic side and divergent on the anticyclonic side (Fig. 5.2). On the anticyclonic side, while the downscale transfer caused by geostrophic advection dominates over the upscale transfer by ageostrophic advection, there is a substantial amount of cancellation, such that the overall downscale transfer is weakened substantially (Fig. 3.1b–d). On the cyclonic side, the ageostrophic downscale transfer is comparable to the geostrophic downscale transfer, and it dominates over the geostrophic one at sufficiently small filter scales (Fig. 3.1c,d).

The scale transfers and their spatial asymmetry in SG extend into the interior, as illustrated at the filter scale $L = 0.5$ (Fig. 5.6g,h). We note that, as exhibited in the spectral budget, the scale transfers are only part of the full kinetic energy budget, with a number of other terms exceeding their magnitudes (Fig. 5.6). In particular, buoyancy production from upwelling on the light, convergent side of the front and downwelling on the dense, divergent side is

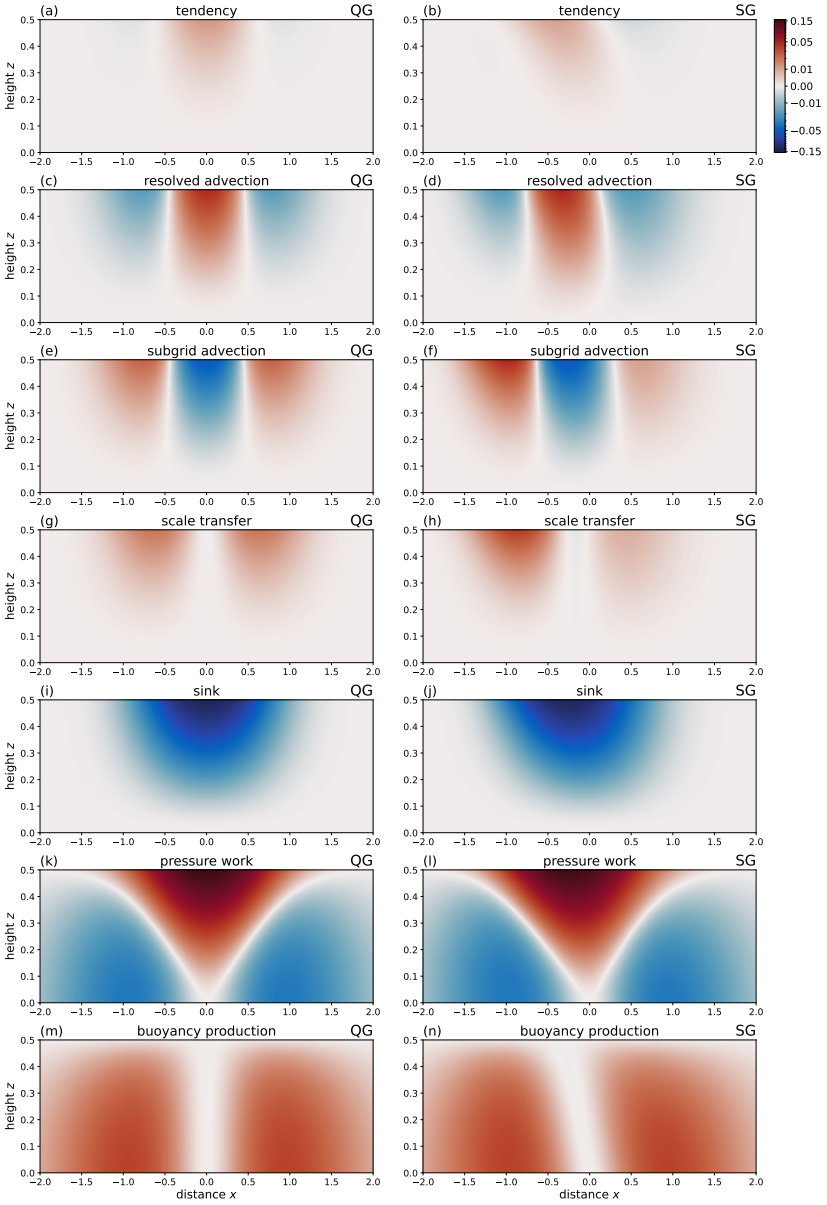

Figure 5.6: Coarse-grained kinetic energy budget for QG and SG fronts. The terms in (5.41) and (5.42) are shown with a sign convention as if all terms except the tendency (a,b) and cross-scale transfer (g,h) were on the right-hand sides of these equations. The budgets are evaluated at $t = 1.33$, with a spatial filter scale of $L = 0.5$. Note the arsinh-scaled color map. All variables are dimensionless (see Appendix 5.7).

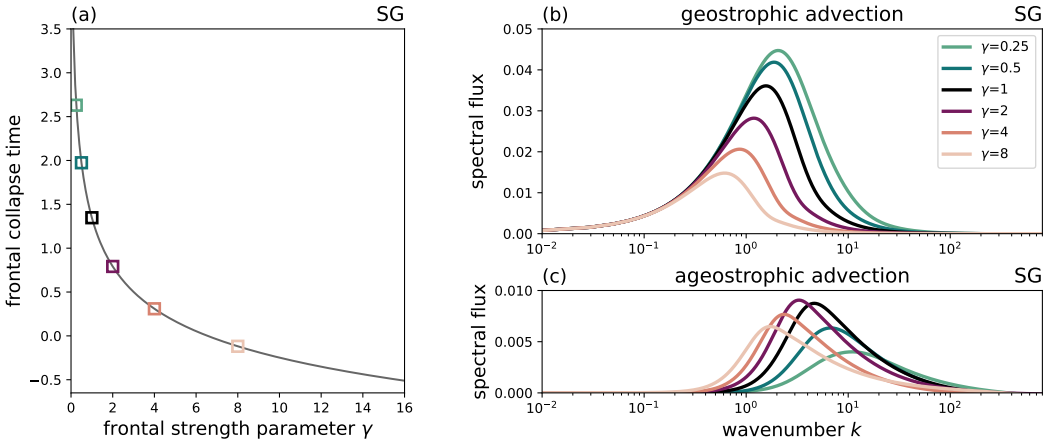

Figure 5.7: The impact of the frontal strength parameter γ on the SG frontal evolution. (a) Frontal collapse time as a function of γ. Colored boxes indicate γ values selected for comparison of energy transfer in (b,c). The reference case $\gamma = 1$, analyzed throughout the main text, is marked in black. (b) Surface spectral energy flux from geostrophic advection for selected values of γ shortly before the respective frontal collapse time. (c) Same as (b) but for ageostrophic advection. All variables are dimensionless (see Appendix 5.7).

the net source of kinetic energy (Fig. 5.6m,n). Pressure work concentrates the kinetic energy into the front (Fig. 5.6k,l), and the sink term from stretching and shear production offsets this gain of kinetic energy in the front (Fig. 5.6i,j). Resolved advective transport moves kinetic energy from the flanks to the center of the front (Fig. 5.6c,d), but its effect is strongly compensated by the subgrid transport (Fig. 5.6e,f). The result is a net advective transport from the anticyclonic to the cyclonic side in the SG case, and a weak residual in the QG case. The scale transfers should be interpreted in this context of the full kinetic energy budget.

5.5 Discussion

5.5.1 Dependence on frontal strength

While QG frontogenesis is independent of it, the evolution of an SG front depends on the frontal strength parameter $\gamma = \Delta/N^2H$, the ratio between the buoyancy drop across the front and the vertical buoyancy contrast (Fig. 5.7). So far, we have considered the $\gamma = 1$ case, but the surface ocean has fronts with varying strength. In winter, in particular, one might expect strong lateral buoyancy gradients, weak stratification, and deep mixed layers, so $\gamma > 1$. According to the observations compiled by Whalen and Drushka (2025), a typical front in the wintertime mixed layer may have $\Delta = 10^{-3}$ m s^{-2}, $N^2 = 4 \times 10^{-6}$ s^{-2}, and $H = 100$ m, which gives $\gamma = 2.5$. We therefore consider briefly how γ affects the scale transfer of energy in SG frontogenesis.

In the nondimensionalization of the SG equations, γ emerges naturally (see Section 5.3.6 and Appendix 5.7). While the SG equations in geostrophic coordinates are independent of γ, the coordinate transformation from geostrophic to physical coordinates does depend on it. The larger γ, the greater the distortion of the front and the faster the collapse. The collapse time

as a function of γ can be calculated by setting the Jacobian $\boldsymbol{J}$ of the transformation to zero, which provides the time at which the coordinate transformation ceases to be single-valued (Fig. 5.7a). We diagnose the spectral energy transfer at 0.01 dimensionless time units before the collapse time.

An increase in the frontal strength γ leads to a higher relative contribution from ageostrophic cross-scale energy fluxes to the total energy transfer (Fig. 5.7b,c). As γ increases from 0.25 to 8, the peak spectral flux due to geostrophic advection decreases monotonically. At $\gamma = 8$, the peak is reduced by 67% compared to the $\gamma = 0.25$ case. This decrease can be understood using the QG solution evaluated at the varying SG collapse times. The earlier collapse time for increasing γ mean that the QG front—and the SG front in geostrophic coordinates—is broader and weaker at the time of diagnosis, explaining the decrease of the peak flux and shift to larger scales. In contrast, the peak spectral flux due to ageostrophic advection increases with γ up to $\gamma = 2$, after which it decreases again. The ratio of the peak spectral fluxes due to ageostrophic and geostrophic advection increases monotonically from 9% at $\gamma = 0.25$ to 44% at $\gamma = 8$, highlighting the growing relative importance of ageostrophic dynamics in strong fronts. The qualitative nature of the spectral energy budget across this range of γ is similar to the $\gamma = 1$ case analyzed at length (Section 5.4).

5.5.2 Comparison with primitive equation models

The spatial structure of scale transfer kinetic energy in QG and SG frontogenesis diverges in some aspects from that in realistic primitive equation simulations (Srinivasan et al., 2023). The simple models of frontogenesis agree with the diagnosis of downscale energy transfer at fronts in primitive-equation models. As the front gets sharpened by the strain field as well as the ageostrophic secondary circulation, the frontal jet narrows, and energy is transferred to small scales (Fig. 5.3–5.6). In SG frontogenesis, the ageostrophic circulation by itself produces a dipole of energy transfer: a downscale transfer on the cyclonic side, where the ageostrophic circulation is horizontally convergent, and an upscale transfer on the anticyclonic side, where the ageostrophic circulation is horizontally divergent (Fig. 3.1d). This ageostrophic transfer is consistent with what is found in primitive-equation models (Fig. 5.1; Srinivasan et al., 2023). However, primitive-equation models exhibit a relatively stronger contribution to the overall scale transfer from the ageostrophic circulation. Srinivasan et al. (2023) found the ageostrophic transfer to dominate over geostrophic transfers, such that the ageostrophic upscale transfer overpowered geostrophic downscale transfer on the anticyclonic side of the front, leaving a dipole in the overall transfer and a tight correlation with the surface divergence (cf., Fig. 5.1).

We emphasize that our setup considers an isolated front, whereas realistic simulations produce fronts embedded in a turbulent mesoscale eddy field. While our setup helps isolate the processes causing energy transfer in a simple context, the energy exchange more broadly should involve mesoscale and submesoscale eddies. The sink term in our frontal setup should

be thought of as a stand-in for the interaction with the surrounding eddy field, which has confluent as well as diffluent regions. The sink term would be part of the scale transfer term for a spatially confined front, which may explain part of the differences with the primitive-equation model diagnostics. Perhaps more importantly, primitive-equation models parameterize mixed-layer turbulence, which affect the evolution of fronts and the strength of the ageostrophic circulation.

5.5.3 Mixed layer turbulence

A key idealization in our setup is that we study adiabatic and frictionless frontogenesis, neglecting the effects of mixed-layer turbulence. Like the sharpening of the front by the strain field, the mixing of momentum and buoyancy throws the front out of thermal wind balance and thus induces a secondary circulation that acts to restore it. The net effect of mixing can be either frontogenic or frontolytic, depending on the relative strengths of momentum and buoyancy mixing as well as on whether horizontal or vertical mixing dominates (Garrett and Loder, 1981; Thomas et al., 2008; McWilliams et al., 2015; Bodner et al., 2020; Dauhajre et al., 2025). If the parameterized mixing is frontogenic, as appears to be the case in the simulations of Srinivasan et al. (2023), a strengthened ageostrophic circulation will enhance the dipole of energy transfer due the convergence on the cyclonic side and divergence on the anticyclonic side of the front, and the resulting ageostrophic scale transfers can overpower the geostrophic transfer that dominates in the inviscid and adiabatic case. Parameterized mixed-layer turbulence may therefore be suspected to be the main reason for the heightened importance of ageostrophic advection in Srinivasan et al. (2023) compared to the idealized case studied here. Barkan et al. (2019) diagnosed a similar role of convergence in the sharpening of fronts from drifter data, and Torres et al. (2024) found a tell-tale correlation between convergence and downscale energy transfer in airborne observations of submesoscale fronts, suggesting that this effect is likely at play in the real ocean as well. Studying the impact of turbulent mixing on the energetics of frontogenesis in a controlled setup would help strengthen this interpretation of the simulated and observed phenomenology.

5.6 Conclusion

Frontogenesis as described by simple balanced theories produces a downscale transfer of kinetic energy (Fig. 5.4). A sharpening front is associated with a narrowing along-front jet and therefore a transfer of kinetic energy to small scales. A geostrophic strain field by itself produces such downscale transfer of kinetic energy, as described by the QG theory (Stone, 1966). Ageostrophic advection, included in the SG theory of frontogenesis (Hoskins and Bretherton, 1972), tilts over the front and accelerates frontogenesis. On the cyclonic side, the resulting horizontal convergence accelerates the sharpening of the buoyancy gradient and enhances the downscale transfer of kinetic energy (Fig. 3.1d). On the anticyclonic side, horizontal divergence slows the sharpening of the buoyancy gradient and is associated with

an upscale transfer of kinetic energy (Fig. 3.1d). In the net, ageostrophic advection enhances the kinetic energy transfer to small scales because the downscale transfer on the cyclonic side is stronger than the upscale transfer on the anticyclonic side (Fig. 3.1b,d).

The adiabatic and frictionless frontogenesis considered here displays a smaller ageostrophic contribution to the scale transfer of kinetic energy than realistic simulations and observations suggest (Fig. 5.1). In the idealized front, the dipole in the ageostrophic transfer—downscale on the cyclonic side of the front, upscale on the anticyclonic side—causes a distinct asymmetry in the overall transfer, but it is not strong enough to overpower the universally downscale geostrophic contribution to give a dipole in the overall transfer. This remains true over a wide range of frontal strengths (Fig. 5.7). We suspect that an enhancement of the ageostrophic circulation by non-conservative processes could flip this balance.

While the submesoscale scale transfer of kinetic energy has received heightened attention for its suspected importance as a route to dissipation (e.g., Capet et al., 2008c; Müller et al., 2011; Schubert et al., 2020; Naveira Garabato et al., 2022; Srinivasan et al., 2023), it is important to interpret this transfer in the context of the full kinetic energy budget. In the idealized theories of frontogenesis considered here, buoyancy production plays a major role in the energetics (Figs. 5.3, 5.6). The ageostrophic circulation lifts up light water and pushes down dense water as it slumps the front (Fig. 5.2). Pressure work transports the resulting kinetic energy into the surface front. The scale transfer moves some of this kinetic energy to smaller scales, playing an important role in the sharpening of the frontal jet. Equally important, however, is the sink of kinetic energy density due to the along-front stretching and shear production associated with the strain field. It would be interesting to extend this scale-resolved analysis of the full kinetic energy budget to more realistic simulations, in which the fronts are embedded in a turbulent eddy field.

Acknowledgments

We thank Andrew Thompson for valuable discussions on this work. YB acknowledges support from the National Aeronautics and Space Administration (NASA) Science Mission Directorate FINESST program under Award No. 80NSSC21K1635. JC acknowledges support from NASA under Award Nos. 80NSSC20K1140 and 80NSSC24K1652.

Data availability statement

Example scripts of QG and SG strain-driven frontal development and kinetic energy budget calculations in both physical and spectral space are available at: `https://doi.org/10.5281/zenodo.17102819`.

5.7 Appendix A: Nondimensionalization

Following the scaling stated in Section 5.3.6, we present the full nondimensionalized QG and SG kinetic energy equations, which serve as the basis for the spectral and coarse-grained

kinetic energy budget results in Section 5.4.

For the QG case, we follow standard procedure. Using the scales (5.43) in the QG kinetic energy equation (5.14), every term in the budget acquires a scale $\alpha\Delta^2/N^2$. The dimensionless form of this equation thus becomes independent of any parameters:

$$\frac{\partial}{\partial\breve{t}}\frac{\breve{v}_0^2}{2}+\frac{\partial}{\partial\breve{x}}\left(-\breve{x}\frac{\breve{v}_0^2}{2}+\breve{u}_1\breve{\phi}_0\right)+\frac{\partial}{\partial\breve{z}}\left(\breve{w}_1\breve{\phi}_0\right)+\frac{3}{2}\breve{v}_0^2=\breve{w}_1\breve{b}_0, \tag{5.45}$$

where $\breve{\cdot}$ marks the nondimensionalized quantities. Note that we dropped this decoration in the main text starting in Section 5.4.

The SG solution in geostrophic coordinates is identical to the QG solution in geostrophic coordinates and therefore also remains independent of any parameters. The coordinate transformation back to physical space, however, introduces the dimensionless parameter $\gamma = \Delta/N^2H$ that characterizes the frontal strength. The nondimensionalized coordinate transformation is

$$\breve{x}=\breve{X}-\gamma\breve{v}_g, \tag{5.46}$$

and its Jacobian is

$$\breve{J}=\left(1-\gamma\frac{\partial\breve{v}_g}{\partial\breve{X}}\right)^{-1}, \tag{5.47}$$

so the amount of distortion of the solution depends on the choice of γ. The modified geopotential is

$$\breve{\phi}=\breve{\Phi}-\gamma\frac{\breve{v}_g^2}{2}, \tag{5.48}$$

and the horizontal ageostrophic velocity becomes

$$\breve{u}=\breve{\tilde{u}}-\gamma\breve{w}\frac{\partial\breve{v}_g}{\partial\breve{z}}. \tag{5.49}$$

The parameter γ also appears in the nondimensionalized kinetic energy budget:

$$\frac{\partial}{\partial\breve{t}}\frac{\breve{v}_g^2}{2}+\frac{\partial}{\partial\breve{x}}\left[(-\breve{x}+\gamma\breve{u})\frac{\breve{v}_g^2}{2}+\breve{u}\breve{\phi}\right]+\frac{\partial}{\partial\breve{z}}\left[\gamma\breve{w}\frac{\breve{v}_g^2}{2}+\breve{w}\breve{\phi}\right]+\frac{3}{2}\breve{v}_g^2=\breve{w}\breve{b}. \tag{5.50}$$

As in the QG case, all terms share a dimensional scale $\alpha\Delta^2/N^2$, except for the ageostrophic advection of momentum by $\breve{u}$ and $\breve{w}$, which carry an additional factor of γ.

The nondimensionalized spectral and coarse-grained kinetic energy budgets are derived and diagnosed based on (5.45) and (5.50), following the steps laid out in Sections 5.3.4 and 5.3.5. In the spectral analysis, the wavenumber k is scaled with f/NH, the inverse of the characteristic length scale. In coarse-graining, the Gaussian filter scale L is the length scale at which the scale energy transfer is assessed, and is therefore nondimensionalized by NH/f, sharing the same scaling as the cross-front coordinate x.

Chapter 6

CONCLUSIONS AND FUTURE DIRECTIONS

6.1 Conclusions

The ocean is a quintessential component of the climate system, encompassing flows that span a wide range of spatial and temporal scales, each governed by distinct dynamics (e.g., Capet et al., 2008b). However, the ocean does not operate in isolation — it continuously interacts with the overlying atmosphere (Seo et al., 2016; Renault et al., 2016b) and exchanges energy, momentum, heat, carbon, and other tracers across its own scales (e.g., Su et al., 2018; Mahadevan, 2016). These interactions tie the climate system as a whole, enabling the transfer of properties and the redistribution of energy that drive the system's evolution. Among these scales, submesoscale motions have recently come into focus, owing to advances in numerical modeling and observational capabilities (Capet et al., 2008c; Callies et al., 2015; McWilliams, 2016). This thesis seeks to clarify the role of submesoscale dynamics in these critical climate interactions, with an emphasis on ocean–atmosphere coupling and energy transfer at submesoscale fronts.

We began by examining the joint impact of TFB and CFB on atmospheric winds in a numerical simulation that resolves submesoscale motions (Chapter 2). We showed that TFB and CFB interact constructively and destructively, producing submesoscale wind stress curl anomalies up to an order of magnitude larger than those at the mesoscale. Neglecting their combined influence can lead to inaccurate estimates of air–sea coupling strength and, consequently, errors in quantifying the impact of air–sea interactions on Ekman-driven vertical velocities (Gaube et al., 2015; Seo et al., 2016). We further showed that at submesoscale, nonlinear Ekman velocities dominate the Ekman pumping (Chapter 3). Decomposing the nonlinear velocities into contributions revealed that submesoscale surface vorticity gradients are the primary driver. These results highlight the importance of submesoscale motions in shaping air–sea interactions and modulating vertical transport in the surface ocean.

Besides facilitating air–sea interactions, submesoscale motions have received heightened attention for their role in mediating oceanic energy transfer across scales (Bodner et al., 2020). Yet debate persists over whether classic balanced theories, such as QG turbulence and QG or SG frontogenesis, can be applied (Torres et al., 2018; Barkan et al., 2019; Callies et al., 2015). We examined the temporal and spatial scales where submesoscale motions transition from balanced to unbalanced regimes (Chapter 4). Using submesoscale-resolving simulations and mooring observations, we found that, in a Lagrangian frame, they approach the unbalanced limit at $O(1)$ km, providing considerable scope for the applicability of balanced theories in the submesoscale range. In Chapter 5, we quantified spectral and coarse-grained

kinetic energy balance of an isolated submesoscale front under balanced QG and SG theories. Both frameworks produce forward energy transfer consistent with high-resolution numerical results (Srinivasan et al., 2023), especially with the ageostrophic circulation in SG frontogenesis reproducing the forward-inverse transfer dipole. However, ageostrophic circulation in balanced theories remains weak, and will likely be strengthened by mixed-layer turbulence (Dauhajre et al., 2025). These results highlight the potential for extending classic balanced theories interpret submesoscale motions, as they reproduce key features of frontal energy transfer.

6.2 Future Directions

Our current understanding of submesoscale turbulence and its contributions to the climate system largely stems from numerical studies. Due to their small spatial scales and short time spans (McWilliams, 2016), observational efforts of submesoscale motions have often been indirect (Callies et al., 2020) or confined to localized contexts (Yu et al., 2019; Naveira Garabato et al., 2022; Farrar et al., 2020, 2025). Large-scale and global assessments of submesoscale motions and their role in climate processes thus rely heavily on high-resolution global simulations (e.g., Sasaki et al., 2014; Su et al., 2018). Localized high-resolution modeling efforts (e.g., Capet et al., 2008b; Schubert et al., 2020; Srinivasan et al., 2023) have further unveiled important dynamical features and unique contributions of submesoscale motions. Yet, it remains an open question how insights from both global and localized numerical settings can best inform and constrain observational estimates of submesoscale variability and impacts.

Studies of submesoscale air–sea interactions have followed a similar trajectory. Numerical simulations have been used from examining individual thermal feedback (TFB) (Strobach et al., 2022) and current feedback (CFB) (Chen et al., 2022), to exploring their combined influence (Bai et al., 2023; Conejero et al., 2024), and to the present thesis chapters, which investigate how air–sea processes impact ocean surface vertical velocities. The reliance on numerical studies reflects the strict requirements for observational constraints: capturing air–sea interactions at submesoscale demands collocated and concurrent measurements of surface ocean currents and temperature, together with near-surface atmospheric winds, temperature, and stability. The small and fast nature of submesoscale motions further compound the challenge.

S-MODE, the Sub-Mesoscale Ocean Dynamics Experiment (Farrar et al., 2025), is a NASA field campaign designed to investigate how submesoscale ocean dynamics influence vertical transport in the upper ocean and air–sea processes. Although localized to a region in the California Current System, its comprehensive sampling strategy combines airborne surveys of the surface winds and ocean currents through DopplerScatt instrument (Wineteer et al., 2020) and SST from the Multiscale Observing System of the Ocean Surface platform (Farrar et al., 2025) up to $O(100)$ m effective resolution, providing the essential ingredients to

analyze submesoscale air–sea interactions in an observational setting. Initial analyses indicate that the joint TFB and CFB mechanism persists in observations; however, CFB tends to make the dominant relative contribution to variability in submesoscale wind stress curl anomalies. Vertical velocities associated with surface submesoscale features and air–sea interactions can be computed based on decompositions outlined in Chapter 3, and nonlinear Ekman velocities are expected to maintain their dominance in observational contexts due to strong surface vorticity and gradients of it (Torres et al., 2024).

Recently, observational efforts of small-scale ocean surface features have begun to extend to the global scale. SWOT, the Surface Water and Ocean Topography mission (Fu et al., 2024), is a joint NASA–CNES satellite mission designed to sample sea surface currents through sea surface height with unprecedented spatial resolution, enabling the study of ocean surface processes down to $O(10)$–$O(20)$ km scales. However, its temporal sampling, constrained by a 21-day repeat cycle, may limit the ability to resolve the continuous evolution of submesoscale flows. Nevertheless, combining SWOT-derived surface current and wind speed measurements with available SST and wind observations from scatterometry (e.g., Verhoef et al., 2012) offers new opportunities to investigate air–sea interactions over broad regions. The availability of SWOT would be particularly valuable in remote and data-sparse regions like the Southern Ocean, where shipboard and observational campaigns are logistically challenging (Josey et al., 2023).

The numerical insights on air–sea interaction processes and impacts developed in this thesis represent key steps toward improving our quantification of air–sea interactions and the contributions of surface submesoscale dynamics. The results underscore the critical role of submesoscale processes in shaping upper-ocean variability and, it is hoped, will help identify the essential dynamics to capture in future observational efforts and thereby advancing our understanding of the role of submesoscale dynamics in the climate system.

References

Aluie, H., M. Hecht, and G. K. Vallis, 2018: Mapping the energy cascade in the north atlantic ocean: The coarse-graining approach. *Journal of Physical Oceanography*, **48 (2)**, 225–244.

Arbic, B. K., M. Müller, J. G. Richman, J. F. Shriver, A. J. Morten, R. B. Scott, G. Sérazin, and T. Penduff, 2014: Geostrophic turbulence in the frequency–wavenumber domain: Eddy-driven low-frequency variability. *Journal of Physical Oceanography*, **44 (8)**, 2050–2069.

Arbic, B. K., K. L. Polzin, R. B. Scott, J. G. Richman, and J. F. Shriver, 2013: On eddy viscosity, energy cascades, and the horizontal resolution of gridded satellite altimeter products. *Journal of Physical Oceanography*, **43 (2)**, 283–300, doi:10.1175/JPO-D-11-0240.1.

Arbic, B. K., S. Elipot, J. M. Brasch, D. Menemenlis, A. L. Ponte, J. F. Shriver, X. Yu, E. D. Zaron, M. H. Alford, M. C. Buijsman, R. Abernathey, D. Garcia, L. Guan, P. E. Martin, and A. D. Nelson, 2022: Near-surface oceanic kinetic energy distributions from drifter observations and numerical models. *Journal of Geophysical Research: Oceans*, **127 (10)**, e2022JC018 551.

Asselin, O., and W. R. Young, 2020: Penetration of wind-generated near-inertial waves into a turbulent ocean. *Journal of Physical Oceanography*, **50 (6)**, 1699–1716, doi:10.1175/JPO-D-19-0319.1.

Badin, G., 2013: Surface semi-geostrophic dynamics in the ocean. *Geophysical & Astrophysical Fluid Dynamics*, **107 (5)**, 526–540.

Bai, Y., A. F. Thompson, A. B. Villas Bôas, P. Klein, H. S. Torres, and D. Menemenlis, 2023: Sub-mesoscale wind-front interactions: The combined impact of thermal and current feedback. *Geophysical Research Letters*, **50 (18)**, e2023GL104 807.

Balwada, D., K. S. Smith, and R. Abernathey, 2018: Submesoscale vertical velocities enhance tracer subduction in an idealized Antarctic Circumpolar Current. *Geophysical Research Letters*, **45 (18)**, 9790–9802.

Balwada, D., Q. Xiao, S. Smith, R. Abernathey, and A. R. Gray, 2021: Vertical fluxes conditioned on vorticity and strain reveal submesoscale ventilation. *Journal of Physical Oceanography*, **51 (9)**, 2883–2901.

Barkan, R., M. J. Molemaker, K. Srinivasan, J. C. McWilliams, and E. A. D'Asaro, 2019: The role of horizontal divergence in submesoscale frontogenesis. *Journal of Physical Oceanography*, **49 (6)**, 1593–1618.

Blumen, W., 1978-: Uniform potential vorticity flow: Part I. Theory of wave interactions and two-dimensional turbulence. *Journal of the Atmospheric Sciences*, **35 (5)**, 774–783, doi:10.1175/1520-0469(1978)035<0774:UPVFPI>2.0.CO;2.

Boccaletti, G., R. Ferrari, and B. Fox-Kemper, 2007: Mixed layer instabilities and restratification. *Journal of Physical Oceanography*, **37 (9)**, 2228–2250.

Bodner, A. S., B. Fox-Kemper, L. P. Van Roekel, J. C. McWilliams, and P. P. Sullivan, 2020: A perturbation approach to understanding the effects of turbulence on frontogenesis. *Journal of Fluid Mechanics*, **883**, A25.

Buckingham, C. E., A. C. Naveira Garabato, A. F. Thompson, L. Brannigan, A. Lazar, D. P. Marshall, A. George Nurser, G. Damerell, K. J. Heywood, and S. E. Belcher, 2016: Seasonality of submesoscale flows in the ocean surface boundary layer. *Geophysical Research Letters*, **43 (5)**, 2118–2126.

Bye, J. A., 1985: Large-scale momentum exchange in the coupled atmosphere-ocean. *Elsevier Oceanography Series*, Vol. 40, Elsevier, 51–61.

Callies, J., R. Barkan, and A. Naveira Garabato, 2020: Time scales of submesoscale flow inferred from a mooring array. *Journal of Physical Oceanography*, **50 (4)**, 1065–1086.

Callies, J., and R. Ferrari, 2018: Baroclinic instability in the presence of convection. *Journal of Physical Oceanography*, **48 (1)**, 45–60.

Callies, J., R. Ferrari, J. M. Klymak, and J. Gula, 2015: Seasonality in submesoscale turbulence. *Nature Communications*, **6 (1)**, 6862.

Callies, J., G. Flierl, R. Ferrari, and B. Fox-Kemper, 2016: The role of mixed-layer instabilities in submesoscale turbulence. *Journal of Fluid Mechanics*, **788**, 5–41.

Capet, X., P. Klein, B. L. Hua, G. Lapeyre, and J. C. McWilliams, 2008a: Surface kinetic energy transfer in surface quasi-geostrophic flows. *Journal of Fluid Mechanics*, **604**, 165–174, doi:10.1017/S0022112008001110.

Capet, X., J. C. McWilliams, M. J. Molemaker, and A. F. Shchepetkin, 2008b: Mesoscale to submesoscale transition in the California current system. Part I: Flow structure, eddy flux, and observational tests. *Journal of Physical Oceanography*, **38 (1)**, 29–43.

Capet, X., J. C. McWilliams, M. J. Molemaker, and A. F. Shchepetkin, 2008c: Mesoscale to submesoscale transition in the California current system. Part III: Energy balance and flux. *Journal of Physical Oceanography*, **38 (10)**, 2256–2269.

Carson, R., 1962: *Silent Spring*. Houghton Mifflin, Boston.

Chang, P., S. Zhang, G. Danabasoglu, S. G. Yeager, H. Fu, H. Wang, F. S. Castruccio, Y. Chen, J. Edwards, and L. Fu, Dan andWu, 2020: An unprecedented set of high-resolution earth system simulations for understanding multiscale interactions in climate variability and change. *Journal of Advances in Modeling Earth Systems*, **12 (12)**, e2020MS002 298.

Charney, J. G., 1971: Geostrophic turbulence. *Journal of the Atmospheric Sciences*, **28 (6)**, 1087–1095.

Chavez, F. P., and M. Messié, 2009: A comparison of eastern boundary upwelling ecosystems. *Progress in Oceanography*, **83 (1-4)**, 80–96.

Checkley Jr, D. M., and J. A. Barth, 2009: Patterns and processes in the California current system. *Progress in Oceanography*, **83 (1-4)**, 49–64.

Chelton, D. B., P. Gaube, M. G. Schlax, J. J. Early, and R. M. Samelson, 2011a: The influence of nonlinear mesoscale eddies on near-surface oceanic chlorophyll. *Science*, **334 (6054)**, 328–332.

Chelton, D. B., M. G. Schlax, M. H. Freilich, and R. F. Milliff, 2004: Satellite measurements reveal persistent small-scale features in ocean winds. *Science*, **303 (5660)**, 978–983.

Chelton, D. B., M. G. Schlax, and R. M. Samelson, 2007: Summertime coupling between sea surface temperature and wind stress in the California current system. *Journal of Physical Oceanography*, **37 (3)**, 495–517.

Chelton, D. B., M. G. Schlax, and R. M. Samelson, 2011b: Global observations of nonlinear mesoscale eddies. *Progress in Oceanography*, **91 (2)**, 167–216.

Chelton, D. B., and S.-P. Xie, 2010: Coupled ocean-atmosphere interaction at oceanic mesoscales. *Oceanography*, **23 (4)**, 52–69.

Chelton, D. B., S. K. Esbensen, M. G. Schlax, N. Thum, M. H. Freilich, F. J. Wentz, C. L. Gentemann, M. J. McPhaden, and P. S. Schopf, 2001: Observations of coupling between surface wind stress and sea surface temperature in the eastern tropical Pacific. *Journal of Climate*, **14 (7)**, 1479–1498.

Chen, X., W. Dewar, E. Chassignet, M. Bourassa, S. Morey, and G. Gopalakrishnan, 2022: On the feedback between air-sea turbulent momentum flux and oceanic submesoscale processes. *Journal of Geophysical Research: Oceans*, **127 (10)**, e2022JC018 767.

Chereskin, T., 1995: Direct evidence for an Ekman balance in the California current. *Journal of Geophysical Research: Oceans*, **100 (C9)**, 18 261–18 269.

Choi, J., A. Bracco, R. Barkan, A. F. Shchepetkin, J. C. McWilliams, and J. M. Molemaker, 2017: Submesoscale dynamics in the northern Gulf of Mexico. Part III: Lagrangian implications. *Journal of Physical Oceanography*, **47 (9)**, 2361–2376.

Combes, V., F. Chenillat, E. Di Lorenzo, P. Rivière, M. D. Ohman, and S. J. Bograd, 2013: Cross-shore transport variability in the California current: Ekman upwelling vs. eddy dynamics. *Progress in Oceanography*, **109**, 78–89.

Conejero, C., L. Renault, F. Desbiolles, J. McWilliams, and H. Giordani, 2024: Near-surface atmospheric response to meso-and submesoscale current and thermal feedbacks. *Journal of Physical Oceanography*, **54 (3)**, 823–848.

Conn, S., J. Fitzgerald, and J. Callies, 2024: Interpreting observed interactions between near-inertial waves and mesoscale eddies. *Journal of Physical Oceanography*, **54 (2)**, 485–502.

Crowe, M. N., and J. R. Taylor, 2018: The evolution of a front in turbulent thermal wind balance. Part 1. Theory. *Journal of Fluid Mechanics*, **850**, 179–211.

Crowe, M. N., and J. R. Taylor, 2019: Baroclinic instability with a simple model for vertical mixing. *Journal of Physical Oceanography*, **49 (12)**, 3273–3300.

Cullen, V., 2005: *Down to the sea for science: 75 years of ocean research, education, and exploration at the Woods Hole Oceanographic Institution*. Woods Hole Oceanographic Insitution.

Dauhajre, D. P., K. Srinivasan, M. J. Molemaker, J. Gula, D. Hypolite, J. C. McWilliams, R. Barkan, and W. R. Young, 2025: Vertical mixing can both induce and inhibit submesoscale frontogenesis. *Journal of Physical Oceanography*.

Desbiolles, F., A. N. Meroni, L. Renault, and C. Pasquero, 2023: Environmental control of wind response to sea surface temperature patterns in reanalysis dataset. *Journal of Climate*, 1–31.

Dewar, W. K., and G. R. Flierl, 1987: Some effects of the wind on rings. *Journal of Physical Oceanography*, **17 (10)**, 1653–1667, doi:10.1175/1520-0485(1987)017<1653:SEOTWO>2.0.CO;2.

Dong, S., J. Sprintall, S. T. Gille, and L. Talley, 2008: Southern Ocean mixed-layer depth from Argo float profiles. *Journal of Geophysical Research: Oceans*, **113 (C6)**.

Dove, L. A., D. Balwada, A. F. Thompson, and A. R. Gray, 2022: Enhanced ventilation in energetic regions of the Antarctic Circumpolar Current. *Geophysical Research Letters*, **49 (13)**, e2021GL097 574.

Dove, L. A., A. F. Thompson, D. Balwada, and A. R. Gray, 2021: Observational evidence of ventilation hotspots in the Southern Ocean. *Journal of Geophysical Research: Oceans*, **126 (7)**, e2021JC017 178.

Dove, L. A., G. A. Viglione, A. F. Thompson, M. M. Flexas, T. R. Cason, and J. Sprintall, 2023: Controls on wintertime ventilation in southern Drake Passage. *Geophysical Research Letters*, **50 (5)**, e2022GL102 550.

Duhaut, T. H., and D. N. Straub, 2006: Wind stress dependence on ocean surface velocity: Implications for mechanical energy input to ocean circulation. *Journal of Physical Oceanography*, **36 (2)**, 202–211.

D'Asaro, E. A., A. Y. Shcherbina, J. M. Klymak, J. Molemaker, G. Novelli, C. M. Guigand, A. C. Haza, B. K. Haus, E. H. Ryan, G. A. Jacobs, H. S. Huntley, N. J. M. Laxague, S. Chen, F. Judt, J. C. McWilliams, R. Barkan, A. D. Kirwan, A. C. Poje, and T. M. Özgökmen, 2018: Ocean convergence and the dispersion of flotsam. *Proceedings of the National Academy of Sciences*, **115 (6)**, 1162–1167.

Eden, C., and H. Dietze, 2009: Effects of mesoscale eddy/wind interactions on biological new production and eddy kinetic energy. *Journal of Geophysical Research: Oceans*, **114 (C5)**.

Ekman, V. W., 1905: On the influence of the earth's rotation on ocean-currents. *Arkiv fr Matematik, Astronomy Och Fysik*.

Elipot, S., R. Lumpkin, R. C. Perez, J. M. Lilly, J. J. Early, and A. M. Sykulski, 2016: A global surface drifter data set at hourly resolution. *Journal of Geophysical Research: Oceans*, **121 (5)**, 2937–2966.

Erickson, Z. K., A. F. Thompson, J. Callies, X. Yu, A. Naveira Garabato, and P. Klein, 2020: The vertical structure of open-ocean submesoscale variability during a full seasonal cycle. *Journal of Physical Oceanography*, **50 (1)**, 145–160.

Eyink, G. L., 1995: Local energy flux and the refined similarity hypothesis. *Journal of Statistical Physics*, **78 (1)**, 335–351, doi:10.1007/BF02183352.

Farrar, J. T., E. D'Asaro, E. Rodriguez, A. Shcherbina, E. Czech, P. Matthias, S. Nicholas, F. Bingham, A. Mahedevan, M. Omand, and R. Jenkins, 2020: S-mode: The sub-mesoscale ocean dynamics experiment. *IGARSS 2020-2020 IEEE International Geoscience and Remote Sensing Symposium*, IEEE, 3533–3536.

Farrar, J. T., E. D'Asaro, E. Rodriguez, A. Shcherbina, L. Lenain, M. Omand, A. Wineteer, P. Bhuyan, F. Bingham, A. Villas Boas, and Coauthors, 2025: S-mode: The sub-mesoscale ocean dynamics experiment. *Bulletin of the American Meteorological Society*, **106 (4)**, E657–E677.

Ferrari, R., and C. Wunsch, 2009: Ocean circulation kinetic energy: Reservoirs, sources, and sinks. *Annual Review of Fluid Mechanics*, **41 (1)**, 253–282.

Flexas, M. M., A. F. Thompson, H. S. Torres, P. Klein, J. T. Farrar, H. Zhang, and D. Menemenlis, 2019: Global estimates of the energy transfer from the wind to the ocean, with emphasis on near-inertial oscillations. *Journal of Geophysical Research: Oceans*, **124 (8)**, 5723–5746.

Forget, G., J.-M. Campin, P. Heimbach, C. Hill, R. Ponte, and C. Wunsch, 2015: ECCO version 4: An integrated framework for non-linear inverse modeling and global ocean state estimation. *Geoscientific Model Development*, **8 (10)**, 3071–3104.

Foussard, A., G. Lapeyre, and R. Plougonven, 2019: Storm track response to oceanic eddies in idealized atmospheric simulations. *Journal of Climate*, **32 (2)**, 445–463.

Fox-Kemper, B., R. Ferrari, and R. Hallberg, 2008: Parameterization of mixed layer eddies. Part I: Theory and diagnosis. *Journal of Physical Oceanography*, **38 (6)**, 1145–1165, doi:10.1175/2007JPO3792.1.

Fox-Kemper, B., H. Hewitt, C. Xiao, G. Aðalgeirsdóttir, S. Drijfhout, T. Edwards, N. Golledge, M. Hemer, R. Kopp, G. Krinner, A. Mix, D. Notz, S. Nowicki, I. Nurhati, L. Ruiz, J.-B. Sallée, A. Slangen, and Y. Yu, 2021: Ocean, Cryosphere and Sea Level Change. *Climate Change 2021: The Physical Science Basis. Contribution of Working Group I to the Sixth Assessment Report of the Intergovernmental Panel on Climate Change*, V. Masson-Delmotte, P. Zhai, A. Pirani, S. Connors, C. Péan, S. Berger, N. Caud, Y. Chen, L. Goldfarb, M. Gomis, M. Huang, K. Leitzell, E. Lonnoy, J. Matthews, T. Maycock, T. Waterfield, O. Yelekçi, R. Yu, and B. Zhou, Eds., Cambridge University Press, Cambridge, United Kingdom and New York, NY, USA, 1211–1362.

Frenger, I., N. Gruber, R. Knutti, and M. Münnich, 2013: Imprint of Southern Ocean eddies on winds, clouds and rainfall. *Nature Geoscience*, **6 (8)**, 608–612.

Fu, L.-L., T. M. Pavelsky, J.-F. Crétaux, R. Morrow, J. T. Farrar, P. Vaze, P. Sengenès, N. Vinogradova-Shiffer, A. Sylvestre-Baron, N. Picot, and G. Dibarboure, 2024: The surface water and ocean topography mission: A breakthrough in radar remote sensing of the ocean and land surface water. *Geophysical Research Letters*, **51 (4)**, e2023GL107 652, doi:10.1029/2023GL107652.

Fuglister, F. C., and L. Worthington, 1951: Some results of a multiple ship survey of the Gulf Stream. *Tellus*, **3 (1)**, 1–14.

Garrett, C. J. R., and J. Loder, 1981: Dynamical aspects of shallow sea fronts. *Philosophical Transactions of the Royal Society of London. Series A, Mathematical and Physical Sciences*, **302 (1472)**, 563–581.

Gaube, P., D. B. Chelton, R. M. Samelson, M. G. Schlax, and L. W. O'Neill, 2015: Satellite observations of mesoscale eddy-induced Ekman pumping. *Journal of Physical Oceanography*, **45 (1)**, 104–132.

Gaube, P., D. B. Chelton, P. G. Strutton, and M. J. Behrenfeld, 2013: Satellite observations of chlorophyll, phytoplankton biomass, and Ekman pumping in nonlinear mesoscale eddies. *Journal of Geophysical Research: Oceans*, **118 (12)**, 6349–6370.

Gaube, P., C. Chickadel, R. Branch, and A. Jessup, 2019: Satellite observations of SST-induced wind speed perturbation at the oceanic submesoscale. *Geophysical Research Letters*, **46 (5)**, 2690–2695.

Gregg, M. C., 1989: Scaling turbulent dissipation in the thermocline. *Journal of Geophysical Research: Oceans*, **94 (C7)**, 9686–9698.

Gruber, N., P. Landschützer, and N. S. Lovenduski, 2019: The variable Southern Ocean carbon sink. *Annual Review of Marine Science*, **11**, 159–186.

Gula, J., M. J. Molemaker, and J. C. McWilliams, 2014: Submesoscale cold filaments in the Gulf Stream. *Journal of Physical Oceanography*, **44 (10)**, 2617–2643.

Haine, T. W. N., and J. Marshall, 1998: Gravitational, symmetric, and baroclinic instability of the ocean mixed layer. *Journal of Physical Oceanography*, **28 (4)**, 634–658, doi:10.1175/1520-0485(1998)028<0634:GSABIO>2.0.CO;2.

Hausmann, U., and A. Czaja, 2012: The observed signature of mesoscale eddies in sea surface temperature and the associated heat transport. *Deep Sea Research Part I: Oceanographic Research Papers*, **70**, 60–72.

Hayes, S. P., M. J. McPhaden, and J. M. Wallace, 1989: The influence of sea-surface temperature on surface wind in the eastern equatorial Pacific: Weekly to monthly variability. *Journal of Climate*, **2 (12)**, 1500–1506.

He, Q., H. Zhan, S. Cai, and G. Zha, 2016: On the asymmetry of eddy-induced surface chlorophyll anomalies in the Southeastern Pacific: The role of eddy-Ekman pumping. *Progress in Oceanography*, **141**, 202–211.

He, Q., H. Zhan, Y. Shuai, S. Cai, Q. P. Li, G. Huang, and J. Li, 2017: Phytoplankton bloom triggered by an anticyclonic eddy: The combined effect of eddy Ekman pumping and winter mixing. *Journal of Geophysical Research: Oceans*, **122 (6)**, 4886–4901.

Held, I. M., R. T. Pierrehumbert, S. T. Garner, and K. L. Swanson, 1995: Surface quasi-geostrophic dynamics. *Journal of Fluid Mechanics*, **282**, 1–20, doi:10.1017/S0022112095000012.

Hoskins, B. J., 1975: The geostrophic momentum approximation and the semi-geostrophic equations. *Journal of Atmospheric Sciences*, **32 (2)**, 233–242.

Hoskins, B. J., and F. P. Bretherton, 1972: Atmospheric frontogenesis models: Mathematical formulation and solution. *Journal of Atmospheric Sciences*, **29 (1)**, 1–37.

Hoskins, B. J., and I. Draghici, 1977: The forcing of ageostrophic motion according to the semi-geostrophic equations and in an isentropic coordinate model. *Journal of Atmospheric Sciences*, **34 (12)**, 1859–1867.

Hoskins, B. J., I. Draghici, and H. Davies, 1978: A new look at the ω-equation. *Quarterly Journal of the Royal Meteorological Society*, **104 (439)**, 31–38.

Hoskins, B. J., M. E. McIntyre, and A. W. Robertson, 1985: On the use and significance of isentropic potential vorticity maps. *Quarterly Journal of the Royal Meteorological Society*, **111 (470)**, 877–946.

Jones, C. S., Q. Xiao, R. P. Abernathey, and K. S. Smith, 2023: Using lagrangian filtering to remove waves from the ocean surface velocity field. *Journal of Advances in Modeling Earth Systems*, **15 (4)**, e2022MS003 220.

Josey, S. A., J. P. Grist, J. V. Mecking, B. I. Moat, and E. Schulz, 2023: A clearer view of Southern Ocean air–sea interaction using surface heat flux asymmetry. *Philosophical Transactions of the Royal Society A*, **381 (2249)**, 20220 067.

Kraichnan, R. H., 1967: Inertial ranges in two-dimensional turbulence. *Physics of Fluids*, **10 (7)**, 1417–1423.

Lapeyre, G., and P. Klein, 2006: Dynamics of the upper oceanic layers in terms of surface quasigeostrophy theory. *Journal of Physical Oceanography*, **36 (2)**, 165–176.

Lawrence, A., and J. Callies, 2022: Seasonality and spatial dependence of mesoscale and submesoscale ocean currents from along-track satellite altimetry. *Journal of Physical Oceanography*, **52 (9)**, 2069–2089.

Leonard, A., 1975: Energy cascade in large-eddy simulations of turbulent fluid flows. *Advances in Geophysics*, F. N. Frenkiel, and R. E. Munn, Eds., Turbulent Diffusion in Environmental Pollution, Vol. 18, Elsevier, 237–248.

Li, D., P. Chang, S. Ramachandran, Z. Jing, Q. Zhang, J. Kurian, A. Gopal, and H. Yang, 2021: Contribution of the two types of Ekman pumping induced eddy heat flux to the total vertical eddy heat flux. *Geophysical Research Letters*, **48 (9)**, e2021GL092 982.

Li, X., W. Pichel, E. Maturi, P. Clemente-Colon, and J. Sapper, 2001: Deriving the operational nonlinear multichannel sea surface temperature algorithm coefficients for NOAA-15 avhrr/3. *International Journal of Remote Sensing*, **22 (4)**, 699–704.

Liu, T. W., X. Xie, P. S. Polito, S.-P. Xie, and H. Hashizume, 2000: Atmospheric manifestation of tropical instability wave observed by QuikScat and Tropical Rain Measuring Mission. *Geophysical Research Letters*, **27 (16)**, 2545–2548.

Luecke, C., B. Arbic, S. Bassette, J. Richman, J. Shriver, M. Alford, O. Smedstad, P. Timko, D. Trossman, and A. Wallcraft, 2017: The global mesoscale eddy available potential energy field in models and observations. *Journal of Geophysical Research: Oceans*, **122 (11)**, 9126–9143.

Mahadevan, A., 2016: The impact of submesoscale physics on primary productivity of plankton. *Annual Review of Marine Science*, **8**, 161–184.

Mahadevan, A., and A. Tandon, 2006: An analysis of mechanisms for submesoscale vertical motion at ocean fronts. *Ocean Modelling*, **14 (3-4)**, 241–256.

Mantua, N. J., S. R. Hare, Y. Zhang, J. M. Wallace, and R. C. Francis, 1997: A Pacific interdecadal climate oscillation with impacts on salmon production. *Bulletin of the American Meteorological Society*, **78 (6)**, 1069–1080.

Marshall, J., A. Adcroft, C. Hill, L. Perelman, and C. Heisey, 1997: A finite-volume, incompressible Navier Stokes model for studies of the ocean on parallel computers. *Journal of Geophysical Research: Oceans*, **102 (C3)**, 5753–5766, doi:10.1029/96JC02775, URL https://onlinelibrary.wiley.com/doi/abs/10.1029/96JC02775, _eprint: https://onlinelibrary.wiley.com/doi/pdf/10.1029/96JC02775.

Marshall, J., and K. Speer, 2012: Closure of the meridional overturning circulation through Southern Ocean upwelling. *Nature Geoscience*, **5 (3)**, 171–180.

McGillicuddy, D. J., L. A. Anderson, N. R. Bates, T. Bibby, K. O. Buesseler, C. A. Carlson, C. S. Davis, C. Ewart, P. G. Falkowski, S. A. Goldthwait, and Coauthors, 2007: Eddy-wind interactions stimulate extraordinary mid-ocean plankton blooms. *Science*, **316 (5827)**, 1021–1026.

McWilliams, J. C., 2016: Submesoscale currents in the ocean. *Proceedings of the Royal Society A: Mathematical, Physical and Engineering Sciences*, **472 (2189)**, 20160 117.

McWilliams, J. C., J. Gula, M. J. Molemaker, L. Renault, and A. F. Shchepetkin, 2015: Filament frontogenesis by boundary layer turbulence. *Journal of Physical Oceanography*, **45 (8)**, 1988–2005.

Mensa, J. A., Z. Garraffo, A. Griffa, T. M. Özgökmen, A. Haza, and M. Veneziani, 2013: Seasonality of the submesoscale dynamics in the Gulf Stream region. *Ocean Dynamics*, **63 (8)**, 923–941, doi:10.1007/s10236-013-0633-1.

Morrison, A. K., D. W. Waugh, A. M. Hogg, D. C. Jones, and R. P. Abernathey, 2022: Ventilation of the Southern Ocean pycnocline. *Annual Review of Marine Science*, **14**, 405–430.

Müller, P., J. McWilliams, and J. Molemaker, 2011: Routes to dissipation in the ocean: The 2D/3D turbulence conundrum. *Marine Turbulence: Theories, Observations, and Models*, Cambridge University Press.

Nagai, T., A. Tandon, E. Kunze, and A. Mahadevan, 2015: Spontaneous generation of near-inertial waves by the Kuroshio Front. *Journal of Physical Oceanography*, **45 (9)**, 2381–2406.

Naveira Garabato, A., X. Yu, J. Callies, R. Barkan, K. L. Polzin, E. E. Frajka-Williams, C. E. Buckingham, and S. M. Griffies, 2022: Kinetic energy transfers between mesoscale and submesoscale motions in the open ocean's upper layers. *Journal of Physical Oceanography*, **52 (1)**, 75–97, doi:10.1175/JPO-D-21-0099.1.

Nicholson, S. A., D. B. Whitt, I. Fer, M. D. du Plessis, A. D. Lebéhot, S. Swart, A. J. Sutton, and P. M. Monteiro, 2022: Storms drive outgassing of CO2 in the subpolar Southern Ocean. *Nature Communications*, **13 (1)**, 158.

Nikurashin, M., G. K. Vallis, and A. Adcroft, 2013: Routes to energy dissipation for geostrophic flows in the Southern Ocean. *Nature Geoscience*, **6 (1)**, 48–51, doi:10.1038/ngeo1657.

Oerder, V., F. Colas, V. Echevin, S. Masson, F. Lemarié, and L. Renault, 2024: Impacts of the mesoscale ocean-atmosphere coupling on the Peru-Chile ocean dynamics: Impact of the thermal feedback. *Journal of Geophysical Research: Oceans*, **129 (6)**, e2023JC020 351.

Okumura, Y., S.-P. Xie, A. Numaguti, and Y. Tanimoto, 2001: Tropical Atlantic air-sea interaction and its influence on the NAO. *Geophysical Research Letters*, **28 (8)**, 1507–1510.

O'Neill, L. W., D. B. Chelton, and S. K. Esbensen, 2010: The effects of SST-induced surface wind speed and direction gradients on midlatitude surface vorticity and divergence. *Journal of Climate*, **23 (2)**, 255–281.

O'Neill, L. W., D. B. Chelton, and S. K. Esbensen, 2012: Covariability of surface wind and stress responses to sea surface temperature fronts. *Journal of Climate*, **25 (17)**, 5916–5942.

Pedlosky, J., 1987: *Geophysical fluid dynamics*. Springer, 710 pp.

Priyanka, K., R. K. K. Sarangi, D. Jeyapragash, and A. Saravanakumar, 2025: Ekman pumping dynamics and atmospheric aerosol concentration enhancing nitrogen and carbon uptake in the Arabian Sea during winter. *Ocean Dynamics*, **75 (4)**, 1–13.

Rai, S., J. T. Farrar, and H. Aluie, 2025: Atmospheric wind energization of ocean weather. *Nature Communications*, **16 (1)**, 1172.

Rai, S., M. Hecht, M. Maltrud, and H. Aluie, 2021: Scale of oceanic eddy killing by wind from global satellite observations. *Science Advances*, **7 (28)**, eabf4920.

Renault, L., M. Contreras, P. Marchesiello, C. Conejero, I. Uchoa, and J. Wenegrat, 2024: Unraveling the impacts of submesoscale thermal and current feedbacks on the low-level winds and oceanic submesoscale currents. *Journal of Physical Oceanography*, **54 (12)**, 2463–2486.

Renault, L., A. Hall, and J. C. McWilliams, 2016a: Orographic shaping of us west coast wind profiles during the upwelling season. *Climate Dynamics*, **46**, 273–289.

Renault, L., S. Masson, V. Oerder, F. Colas, and J. C. McWilliams, 2023: Modulation of the oceanic mesoscale activity by the mesoscale thermal feedback to the atmosphere. *Journal of Physical Oceanography*.

Renault, L., S. Masson, V. Oerder, S. Jullien, and F. Colas, 2019: Disentangling the mesoscale ocean-atmosphere interactions. *Journal of Geophysical Research: Oceans*, **124 (3)**, 2164–2178.

Renault, L., J. C. McWilliams, and J. Gula, 2018: Dampening of submesoscale currents by air-sea stress coupling in the Californian upwelling system. *Scientific reports*, **8 (1)**, 1–8.

Renault, L., J. C. McWilliams, and S. Masson, 2017: Satellite observations of imprint of oceanic current on wind stress by air-sea coupling. *Scientific Reports*, **7 (1)**, 1–7.

Renault, L., M. J. Molemaker, J. C. McWilliams, A. F. Shchepetkin, F. Lemarié, D. Chelton, S. Illig, and A. Hall, 2016b: Modulation of wind work by oceanic current interaction with the atmosphere. *Journal of Physical Oceanography*, **46 (6)**, 1685–1704.

Resplandy, L., M. Lévy, and D. J. McGillicuddy Jr, 2019: Effects of eddy-driven subduction on ocean biological carbon pump. *Global Biogeochemical Cycles*, **33 (8)**, 1071–1084.

Rhines, P. B., 1977: The dynamics of unsteady currents. *The Sea*, Ideas and Observations on Progressin the Study of the Seas, Vol. 6, J. Wiley & Sons, 189–318.

Rhines, P. B., and W. R. Young, 1982: Homogenization of potential vorticity in planetary gyres. *Journal of Fluid Mechanics*, **122**, 347–367, doi:10.1017/S0022112082002250.

Rocha, C. B., S. T. Gille, T. K. Chereskin, and D. Menemenlis, 2016: Seasonality of submesoscale dynamics in the Kuroshio Extension. *Geophysical Research Letters*, **43 (21)**, 11–304.

Rocha, C. B., G. L. Wagner, and W. R. Young, 2018: Stimulated generation: Extraction of energy from balanced flow by near-inertial waves. *Journal of Fluid Mechanics*, **847**, 417–451, doi:10.1017/jfm.2018.308.

Roemmich, D., and J. Gilson, 2001: Eddy transport of heat and thermocline waters in the North Pacific: A key to interannual/decadal climate variability? *Journal of Physical Oceanography*, **31 (3)**, 675–687.

Rooth, C., and L. Xie, 1992: Air-sea boundary layer dynamics in the presence of mesoscale surface currents. *Journal of Geophysical Research: Oceans*, **97 (C9)**, 14 431–14 438.

Rosso, I., A. M. Hogg, R. Matear, and P. G. Strutton, 2016: Quantifying the influence of sub-mesoscale dynamics on the supply of iron to Southern Ocean phytoplankton blooms. *Deep Sea Research Part I: Oceanographic Research Papers*, **115**, 199–209.

Rudnick, D. L., 2001: On the skewness of vorticity in the upper ocean. *Geophysical Research Letters*, **28 (10)**, 2045–2048.

Salmon, R., 1978: Two-layer quasi-geostrophic turbulence in a simple special case. *Geophysical & Astrophysical Fluid Dynamics*, **10 (1)**, 25–52.

Sasaki, H., P. Klein, B. Qiu, and Y. Sasai, 2014: Impact of oceanic-scale interactions on the seasonal modulation of ocean dynamics by the atmosphere. *Nature Communications*, **5 (1)**, 5636.

Schubert, R., J. Gula, R. J. Greatbatch, B. Baschek, and A. Biastoch, 2020: The submesoscale kinetic energy cascade: Mesoscale absorption of submesoscale mixed layer eddies and frontal downscale fluxes. *Journal of Physical Oceanography*, **50 (9)**, 2573–2589, doi:10.1175/JPO-D-19-0311.1.

Scott, R. B., and F. Wang, 2005: Direct evidence of an oceanic inverse kinetic energy cascade from satellite altimetry. *Journal of Physical Oceanography*, **35 (9)**, 1650–1666.

Seo, H., A. J. Miller, and J. R. Norris, 2016: Eddy–wind interaction in the California current system: Dynamics and impacts. *Journal of Physical Oceanography*, **46 (2)**, 439–459.

Seo, H., L. W. O'Neill, M. A. Bourassa, A. Czaja, K. Drushka, J. B. Edson, B. Fox-Kemper, I. Frenger, S. T. Gille, B. P. Kirtman, and W. Qing, 2023: Ocean mesoscale and frontal-scale ocean–atmosphere interactions and influence on large-scale climate: A review. *Journal of Climate*, **36 (7)**, 1981–2013.

Shakespeare, C. J., A. H. Gibson, A. M. Hogg, S. D. Bachman, S. R. Keating, and N. Velzeboer, 2021: A new open source implementation of Lagrangian filtering: A method to identify internal waves in high-resolution simulations. *Journal of Advances in Modeling Earth Systems*, **13 (10)**, e2021MS002 616.

Shcherbina, A. Y., E. A. D'Asaro, C. M. Lee, J. M. Klymak, M. J. Molemaker, and J. C. McWilliams, 2013: Statistics of vertical vorticity, divergence, and strain in a developed submesoscale turbulence field. *Geophysical Research Letters*, **40 (17)**, 4706–4711.

Siegelman, L., P. Klein, P. Rivière, A. F. Thompson, H. S. Torres, M. M. Flexas, and D. Menemenlis, 2020: Enhanced upward heat transport at deep submesoscale ocean fronts. *Nature Geoscience*, **13 (1)**, 50–55.

Sinha, A., J. Callies, and D. Menemenlis, 2023: Do submesoscales affect the large-scale structure of the upper ocean? *Journal of Physical Oceanography*, **53 (4)**, 1025–1040.

Small, R. J., F. O. Bryan, S. P. Bishop, and R. A. Tomas, 2019: Air–sea turbulent heat fluxes in climate models and observational analyses: What drives their variability? *Journal of Climate*, **32 (8)**, 2397–2421.

Small, R. J., S. P. deSzoeke, S. Xie, L. O'Neill, H. Seo, Q. Song, P. Cornillon, M. Spall, and S. Minobe, 2008: Air–sea interaction over ocean fronts and eddies. *Dynamics of Atmospheres and Oceans*, **45 (3-4)**, 274–319.

Srinivasan, K., R. Barkan, and J. C. McWilliams, 2023: A forward energy flux at submesoscales driven by frontogenesis. *Journal of Physical Oceanography*, **53 (1)**, 287–305, doi:10.1175/JPO-D-22-0001.1.

Stern, M. E., 1965: Interaction of a uniform wind stress with a geostrophic vortex. *Deep Sea Research and Oceanographic Abstracts*, **12 (3)**, 355–367.

Stommel, H., 1948: The westward intensification of wind-driven ocean currents. *Eos, Transactions American Geophysical Union*, **29 (2)**, 202–206, doi:10.1029/TR029i002p00202.

Stone, P. H., 1966: Frontogenesis by horizontal wind deformation fields. *Journal of Atmospheric Sciences*, **23 (5)**, 455–465.

Strobach, E., P. Klein, A. Molod, A. A. Fahad, A. Trayanov, D. Menemenlis, and H. Torres, 2022: Local air-sea interactions at ocean mesoscale and submesoscale in a Western Boundary Current. *Geophysical Research Letters*, **49 (7)**, e2021GL097 003.

Su, Z., J. Wang, P. Klein, A. F. Thompson, and D. Menemenlis, 2018: Ocean submesoscales as a key component of the global heat budget. *Nature Communications*, **9 (1)**, 775.

Sverdrup, H. U., 1947: Wind-driven currents in a baroclinic ocean; with application to the equatorial currents of the eastern pacific. *Proceedings of the National Academy of Sciences*, **33 (11)**, 318–326.

Swart, S., M. D. du Plessis, S. A. Nicholson, P. M. S. Monteiro, L. A. Dove, S. Thomalla, A. F. Thompson, L. C. Biddle, J. M. Edholm, I. Giddy, K. J. Heywood, C. Lee, A. Mahadevan, G. Shilling, and R. B. de Souza, 2023: The Southern Ocean mixed layer and its boundary fluxes: fine-scale observational progress and future research priorities. *Phil. Trans. R. Soc. A.*, **381**.

Takatama, K., and N. Schneider, 2017: The role of back pressure in the atmospheric response to surface stress induced by the Kuroshio. *Journal of the Atmospheric Sciences*, **74 (2)**, 597–615.

Talley, L. D., 2013: Closure of the global overturning circulation through the Indian, Pacific, and Southern Oceans: Schematics and transports. *Oceanography*, **26 (1)**, 80–97.

Taylor, J. R., S. Bachman, M. Stamper, P. Hosegood, K. Adams, J.-B. Sallee, and R. Torres, 2018: Submesoscale Rossby waves on the Antarctic Circumpolar Current. *Science Advances*, **4 (3)**, eaao2824.

Taylor, J. R., and A. F. Thompson, 2023: Submesoscale dynamics in the upper ocean. *Annual Review of Fluid Mechanics*, **55**.

Thomas, L. N., A. Tandon, and A. Mahadevan, 2008: Submesoscale processes and dynamics. *Ocean Modeling in an Eddying Regime, Geophysical Monograph Series*, **177**, 17–38.

Thomas, L. N., J. R. Taylor, R. Ferrari, and T. M. Joyce, 2013: Symmetric instability in the Gulf Stream. *Deep Sea Research Part II: Topical Studies in Oceanography*, **91**, 96–110, doi:10.1016/j.dsr2.2013.02.025.

Torres, H. S., P. Klein, D. Menemenlis, B. Qiu, Z. Su, J. Wang, S. Chen, and L.-L. Fu, 2018: Partitioning ocean motions into balanced motions and internal gravity waves: A modeling study in anticipation of future space missions. *Journal of Geophysical Research: Oceans*, **123 (11)**, 8084–8105.

Torres, H. S., P. Klein, E. D'Asaro, J. Wang, A. F. Thompson, L. Siegelman, D. Menemenlis, E. Rodriguez, A. Wineteer, and D. Perkovic-Martin, 2022a: Separating energetic internal gravity waves and small-scale frontal dynamics. *Geophysical Research Letters*, **49 (6)**, e2021GL096 249.

Torres, H. S., P. Klein, J. Wang, A. Wineteer, B. Qiu, A. F. Thompson, L. Renault, E. Rodriguez, D. Menemenlis, A. Molod, and D. Perkovic-Martin, 2022b: Wind work at the air-sea interface: A modeling study in anticipation of future space missions. *Geoscientific Model Development*, **15 (21)**, 8041–8058.

Torres, H. S., E. Rodriguez, A. Wineteer, P. Klein, A. F. Thompson, J. Callies, E. D'Asaro, D. Perkovic-Martin, J. T. Farrar, F. Polverari, and R. Akbar, 2024: Airborne observations of fast-evolving ocean submesoscale turbulence. *Communications Earth & Environment*, **5 (1)**, 1–10, doi:10.1038/s43247-024-01917-3.

Tulloch, R., J. Marshall, C. Hill, and K. S. Smith, 2011: Scales, growth rates, and spectral fluxes of baroclinic instability in the ocean. *Journal of Physical Oceanography*, **41 (6)**, 1057–1076.

Vallis, G. K., 2017: *Atmospheric and oceanic fluid dynamics*. Cambridge University Press.

Verhoef, A., M. Portabella, and A. Stoffelen, 2012: High-resolution ascat scatterometer winds near the coast. *IEEE Transactions on Geoscience and Remote Sensing*, **50 (7)**, 2481–2487.

Villas Bôas, A. B., B. D. Cornuelle, M. R. Mazloff, S. T. Gille, and F. Ardhuin, 2020: Wave–current interactions at meso-and submesoscales: Insights from idealized numerical simulations. *Journal of Physical Oceanography*, **50 (12)**, 3483–3500.

Villas Bôas, A. B., S. T. Gille, M. R. Mazloff, and B. D. Cornuelle, 2017: Characterization of the deep water surface wave variability in the California current region. *Journal of Geophysical Research: Oceans*, **122 (11)**, 8753–8769.

Wagner, G. L., N. Pizzo, L. Lenain, and F. Veron, 2023: Transition to turbulence in wind-drift layers. *Journal of Fluid Mechanics*, **976**, A8.

Wai, M. M.-K., and S. A. Stage, 1989: Dynamical analyses of marine atmospheric boundary layer structure near the Gulf Stream oceanic front. *Quarterly Journal of the Royal Meteorological Society*, **115 (485)**, 29–44.

Wallace, J. M., T. Mitchell, and C. Deser, 1989: The influence of sea-surface temperature on surface wind in the eastern equatorial Pacific: Seasonal and interannual variability. *Journal of Climate*, **2 (12)**, 1492–1499.

Wenegrat, J. O., and L. N. Thomas, 2017: Ekman transport in balanced currents with curvature. *Journal of Physical Oceanography*, **47 (5)**, 1189–1203.

Whalen, C. B., and K. Drushka, 2025: Global distribution and governing dynamics of submesoscale density fronts. *Journal of Physical Oceanography*.

Wineteer, A., D. Perkovic-Martin, R. Monje, E. Rodríguez, T. Gál, N. Niamsuwan, F. Nicaise, K. Srinivasan, C. Baldi, N. Majurec, and Coauthors, 2020: Measuring winds and currents with Ka-band Doppler scatterometry: An airborne implementation and progress towards a spaceborne mission. *Remote Sensing*, **12 (6)**, 1021.

Wunsch, C., and R. Ferrari, 2004: Vertical mixing, energy, and the general circulation of the oceans. *Annual Review of Fluid Mechanics*, **36 (1)**, 281–314.

Wunsch, C., and D. Stammer, 1998: Satellite altimetry, the marine geoid, and the oceanic general circulation. *Annual Review of Earth and Planetary Sciences*, **26 (1)**, 219–253.

Xie, J.-H., and J. Vanneste, 2015: A generalised-Lagrangian-mean model of the interactions between near-inertial waves and mean flow. *Journal of Fluid Mechanics*, **774**, 143–169, doi:10.1017/jfm.2015.251.

Xie, S.-P., 2004: Satellite observations of cool ocean–atmosphere interaction. *Bulletin of the American Meteorological Society*, **85 (2)**, 195–208.

Xu, Y., and R. B. Scott, 2008: Subtleties in forcing eddy resolving ocean models with satellite wind data. *Ocean Modelling*, **20 (3)**, 240–251.

Young, W., 1994: The subinertial mixed layer approximation. *Journal of Physical Oceanography*, **24 (8)**, 1812–1826.

Young, W., and L. Chen, 1995: Baroclinic instability and thermohaline gradient alignment in the mixed layer. *Journal of Physical Oceanography*, **25 (12)**, 3172–3185.

Yu, X., A. C. Naveira Garabato, A. P. Martin, C. E. Buckingham, L. Brannigan, and Z. Su, 2019: An annual cycle of submesoscale vertical flow and restratification in the upper ocean. *Journal of Physical Oceanography*, **49 (6)**, 1439–1461.

Zhai, X., H. L. Johnson, and D. P. Marshall, 2010: Significant sink of ocean-eddy energy near western boundaries. *Nature Geoscience*, **3 (9)**, 608–612, doi:10.1038/ngeo943.